# Drapability Characterisation of Dry Non-Crimp Fabrics for Preforming Simulation Applications

Jung (Andrew) BAE

Department of Mechanical Engineering

McGill University, Montreal

August 2022

*A thesis submitted to McGill University in partial fulfillment of the requirements of the degree of Master of Science*

# Abstract

The automotive and aerospace industries are constantly looking to improve their manufacturing techniques and to decrease the manufacturing cost. They are looking into liquid composite moulding (LCM) with dry non-crimp fabric (NCF) as an economical alternative to traditional autoclave manufacturing process. Non-crimp fabric material is known to have a great drapeability properties which increases its potential in terms of design flexibility. Proper characterisation methodologies are required to create accurate preforming simulations to predict the preforming defects at both ply and laminate levels. Simulation tools can also determine final fibre orientation which is critical for local mechanical strength and local permeability. The objectives of the present work where to characterise NCF drapability behaviour, implement them in PAM-FORM preforming simulation software and validate NCF drapability for a complex geometry.

The NCF materials used in this project were TG15N, SG33N, and TG33N, supplied by Texonic[Inc]. The fabrics were characterised in shear and bending to accommodate the most dominant deformation mode and wrinkle formation respectively. Picture-frame method (ASTM D8057) and bending cantilever test by Peirce (modified from ASTM D1388) were used to characterise shear and bending properties of the fabrics respectively. Methodologies were developed to ensure test reproducibility. The characterised reinforcement properties were implemented as material data card in the PAM-FORM software from ESI Group. The material data cards were validated by modelling the picture-frame test and the bending cantilever characterisation tests in PAM-FORM. Good correlation was achieved between the simulation and measured experimental data.

Using the validated NCF material data cards for shear and bending behaviours  drapability property values for tensile and friction behaviours from the literature, preforming simulations were used to predict the forming of NCF for different geometries and various preforming processes. A membrane preforming model was used to validate the preforming of a complex geometry. The experimental and numerical shear angles were compared by using a gridline methodology and the bridging distances were compared using a 3D scanning methodology. PAM-FORM was able to accurately predict preform shear angles and bridging but did not capture the wrinkles formation for the complex geometry. Also, a sensitivity analysis of NCF tensile properties

on preforming behaviour was performed. No significant variation was observed with the tested NCF moduli. Flat pattern optimisation was performed on the matched-tool forming simulation and was compared with flat pattern result of another preforming software tool (FiberSim). Flat pattern optimisation increases the part quality and PAM-FORM's flat pattern resulted in better preform. Overall, PAM-FORM was able to predict the outcome of experimental membrane preforming of NCF with shear and bending characterisation test.

# Sommaire

L'industrie automobile et aérospatiale est constamment à la recherche de procédés de fabrication améliorés afin de réduire les coûts de fabrication. Le moulage par transfert de résine avec des renforts non tissés est une option économique pour la fabrication de pièces composites de haute performance comparée aux procédés par autoclave. Les renforts non tissés sont connus pour avoir de très bonnes propriétés de drapage permettant plus de flexibilité de conception en termes de géométrie. De bonnes méthodes de caractérisation sont nécessaires afin d'obtenir des résultats de simulation de préformage précis. Les outils de simulations peuvent aussi prédire les orientations finales des fibres qui ont un effet important sur la résistance locale d'une pièce en composite et sur la perméabilité locale de la préforme. L'objectif du travail présenté dans cette thèse est de caractériser les renforts non tissés, de les implémenter dans la simulation de préformage du logiciel PAM-FORM du groupe ESI, et de développer les méthodes de validation des propriétés de formage pour des géométries complexes.

Les trois types de renforts non tissés utilisés dans ce travail sont le TG15N, SG33N, et TG33N fabriqués par Texonic[Inc]. Les tissus ont été caractérisés en cisaillement et en flexion car ces deux propriétés ont le plus d'influence sur les modes de déformation les plus dominants. Les tests de cisaillement dans un cadre (ASTM D8057) et de flexion en porte-à-faux de Peirce (ASTM D1388 modifié) ont été utilisés pour caractériser les comportements en cisaillement et en flexion respectivement. Les méthodologies ont été développées afin d'assurer la reproductibilité des expérimentations. Les propriétés des tissus caractérisés ont été implémentées dans le logiciel de simulation de préformage PAM-FORM. Les propriétés des matériaux ont été validées en reproduisant les tests de caractérisations dans PAM-FORM. De bonnes corrélations ont été obtenues entre les résultats de la simulation et les résultats expérimentaux.

En utilisant les propriétés de préformage des renforts caractérisées en cisaillement et en flexion ainsi que les propriétés en tension et en friction qui sont prises de la littérature, les simulations de préformage ont été réalisées pour tester différentes géométries et procédés de préformage afin d'améliorer l'efficacité du procédé. Le préformage avec une membrane sous vide a été utilisé afin de valider la simulation pour une géométrie complexe. Les angles de cisaillement de la préforme fabriquée expérimentalement ont été comparés avec les angles de cisaillement

obtenus par la simulation. Aussi, la conformation géométrique de la préforme avec le moule a été mesurée avec un scanner 3D et comparée aux résultats de simulation. Le logiciel de simulation PAM-FORM a prédit précisément les angles de cisaillement et de la conformité pour la géométrie complexe, mais n'a pas été capable de prédire les plis du tissu. De plus, une analyse de sensibilité sur l'influence du module de tension du renfort a été effectuée afin de déterminer l'effet de cette propriété sur le préformage. Cette analyse a montré que le module de tension n'avait pas d'effet significatif sur la simulation de préformage. Enfin, l'optimisation du gabarit plat de la préforme a été effectuée en simulant un préformage par moule métallique. Les résultats du préformage en utilisant le gabarit plat optimisé du logiciel PAM-FORM et d'un autre programme de simulation (FiberSim) ont été comparés. L'optimisation du gabarit plat avec PAM-FORM a montré une amélioration de qualité de la préforme ainsi qu'un meilleur résultat que le gabarit plat prédit par FiberSim. En conclusion, PAM-FORM était capable de prédire précisément le préformage expérimental en utilisant les renforts non tissés qui sont seulement caractérisés en cisaillement et en flexion.

# Acknowledgements

Last but not least, love and appreciation go to my parents, sister, and grand parents for their constant generous support, patience, and selfless sacrifice thought out this experience and to my friends who took interest in my work and provided help and advice when needed. Their supports have given me the confidence to achieve this milestone.

# Table of Contents

# List of Tables

# List of Figures

XIII

XVII

# List of Abbreviations

| | |
|---|---|
| 3D | Three dimensional |
| CAD | Computer-aid design |
| CFRP | Carbon fibre reinforced polymer |
| CRTM | Compression resin transfer moulding |
| CTA | Centre Technologique en Aérospatiale |
| DIC | Digital image correlation |
| FEM | Finite element modelling |
| GUI | Graphical user interphase |
| OL | Overhang length |
| LCM | Liquid composite moulding |
| NCF | Non-crimp fabric |
| NRC | National Research Council of Canada |
| Prepregs | Pre-impregnated materials |
| $R^2$ | Coefficient of determination |
| RTM | Resin transfer moulding |
| SNAP | Short Novel Affordable Process |
| UTM | Universal tensile test machine |
| VARTM | Vacuum assisted resin transfer moulding |
| 3D | Three dimensional |

xx

# 1  Introduction

## 1.1  Background

This research project has been conducted within SNAP Composite Research and Development industrial group in conjunction with Nation Research Council of Canada, Automotive and Surface Transportation Research Center located in Boucherville, Quebec. SNAP is an acronym for Short Novel Affordable Process which targets composite material manufacturing for the transportation industry. The SNAP Composite project's objective is to develop low-cost manufacturing methods of high-performance composites for medium to high-volume market segments. Its relative cost and annual volume market compared to other composite manufacturing techniques are demonstrated in Figure 1. SNAP Composite focuses on two process families: Compression Resin Transfer Moulding (CRTM) process, i.e. SNAP-RTM, and compression of prepreg, i.e. SNAP-PREG. The detailed manufacturing steps of these two processes are illustrated in Figure 2 and described below:

- SNAP-RTM: Preformed dry fabrics are transferred to CRTM mould. Resin is injected within a gap between the mould and fabrics. While the resin gets compressed and gets impregnated into the fabrics, the curing process is initiated. The total process time can vary from 2 to 15 minutes depending on resin system.

- SNAP-PREG: Preformed prepreg are transferred to the mould where the impregnated resin gets cured. The total process time is 2 to 15 minutes depending on resin system.
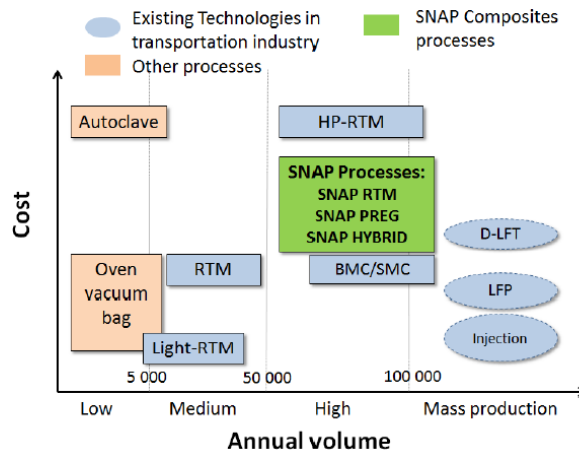
Figure 1 Positioning of SNAP processes compared to other composites manufacturing processes (reproduced with permission from L. Khoun [1])
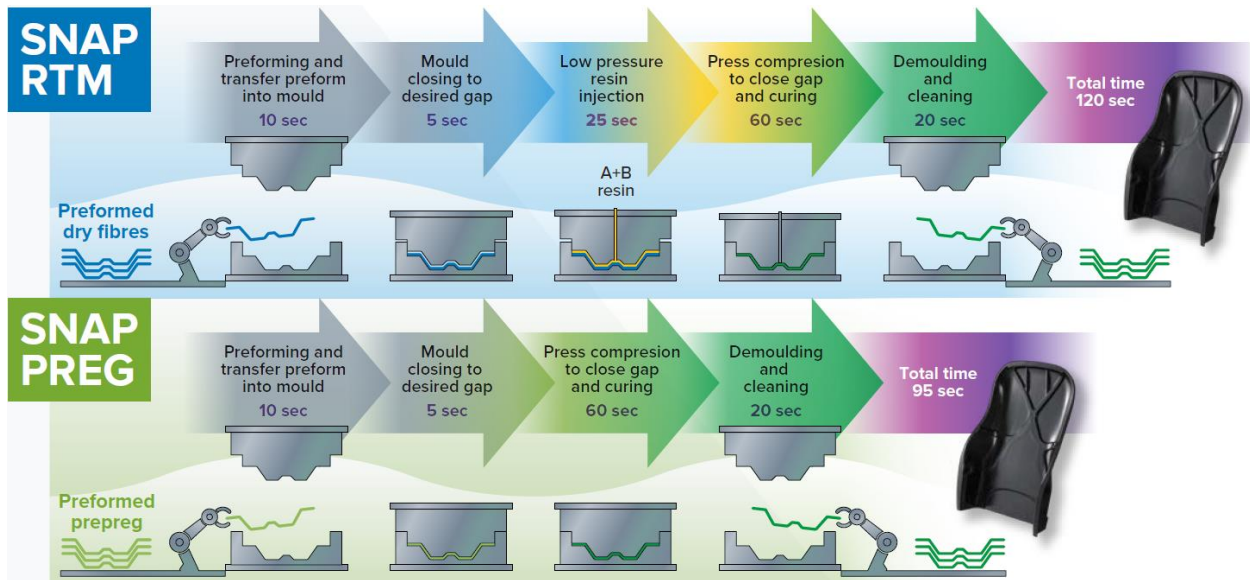


Figure 2 SNAP-RTM and SNAP-PREG processes (reproduced with permission from L. Khoun [1])

## 1.2 Preforming Processes

Preforming of reinforcements is often the first manufacturing step prior to composite moulding process, especially for Liquid Composite Moulding (LCM) processes. A schematic of the preforming process is illustrated in Figure 3. The preforming process consists in stacking up the dry fibres and applying pressure using solid punch tool or flexible membrane to form the stack of reinforcement to a near-final shape. The preformed shape can be stabilised by applying binders

2

between the preform layers. Preforming is a necessary step to help handling and control fibre alignment, thickness, and final fibre volume fraction ($V_f$) [2].
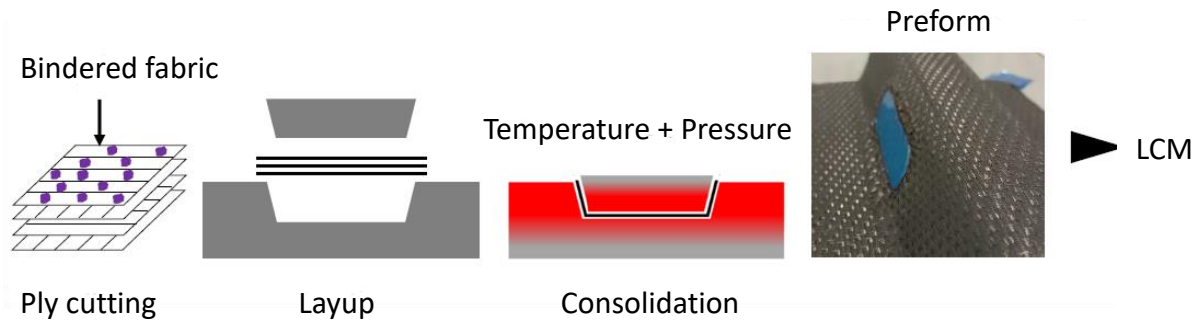


Figure 3 Preforming process using dry fabric and binder material (reproduced with permission from L. Grou [3])

There are several types of preforming methodologies: diaphragm forming, vacuum forming, pressure forming, matched-tool forming. Few examples of various types of membrane forming processes are illustrated in Figure 4.

Each preforming technique has its own advantages and disadvantages. For example, the membrane preforming has lower capital investment compared to rigid tool forming [4]. However, as the forming forces should overcome frictional forces between fabric and tool as well as between fabrics, the forming force of membrane preforming technique may not be high enough to fully deform the fabrics. Thus, the membrane preforming is more prone to local defects such as bridging compared to matched-tool preforming [4].



(a)         (b)         (c)
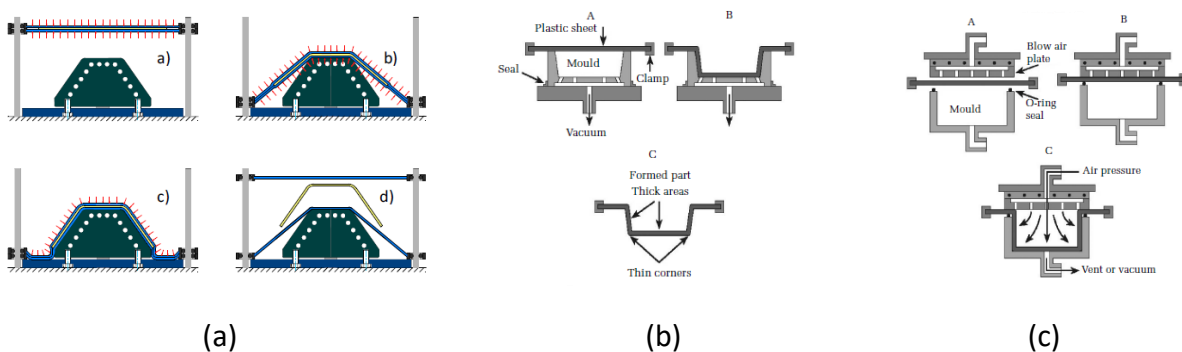
Figure 4 Schematic of membrane forming: double diaphragm forming (a) (reproduced with permission from Elsevier [4]), vacuum forming (b) and pressure forming (c) (reproduced with permission from Sage Journal [5])

Preforming techniques and reinforcement materials can affect the preform and the composite part quality and performance by changing the preform permeability, the fibre orientation, or the fibre volume fraction. It is therefore important to be able to predict the fabric's behaviour during preforming to predict the preforming outcome. The approach of using various simulations during composite manufacturing is well depicted in Figure 5. Iterations of preforming simulations are performed to test different preforming conditions, materials, or different designs of the components to reduce defects. Then, the simulation results can be transferred to perform permeability model to improve LCM techniques. Also, the results from preforming simulation can be used to determine the component's mechanical performance using structural model.
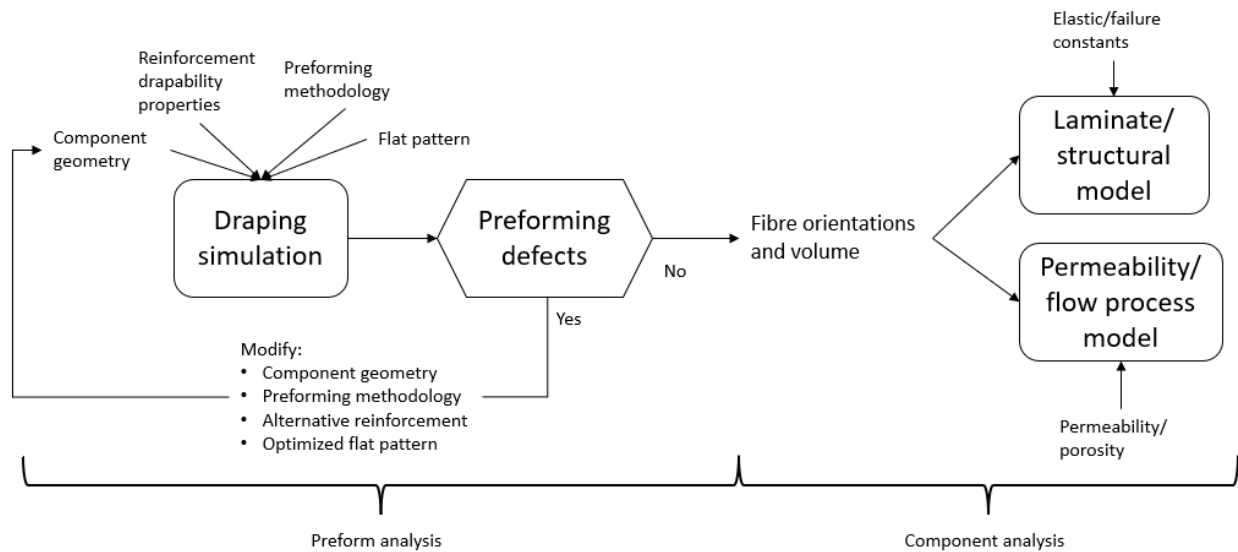


Figure 5 Flow chart for use of different simulation techniques for composite manufacturing design [6]

Preforming simulation must be performed to determine the optimal preforming methodology. Accurate material properties are required to run accurate preforming simulation. Several materials such as dry fabrics and prepregs can be simulated in preforming simulations. In the literature, drapability characterisation tests for dry fabrics are well defined for woven fabrics but not well for NCF architectures [7] despite several advantages (i.e. economic and mechanical properties) over woven fabrics.

## 1.3 Thesis Objectives

In this context, the main research objective of this thesis is to characterise the drapability properties of dry NCF for the purpose of conducting preforming simulation. To achieve this goal, the following tasks were carried out:

1) Characterise NCF shear and bending behaviours, the picture-frame method (ASTM D8067) and the bending cantilever test by Peirce (modified from ASTM D1388) were used respectively.

2) Implement material data card in preforming simulation software.

3) Validate the implementation methodology by reproducing the test setup in preforming simulation software.

4) Validate the drapability properties of NCF for a complex geometry using preforming simulation.

## 1.4 Outline of Thesis

The thesis is organised into the following chapters:

**Chapter 2:** A literature review of the preforming simulation processes is conducted in this chapter. First, LCM processes and different types of dry fabrics are presented to understand the advantages of NCF for preforming. Several types of preforming defects are discussed with their causes and consequences to the preform and final laminate part. Also, the different types of preforming simulations are introduced in this chapter. Lastly, the different reinforcement drapability properties required to perform those preforming simulations, are explained. Effect of reinforcement property to the preform as well as the methodologies to characterise them are discussed. This chapter is used to guide characterisation and validation process presented in the following chapters.

**Chapter 3:** This chapter presents the methodologies and results of drapability properties characterisation. The objective is to measure the densities as well as shear and bending behaviours. The properties implementation validation methodologies are also discussed in this chapter.

**Chapter 4:** This chapter presents results of preforming simulations using the implemented material data cards from Chapter 3 using complex geometry. The results of the comparison

5

between simulation and experimental preforming are discussed using two validation methodologies: a gridline methodology and a 3D scanning methodology. Also, sensitivity analyses on tensile properties of NCF are performed. This chapter also presents the flat pattern optimisation results.

**Chapter 5:** This chapter presents the summary of the discussions of the previous chapters.

# 2 Literature Review

This chapter presents a literature review of the preforming simulation processes. Liquid composite moulding processes and different types of dry fabrics are introduced to understand the advantages of NCF in preforming. The cause and consequences of several types of defects are discussed. Then, different types and usages of preforming simulations are introduced. Finally, the effect of different drapability behaviours and their characterisation methodologies are presented.

## 2.1 Dry Fabric and Liquid Composite Moulding

A material can be defined as composite material only if its constituents have significantly different physical properties [8]. These composite materials in general are known to have higher strength-to-weight ratio, to be more fatigue resistant, corrosion resistant, and more capable to shape in large critical components by reducing the number of parts and joints required compared to traditional metal manufacturing counterpart [9]. An example of comparison between aluminium and carbon fibre reinforced plastic (CFRP) constructions of Lamborghini Gallardo Spyder's boot lid is demonstrated in Figure 6. In some cases, pre-impregnated (prepregs) materials are favored for their manufacturing quality over dry fabrics. However, prepreg material has several economical disadvantages such as higher manufacturing, labour, and storage costs [8]. Prepregs are often thinner than dry fabric which leads to have lower deposition rate. Also, prepreg material requires freezer to be stored and has limited shelf lifetime compared to dry fabrics which can be stored in room temperature with unlimited shelf lifetime.

CFRP
(2 parts - air exhaust integrated)

Weight (in terms of figures): 20 kg

Weight (weighted): 15.1 kg

(a)                                    (b)                                    (c)
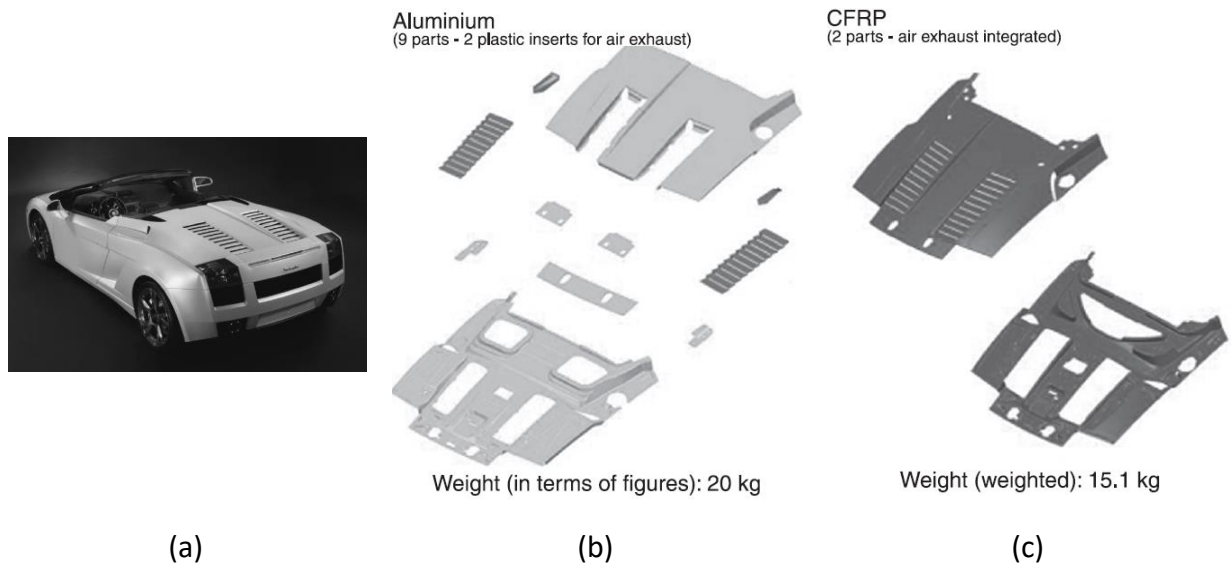
Figure 6 Lamborghini Gallardo Spyder's back view (a), schematic of aluminium construction (b) and schematic of composite material construction (c) (reproduced with permission from Elsevier [10])

LCM technique was developed in aerospace industries to reduce composite manufacturing cost. The traditional aerospace composite manufacturing was using autoclave and prepreg materials. For LCM, resin is injected from its reservoir into the mould cavity by infiltrating the reinforcements [11]. Thus, manufacturing with dry fabrics with LCM (Figure 7) is seen as an economical option. Several various techniques of LCM are illustrated in Figure 8. Resin transfer moulding (RTM) is a process where a liquid resin is injected and cured under closed mould. Vacuum assisted resin transfer moulding (VARTM) is a process where liquid resin is injected and cured using vacuum pressure under vacuum bagging. RTM Light is a process where liquid resin is injected and cured under vacuum mould. Compression RTM is a process which the resin is injected into small gap between the mould and preform. Then, using the compressive force of the mould, the resin gets fully infiltrated and cured.
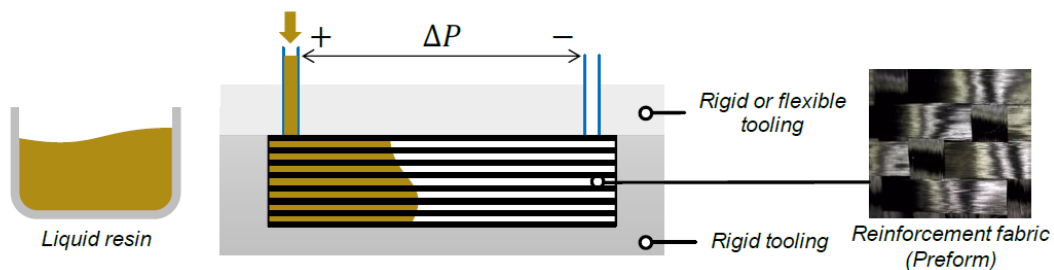


Figure 7 Schematic of basic principle of LCM process (reproduced with permission from L. Grou [3])
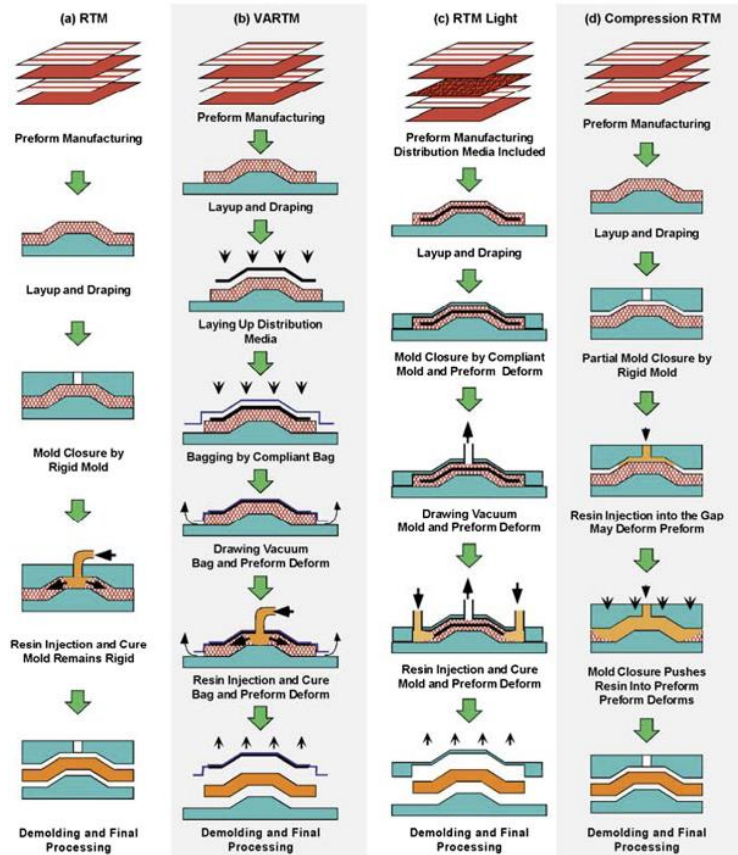
Figure 8 Illustrations of various LCM techniques: Resin transfer moulding (RTM) (a), Vacuum assisted resin transfer moulding (VARTM) (b), RTM Light (c), and Compression RTM (d) (Copyright © 2002 CRC Press. All rights reserved [11])

Within dry fabrics, there are two main different types of textile architectures: woven and NCF as shown in Figure 9. There are several types of weave patterns such as plain, twill, and harness satin. The woven construction increases the fabric stability during handling but decreases its mechanical properties [8, 12]. As it has a complicated structure, it makes the mechanical properties harder to predict [13].

<div align="center">(a)          (b)</div>
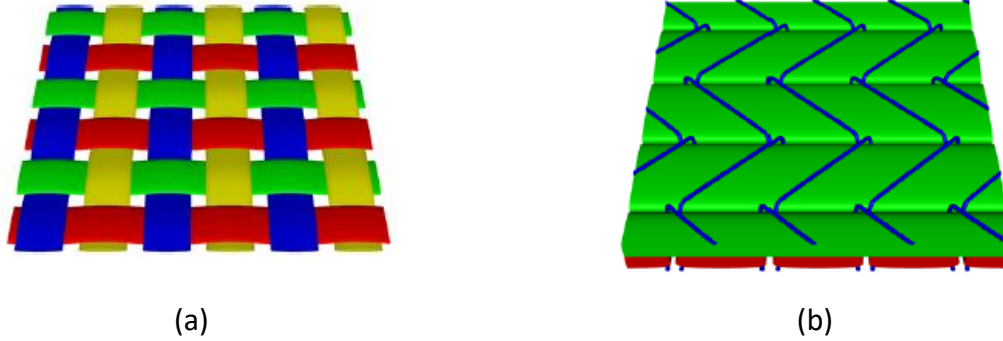
Figure 9 Examples of textile architectures of plain weave fabric (a) and NCF (b) (reproduced with permission from A. Long [14])

Non crimp fabrics are composed with layers of fabric tows laid on top of each other, held by polyester stitches. These stitches don't contribute to the mechanical properties but allow the fibre tows to stay together [12]. Due to the simpler yarn construction, the manufacturing cost of NCF is more economical compared to woven fabrics. Non crimp fabrics are also known to have great drapability properties which increase their potential use in terms of design and geometry flexibility [15]. NCF has higher mechanical properties than woven fabrics as it is constructed without internally structured weaves. However, NCF are more difficult to manipulate due to their structural instability. They are prone to fraying at the edge and shear more freely as they are only held by stitches [8]. Those disadvantages make accurate material characterisation more difficult and increase variability of the fabric drapability behaviours [16].

In both automotive and aerospace industries, the usage of the NCF material is increasing. Despite popularity of the short fibre reinforced sheet moulding components and bulk moulding components, NCF are now found in some high-end cars (Figure 6 and Figure 10) [10]. In the aerospace industries, most composite parts are still manufactured with prepregs materials with few exceptions manufactured with LCM. Amongst these few exceptions, most are manufactured with NCF materials due to their high strength properties [17]. For example, the rear pressure bulkhead of Airbus A380 (Figure 11) was manufactured with NCF with automated draping system [17]. The NCF has the potential to be mass produced, however, the quality of the manufactured composite part must be met [10]. To do so, repeatable preforming process must be achieved.
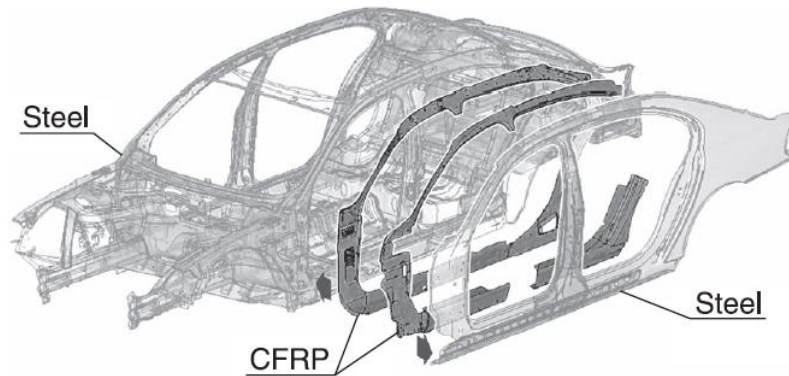
Figure 10 Use of NCF in automotive industry: side frame of BMW Hydrogen 7 (reproduced with permission from Elsevier [10])



Figure 11 Use of NCF in aerospace industry: Draping of NCF in the Airbus A380 rear pressure bulkhead production (reproduced with permission from P. Middendorf [17])

## 2.2 Preforming Defects

Preforming defects are often caused by a combination of several different factors such as material properties and boundary conditions. The main preforming defects are bridging and out-of-plane wrinkles (Figure 12).

Bridging (Figure 12-a) is caused if the forming force is not sufficient to deform fabrics into concave corners or into grooves [18]. Overcoming the fabric bending stiffness and the inter-ply friction as well as the friction between the tool and the ply become important to reduce bridging.

There are two types of wrinkles: out-of-plane (Figure 12-b) and in-plane (Figure 12-c) wrinkles. These types of wrinkles are caused by fibre compression [19]. However, only out-of-plane

wrinkles will be dealt for the rest of the thesis as it is one of the most critical defects in preforming. In the rest of the thesis, out-of-plane wrinkles will be shortened as wrinkles. Wrinkles were previously known to be caused when the fabric shear angle exceeds the locking angle of the fabric [20, 21]. However, recent studies have shown that the wrinkles are more likely caused by the bending stiffness of the fabric [22, 23]. Presence of wrinkles dramatically decreases the compressive strength of the composite [24]. Addition of blank holder can be beneficial to reduce wrinkles [22]. Additional potential sources of defects and control techniques during preforming process are listed in Table 1.
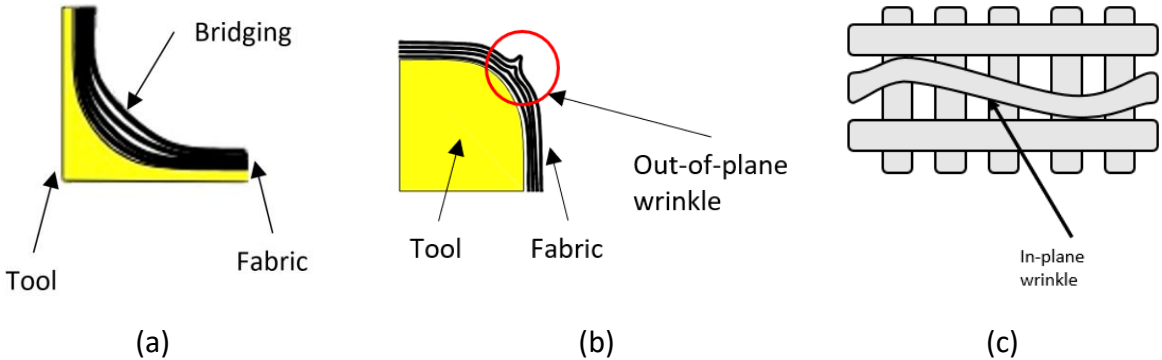


Figure 12 Preforming defects: bridging (a) (reproduced with permission from K. Potter [25]), out-of-plane wrinkling effect (b) (reproduced with permission from K. Potter [25]) and in-plane wrinkling effect (c)

Table 1 Sources of potential variability at each process step during experimental preforming setup (reproduced with permission from Elsevier [16])

| | Process Step | Variability Source(s) | Potential Effect(s) | *Effect* on Variability (1-3) | Control Technique(s) | *Control* Effectiveness (1-3) | Net Result (*Effect – Control*) |
|---|---|---|---|---|---|---|---|
| **Process** *Uncontrolled Sources of Variability* | **Material Production** | • Tolerances in fibre production<br>• Tolerances in fabric assembly | • Irregular fibre tow orientations<br>• Variations in sample mass | 3 | • Not controlled – investigated in study | N/A | 3 |
| | **Material Forming** | • Deformation modes<br>• Dynamic effects<br>• Frictional behaviour | • Changes in preformed shape<br>• Changes in wrinkle behaviour | 3 | • Not controlled – investigated in study | N/A | 3 |
| **Process** *Controlled Sources of Variability* | **Sample Cutting** | • Sample dimensions | • Variations in sample dimensions and/or geometry<br>• Variation in sample mass | 1 | • Use cutting template to get consistent geometry<br>• Apply weights onto template to prevent sliding | 3 | -2 |
| | | • Lateral alignment of template | • Variations in fibre tow locations on the sample | 1 | • Using stitching as guide when aligning cutting template<br>• Apply dead weights onto template to prevent sliding | 3 | -2 |
| | **Placement of Sample** | • Alignment of sample relative to blank holder | • Variations in initial fibre tow orientations | 1 | • Use the fixed grooves on blank holder to align stitch direction<br>• Use ruler and protractor to ensure correct rotation | 3 | -2 |
| | **Loading of Sample** | • Inconsistent weight loading | • Irregular blank holder force application | 1 | • Avoid local loading variations between the 4 weight hooks on the weight ring. | 2 | -1 |
| | | • Inconsistent weight ring alignment | • Irregular blank holder force application | 1 | • Place weight ring on blank holder such that the opposing hooks are directly in line with the fixed grooves | 1 | 0 |

Preforming defects directly affect the performance of the composite. It is therefore important to understand how they are formed to prevent them. In this optic, performing simulations are essential tool to predict the reinforcement behaviour during the preforming step and make preform adjustments accordingly.

## 2.3    Preforming Simulation

In the past decades, preforming simulation tools have been developed to predict the preforming capabilities of dry fabrics as well as thermoset and thermoplastic prepreg materials. Preforming simulations are used to predict the outcome of the preforming step and to reduce the development time (trial and error experiments) [13]. Preforming simulations are used to predict preforming defects such as wrinkling, bridging, thickness variation, or shear at both ply and laminate levels.

Simulation tools can also determine the final fibre orientation and the shear angle which are critical for local mechanical strength and local permeability [24, 26]. In the literature, studies have shown that the fibre orientation and local volume fraction of the preforms determine the

mechanical properties of the final composite part and local permeability of the preform [27-30]. Studies have shown that geometric complexity which causes changes in fibre angles affects the fibre volume fraction and the porosity which affect the local permeability [27-29].

The mechanical strength of a composite part depends on the fibre direction. The difference in the angle between fibre direction and load direction determines the local mechanical strength along the load direction [24, 30]. Also preforming defects such as wrinkles decrease the compressive strength [24]. In consequence, simulation of preforming setup is important to determine the defects, and undesired fibre orientation prior to experimenting on the preforming setup. An example of fibre orientation obtained during preforming simulation is shown in Figure 13.
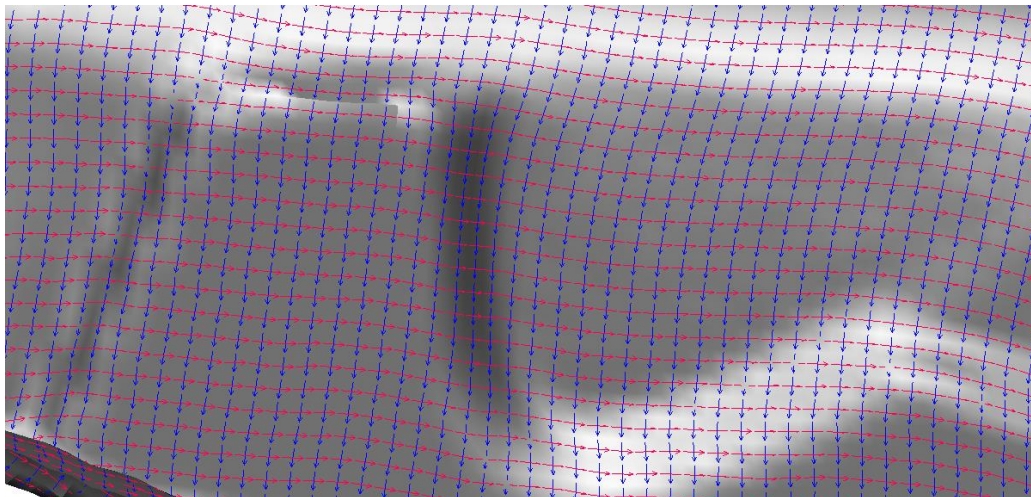


Figure 13 Modified fibre directions due to presence of curvature in PAM-FORM software

Preforming simulations can also determine preform flat pattern for the desired geometry and help optimising it. Flat pattern is the expanded pattern from draped fabric. Optimising the shape of the fabric before preforming, as in during the first trimming phase, can affect its final part quality and reduce manufacturing steps. Krebs et al. [31] showed that flat pattern optimisation is important when it comes to reduce waste, avoid redundant areas which can lead to defects (wrinkling, buckling and bridging). The concept of flat pattern optimisation is illustrated in Figure 14.
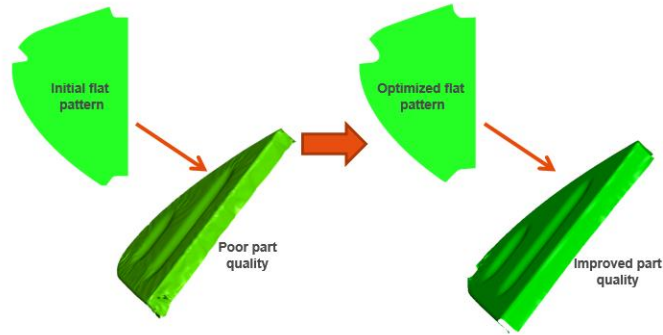
Figure 14 Objective of performing flat pattern optimisation (Copyright © ESI Group. All rights reserved

There are three different categories of preforming simulation: kinematic mapping, mesoscopic
finite element modelling (FEM) and macroscopic FEM. The kinematic mapping ignores material
behaviour and process parameters and only considers desired component geometric shape [6].
As material behaviour and process parameters are not considered, the kinematic mapping has
fast computational time but limited accuracy [33]. According to Vanclooster et al. [33] kinematic
models oversimplify the material model and fails in predicting accurate fibre orientation.
Commercially available software Fibersim from NX (Figure 15) is an example of software using
kinematic mapping simulation.



(a) (b)
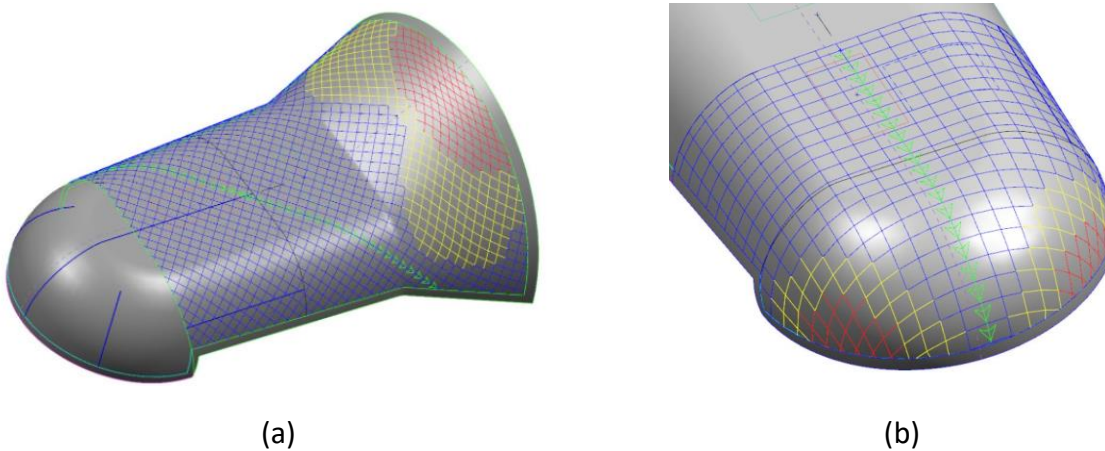
Figure 15 Examples of kinematic mapping simulation result using FiberSim. The coloured grid represents
the different shear angles of the reinforcements after forming (Copyright © 2019 Siemens. All rights
reserved [34])

Mesoscopic FEM has been developed in academia to calculate each load acting on a unit woven cell (Figure 16) to predict the final shape of the preforms [13]. Each fibre tow is modelled using computer-aid design (CAD) and meshed [14]. Examples of loads applied on a unit cell which are considered in mesoscopic FEM are illustrated in Figure 16. An example of calculation methods is shown in Figure 17-a. In this example, the bending moment is calculated taking consideration of tows crossover angle. The complexity of the calculation of mesoscopic FEM can be illustrated by three examples of tows crossovers illustrated in Figure 17-b. For each fibre tows crossover angle, the calculation must be adapted accordingly. The mesoscopic FEM is very computationally expensive and a unit cell cannot represent the behaviour of the fabric on its entire geometry [35]. To the author's knowledge, there is no commercially available mesoscopic FEM preforming software due to the very high computational power required to run simulation for small and simple geometry. For mesoscopic FEM, reinforcement material properties such as shear, bending, tensile, twisting, and friction must be characterised [36].
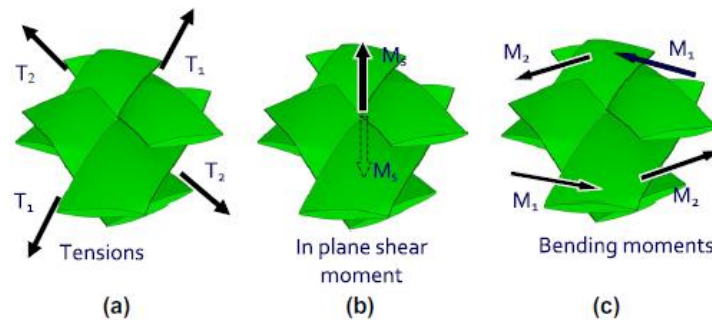


Figure 16 Load resultant on a unit woven cell (reproduced with permission from Elsevier [13])

Type 1)   Type 2)   Type 3)

(a)   (b)
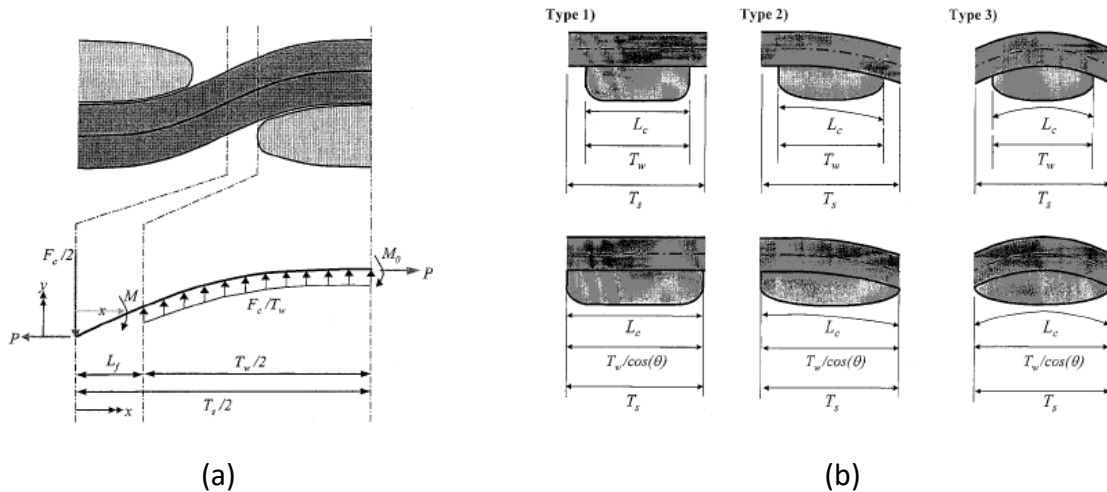
Figure 17 Microscopic FEM calculation methods (a) and three different types of tow crossover – before shearing (top) and during shearing (bottom) (b) and (reproduced with permission from A. Long [37])

The macroscopic FEM takes into consideration the material property but as a homogeneous material, making it possible to create simulation of a larger part [6]. Macroscopic FEM simulation with refined mesh gives a reasonably good prediction of the local shear angle prediction with less than 10° of difference compared to experimental preforming [33]. However, it relies highly on the material experimental characterisation data [38]. Thus, good characterisation methodology is crucial for a macroscopic simulation to give accurate results [39]. Fibre tow defects such as in-plane bending, or twisting cannot be simulated using this process.

The commercial tool PAM-FORM from ESI Group uses macroscopic FEM to run preforming simulation. This software has a wide range of applications including rigid mould stamping, rubber pad forming, thermoforming and flexible membrane forming [40]. The simulation predicts the final fibre orientation, the thickness distribution, the optimum flat pattern and the preforming defects at both ply and laminate levels [40]. The software can perform simulations for both fabrics and unidirectional materials as well as for both dry and prepreg materials. Non-linear elasto-plastic material properties can be modelled by adding temperature, strain, strain-rate, pressure, viscosity dependencies [40]. The material data card in PAM-FORM requires the fabric shear, bending, and tensile behaviours in the warp and weft directions. Figure 18 shows an example of preforming simulation performed in PAM-FORM. The preforming software is capable to predict defects such as wrinkles and fibre orientations.

17

Figure 18 Example of preforming simulation using PAM-FORM (Copyright © ESI Group. All rights reserved [32])

The macroscopic FEM was widely used for woven fabrics, but not many studies were performed on NCF despite its mechanical and economic advantages [7]. The drapability behaviour in shear, bending and tensile loading is required to conduct macroscopic preforming simulations for NCF. Additionally, the friction behaviour between fabric layers and between the tool material and fabrics need to be characterised.

## 2.4 Drapability Characterisation Methodologies

Due to interactions of the yarns during deformation, predicting formability behaviour of dry fabrics is complex [13]. In fact, several factors such as shear, bending, tensile and as well as friction (inter-layer and between ply and tool) interact during forming. There are very large number of components at the scale of the yarn or of the fibre and large number of frictions between them which makes prediction of behaviour much difficult [13]. These complex behaviours and interactions must be shown as homogeneous material for macroscopic FEM. Thus, accurate material characterisation is necessary to obtain accurate simulation results [39].

### 2.4.1 In-Plane Shear

The shear behaviour is the most important deformation mode in dry fabric preforming as it determines the final fibre direction [41]. There is no simple relationship between shear angle and wrinkling [22]. Two examples of experimental preform of the hemisphere are shown in Figure 19. Modified shear angles and fibre directions can be observed. Figure 19-b explains how the shear angle can be experimentally determined by observing the rotation of the tows.

18

The lines indicate the rotation of the tows as the fabric deforms. This rotation is an indication of the amount of shear.

Shear angle =45°
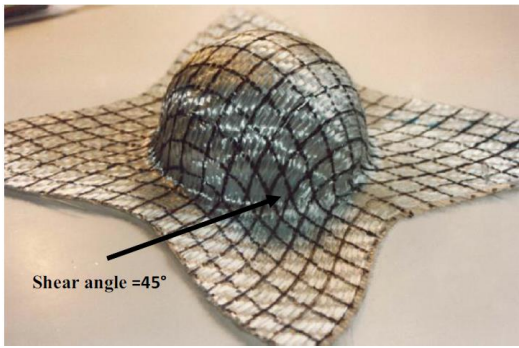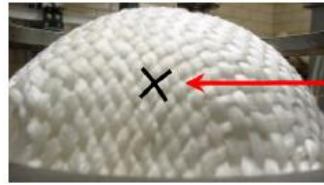
(a)                                                             (b)

Figure 19 Modified fibre angles due to presence of curvature (a) (reproduced with permission from Springer Nature [42]) and indication of fabric shearing (b) (reproduced with permission from Elsevier [41])

Performing in-plane shear characterisation test to obtain locking angle is an important step. The locking angle is an angle specific for each fabric material at which in-plane shear stiffness increases drastically. This occurs because tows are no longer able to freely rotate and compressive forces are exerted on each other [41]. Wrinkles occur at shear angle larger than locking angle [20, 21]. However locking angle is not sufficient to solely predict the shape of wrinkles [22]. Locking angle of the fabric can be determined at the intersection of the two tangents of the stress-strain curve inflection resulting from a fabric in-plane shear test [15, 43].

Several studies have shown that some NCF can have asymmetric shear behaviours depending on their architecture and stitch pattern [16, 19, 44]. Figure 20 shows asymmetric shear behaviour caused by the tension and compression of the stitches. Thus, for all NCF architecture, shear characterisation tests must be performed in both positive and negative shear directions.
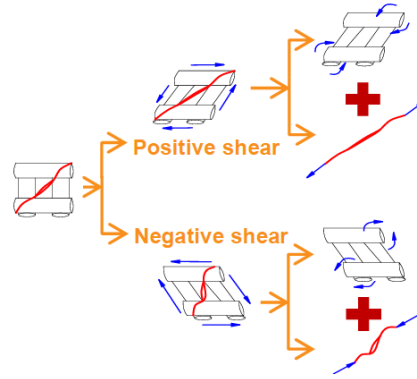
Figure 20 Schematic showing the asymmetric shear behaviour of NCF (reproduced with permission from S. Chen [44])

From the literature both picture-frame and bias-extension tests are the common shear characterisation methodologies [7, 45].

Picture-frame (also known as trellis-frame) test is performed on a standard universal tensile test machine (UTM). Fabric sample is clamped at the edges of in a four-corner pinned jig (Figure 21) in order to prevent slippage [45]. The samples are loaded in tension with a constant crosshead displacement rate.
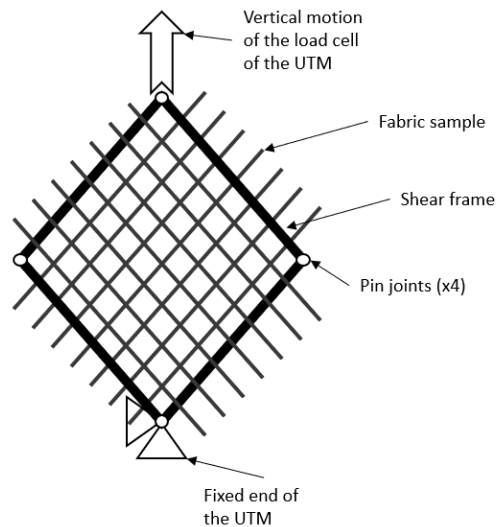


Figure 21 Schematic of the picture frame setup

Zero test or calibration is required in this setup [41]. Shear behaviour as well as locking angle can be measured as shown in Figure 22. The picture-frame test must be performed with care as it is more sensitive to fibre alignment [45]. If the fibres are not exactly aligned with the 45°, then

20

tension forces can be recorded which makes the test load larger than the actual shear load [46]. Compared to bias-extension test, picture-frame test is more prone to wrinkles during testing [15].
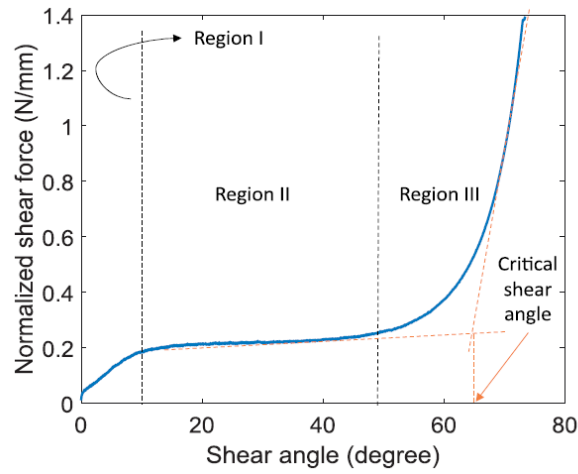


Figure 22 Typical result of picture-frame test with inflection point methodology to calculate locking angle (reproduced with permission from Sage Journal [15])

Bias-extension is another test can also be performed to characterise shear behaviour. The bias-extension setup is shown in Figure 23-a. Yarns are oriented at +/- 45° and pure-shear can be observed in zone C of Figure 23-b and c [20]. For this test method, results depend on displacement rate of the tensile machine as shown in Figure 24. The bias-extension test setup is much simpler than picture-frame setup but is more prone to slippage [45].



(a)                                          (b)                    (c)
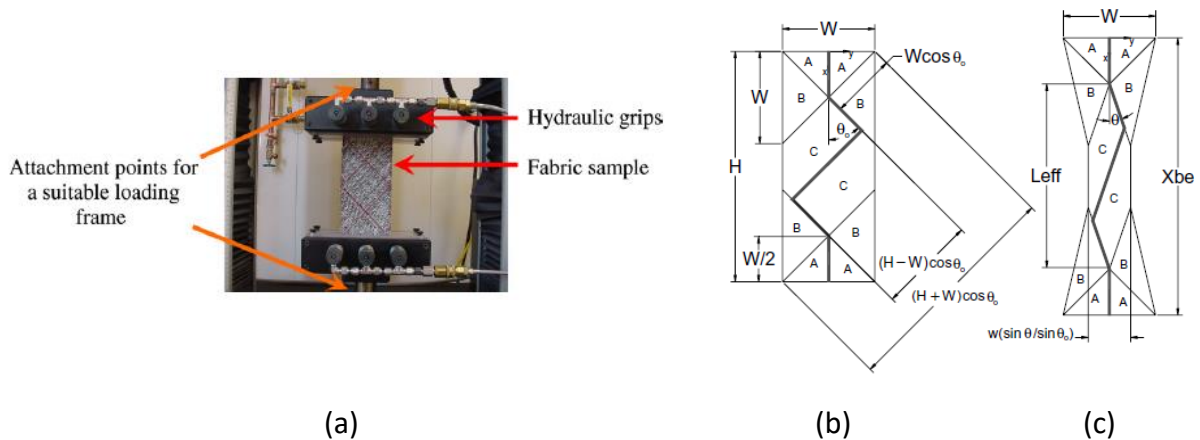
Figure 23 Bias-extension test apparatus (a) and schematic showing the undeformed (b) deformed (c) shapes of the specimen in the bias-extension test (reproduced with permission from Elsevier [41])
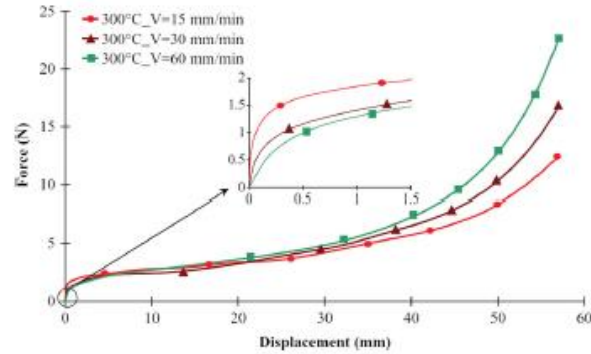
Figure 24 Example of bias-extension test results at different crosshead displacement rates (reproduced with permission from Springer Nature [42])

Bias-extension setup is more prone to sliding than picture-frame test. Also, the fibre tows of NCF are more prone to slide than woven fabrics. To characterise pure shear, picture-frame is a more suitable test than bias-extension for NCF material [47].

## 2.4.2 Out-Plane Bending

The out-of-plane bending behaviour is the second most important factor in the deformation of fabrics. Although wrinkles depend on several factors such as shear strain levels, stiffness, and boundary conditions, bending stiffness is the most important factor for wrinkles [13, 22, 23]. It has been shown that higher flexural rigidity increases wrinkle size [22] but lower flexural rigidity material is more prone to wrinkles [22, 23]. Haanappel et al. [48] performed sensitivity analysis on bending properties and showed that it can also affect the resulting shear angle of the preform. However, this phenomenon is only significant at the edge of the mould.

The methodology to measure the out-of-plane bending stiffness is the cantilever bending test (Figure 25) following ASTM D1388 [49] or Peirce Cantilever test [50]. This test consists of increasing the overhang length gradually until the tested sample strip reaches 41.5°. One of the drawbacks of ASTM D1388 is that it is limited to a single bending angle. Bilbao et al. [51] used this cantilever test with various overhang lengths to determine the bending modulus as a function of the radius of curvature and characterise non-linear and non-elastic bending behaviour. An example of their test results is depicted in Figure 26.
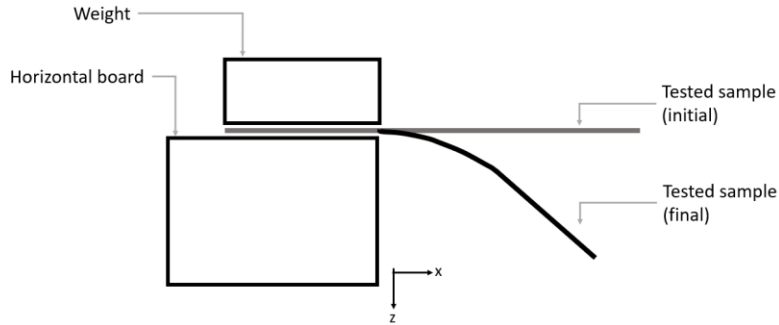
Figure 25 Schematic of the bending cantilever test
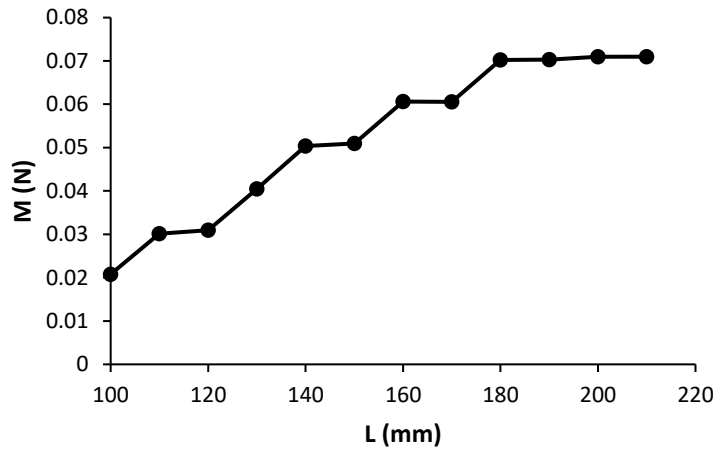


Figure 26 Results from cantilever test analysing moment for several bending length (reproduced with permission from E. de Bilbao [51])

It should be noted that the equations to calculate the flexural rigidity (G) from the ASTM D1388 and Peirce are different:

$$G_{ASTM} = 1.421 \cdot 10^{-11} \cdot \rho_A \cdot c^3 \tag{2.1}$$

$$G_{Peirce} = 9.81 \cdot 10^{-12} \cdot \rho_A \cdot c^3 \tag{2.2}$$

where $\rho_A$ is the areal weight of the fabric and $c$ is the bending length. Peirce first introduced the concept of the bending length as the length of fabric that will bend under its own weight during the cantilever test [50]. It mathematically relates the overhang length to the fabric's flexural stiffness. The relationship between the bending length and the overhang length was developed

based on elastic theory and corrected with empirical data. No information is available on the ASTM standard D1388 regarding the calculation of the scale factor of 1.421 x 10$^{-11}$.

In their study, Lammens et al. [52] showed that Peirce's equation of flexural rigidity gave much more accurate results than the ASTM standard.

### 2.4.3 Tensile

The tensile behaviour is not as important as the shear or bending behaviour to characterise the fabric deformation properties, but it is critical if there is a blank holder in the preforming setup as it applies tension into the fabrics [22]. Use of blank holder to hold the preform during the preforming step can be beneficial if the preforming setup creates too many wrinkles [22]. During preforming, the fabric deforms first in shear and in bending [51]. If the fabric is constrained to deform in those two deformation modes, then the fabric will start deforming in tension [53].

Tensile properties of a dry woven fabric has a non-linear behaviour due to decrease of crimp at low loading and has a linear behaviour at higher loading [13]. Bi-axial phenomenon can be observed due to warp and weft axial strains [13]. Both tensile and biaxial tensile (Figure 27) tests can be performed but for a balanced fabric, tensile behaviour in both directions is identical [54]. However, due to stitching of fibres, NCF has no non-linearity nor dependencies on biaxial strain ratio unlike woven fabrics [55]. A typical test standard for testing tensile of fabric is ASTM D882 and rubber padding grips may be required to prevent slippage [52].



Figure 27 Biaxial tensile test device (reproduced with permission from Elsevier [54])

### 2.4.4 Friction

Friction can be characterised by pulling the fabric out while applying normal force on the contact surface. Friction characterisation methods between the tool and the fabric and between each ply are depicted in Figure 28. A typical result of this test apparatus is shown in Figure 29. According to Fetfatsidis et al. [53] , the friction coefficient between each ply and between the tool and the fabric is constant and can vary between 0.1-0.5. Presence of more crossover of fibres would increase the friction coefficient [39]. This means that for NCF, the friction coefficient would be relatively low. In several studies, friction coefficients of woven fabrics were assumed to be between 0.2 and 0.3 [13, 22, 56].



(a)                                                           (b)
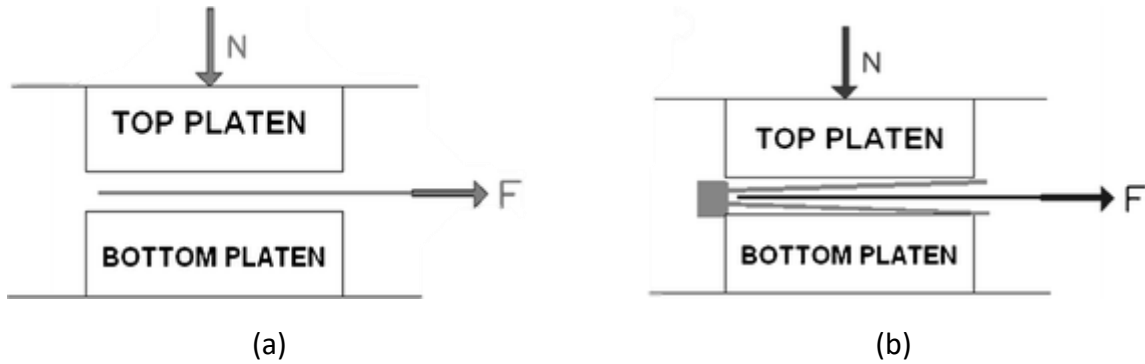
Figure 28 Friction test schematics for tool-ply friction (a) and ply-ply friction (b) (reproduced with permission from Springer Nature [53])
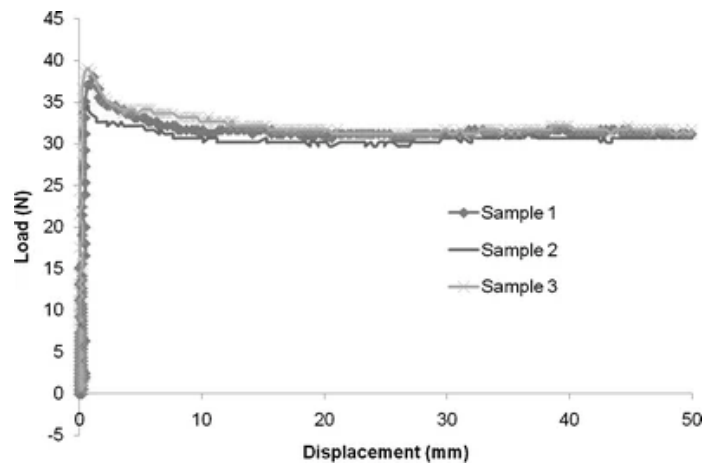


Figure 29 Typical result of friction test (reproduced with permission from Springer Nature [53])

## 2.5   Drapability Properties Validation Methodologies

Once measured, the drapability behaviours of the reinforcements are implemented in preforming simulation software as material data cards. Comparison between preforming experiments and numerical prediction is then necessary to validate the simulation.

Drapability properties validations are generally carried out on specific geometry. The most common ones are the hemisphere geometry (Figure 30-a) and the half cylinder with two half hemispheres geometry (Figure 30-b). These two geometries are considered as simple geometries where only shear properties can be sufficient to obtain good correlations with the simulation. However, some other complex geometries are also used such as tetrahedral (Figure 31-a) and eggshell geometries (Figure 31-b). To obtain good correlations for these complex geometries, often, some other drapability properties must be characterised.



(a)                                                                              (b)
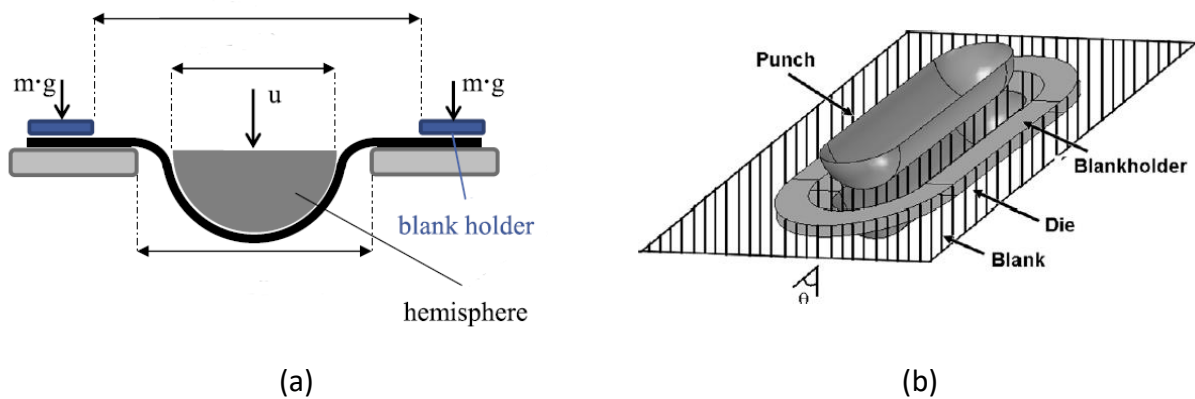
Figure 30 Examples of validation geometries used in literature: hemisphere (a) (reproduced with permission from Elsevier [47]), half cylinder with two half hemispheres (b) (reproduced with permission from S. Lomov [33])

|     |     |
| :-: | :-: |
| (a) | (b) |
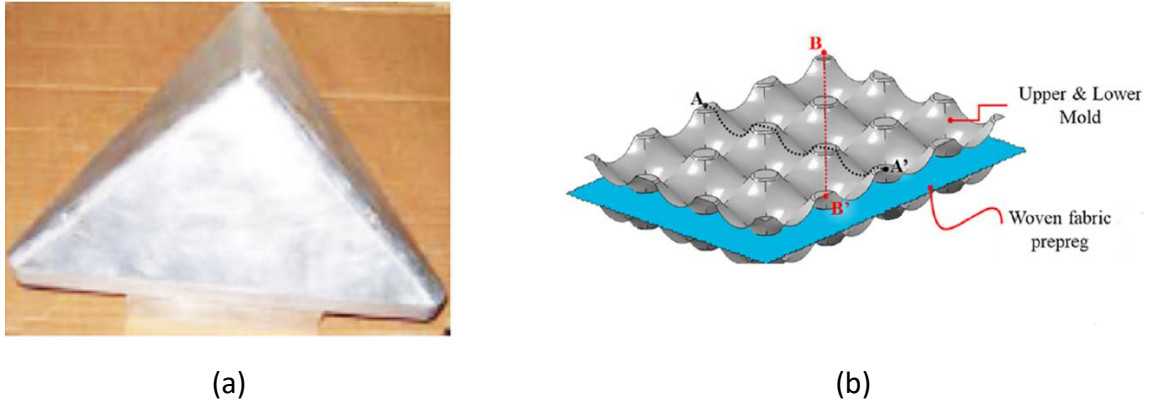
Figure 31 Examples of validation complex geometries used in literature: tetrahedral (a) (reproduced with permission from Elsevier [13]), complex eggshell (b) (reproduced with permission from Elsevier [57])

Digital image correlation (DIC) is used in numerous studies as a tool to compare the final shape and the local shear angles, obtained experimentally and numerically [7, 13]. An overview of the comparison process using DIC is well illustrated in the Figure 32. It requires capturing the image using camera, processing the image, and comparing it with simulation results. Example of comparison of experimental and numerical final fibre orientations from a study by Mallach et al. is shown in Figure 33. Both good and bad correlations are shown for comparison purposes. Digital image correlation comparison methodologies allow to capture the validity of the characterised drapability properties for preforming simulation.
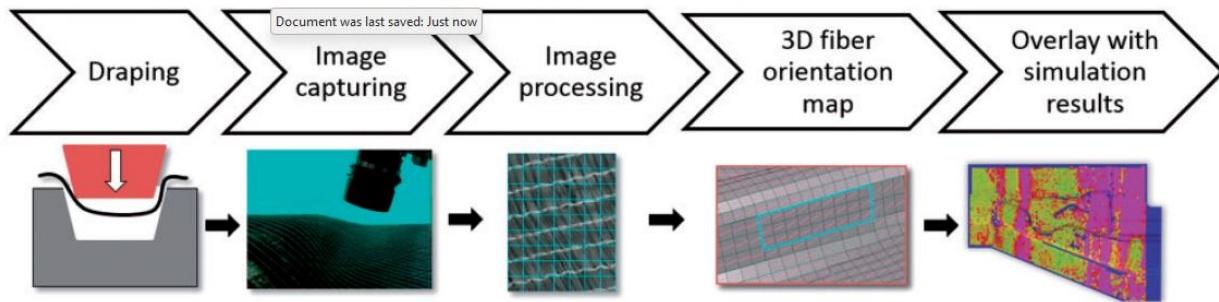


Figure 32 Overview of validation steps using DIC (reproduced with permission from P. Middendorf [7])
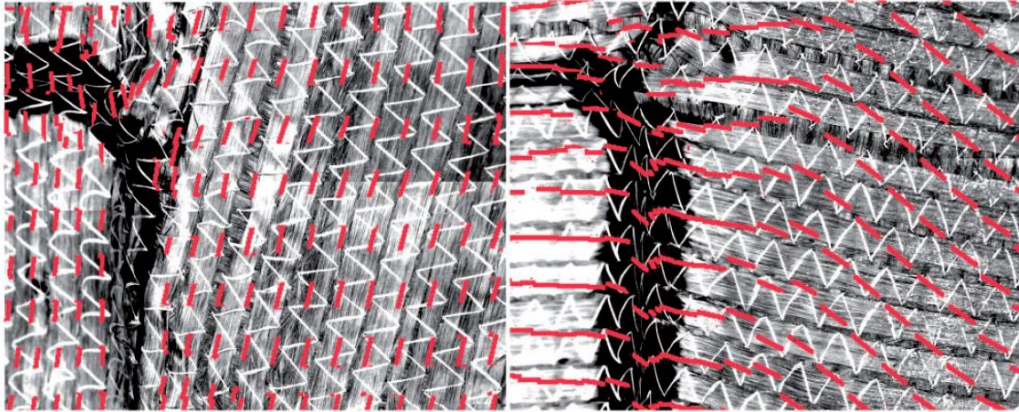
(a)                                                        (b)

Figure 33 Comparison results between simulation (in red dashed line) with experimental fibre orientation: good correlation (a) and bad correlation (b) (reproduced with permission from P. Middendorf [7])

Despite its accuracy, DIC is very time consuming, expensive and may not be available in all facilities. The traditional gridline methodology is still used in the literature to compare the outcome of simulation and experimental fibre orientation and shear angle. The idea is to draw gridlines on the fabrics while being flat. Once the fabrics are preformed, then the deformation can be more visible with the help of the gridlines. The example from Long et al. (Figure 34) [37] shows how the same material with two different preforming setups can result in different fibre orientation. It also shows the comparison results with the simulation.
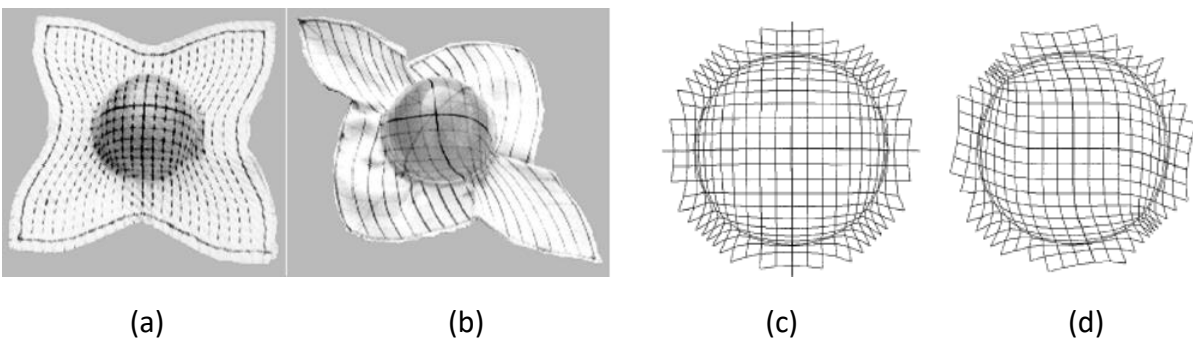


(a)                      (b)                      (c)                      (d)

Figure 34 Comparison of fibre orientation using gridline methodology between experimental (a and b) and simulation outcome (c and d) with two different preforming setups (reproduced with permission from A. Long [37])

28

The bending properties can be validated by modelling the bending cantilever test using preforming simulation [51, 52]. Experimental and simulation bending curvature profiles can be compared to validate the simulation. Figure 35 shows an example of final deformed shape of bending cantilever using finite element modelling.
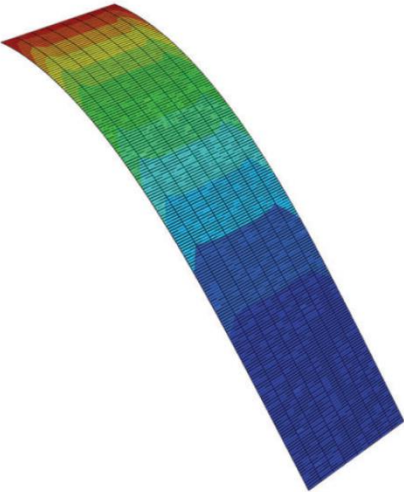


Figure 35 Finite element modelling result of bending cantilever test(reproduced with permission from Sage Journals [52])

Bending modulus can also be validated by comparing the shape and the number of wrinkles to the experimental preforming [22, 23] as shown in Figure 36.



(a)                                                          (b)
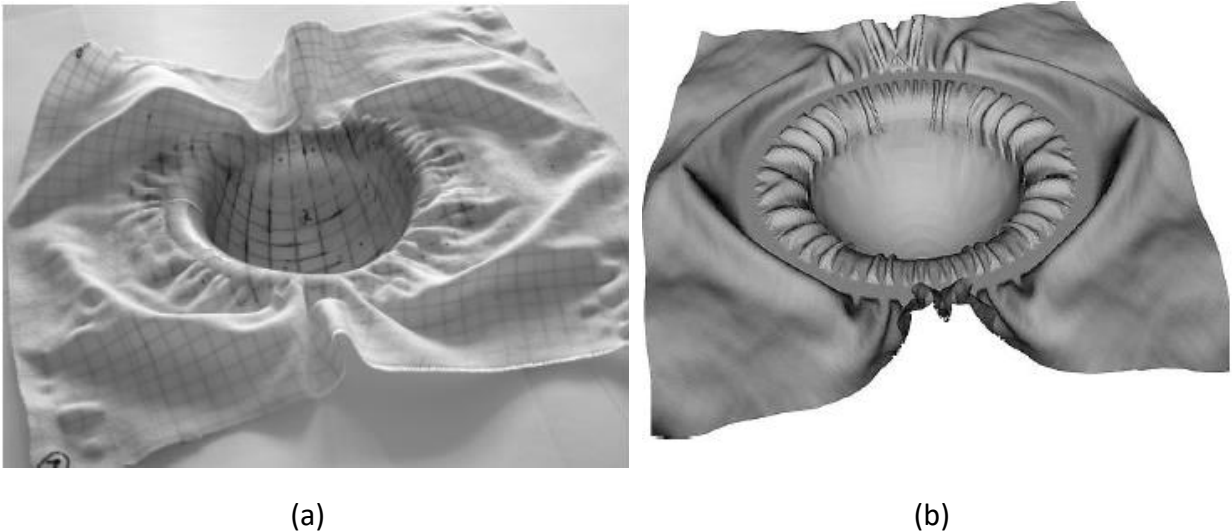
Figure 36 Comparison between experimental (a) and simulation (b) preforming with wrinkled shapes (reproduced with permission from Elsevier [22])

## 2.6   Summary of Literature Review

Non-crimp fabric materials combine the advantages of both UD prepregs (mechanical strength) and dry woven fabrics (low manufacturing cost) [8]. However, the downside of this material is its geometrical instability. Preforming is a necessary step in RTM process which is essential to have better repeatability on fibre alignment, better thickness control and better final fibre volume fraction control [2]. Two main preforming methods are matched-tool and membrane preforming. Matched-tool requires more capital investment compared to membrane preforming. However, membrane preforming is more prone to defects such as bridging and wrinkling [4]. Preforming simulation becomes crucial to determine fibre orientation and defects. Out of the three types of preforming simulation, macroscopic FEM simulation is often used in the industry. It considers material properties unlike kinematics mapping which has limited accuracy [33]. It is much faster than mesoscopic FEM by considering material as homogeneous material.

Commercially available PAM-FORM preforming software was used in this project to predict the outcome of preforming NCF for large components (1~2 metres). The simulation is generally used to predict preforming defects such as bridging, wrinkling as they affect directly the mechanical property of the composite part [24, 30]. The simulation is also used to predict the final fibre orientation as it affects local strength [24, 30] and local permeability [27-29]. Finally, flat pattern optimisation is performed to minimise material waste and avoid redundant areas which can lead to defects [31]. As mentioned, several times in previous sections, due to the nature of the material and simulation, proper characterisation methods are crucial. In this study, in-plane shear behaviour, which determine the final fibre orientation of the fabric, was characterised by using picture-frame method. Out-plane bending properties was characterised by using Peirce cantilever method at several overhang lengths to consider different radii of curvature. Tensile properties were not characterised in this specific project as no blank holder were used for the preforming step. The tensile is not considered to be as dominant as the other two properties of the fabric. Friction properties were not characterised in this specific project as lots of studies have assumed the friction coefficient to be 0.2 [13, 22].

# 3  Material Models

This chapter presents the methodologies and results of drapability behaviour (shear and bending) characterisation. The methodologies for the implementation of the material data card are discussed. The validation of the properties was performed by reproducing the characterisation tests in PAM-FORM preforming simulation software. The results of the validations are reported. These implemented material data cards are later used in the following chapter for complex geometry simulations.

## 3.1  Material Description

Glass fibre NCF materials studied in this paper (TG15N, TG33N, SG33N) were supplied by Texonic [Inc]. Table 2 summarises the main fabric characteristics. The NCF contains one layer of UD glass fibres in the warp direction stacked between two layers of glass fibres in the weft direction. The layers are stitched with a thin polyester yarn in the warp direction as shown in Figure 37. SG33N and TG33N have the same architecture but with a higher areal density compared to TG15N. SG33N also contains thermoplastic stitches in the warp direction, which can be used as in-situ binder for the preforming and could eliminate the powder binder application step. All three fabrics are biaxial warp-knitted NCF which have the highest productivity rate with low manufacturing complexity suitable for high volume production and cost effective manufacturing process [58].

Table 2 Technical data sheet information of NCF fabrics [59-61]

| Material | TG15N | SG33N | TG33N |
|---|---|---|---|
| Infused Thickness (mm) | 0.45 | 0.75 | 0.86 |
| Stitch Composition (Warp direction) | Polyester | Polyester + Thermoplastic binder | Polyester |
| Warp/Weft Weight Ratio | 44%-56% | 46%-54% | 45%-55% |
| Warp Material Composition | 735 tex (GF) 16.7 tex (Polyester) 3.1 /cm | 1100 tex (GF) 16.66 tex (Polyester) 60 tex (UniFlex<sup>TM</sup>) 4.6 /cm | 1100 tex (GF) 16.66 tex (Polyester) 4.6 /cm |
| Weft Material Composition | 275 tex (GF) 10.4 /cm | 735 tex (GF) 8.4 /cm | 735 tex (GF) 8.4/cm |
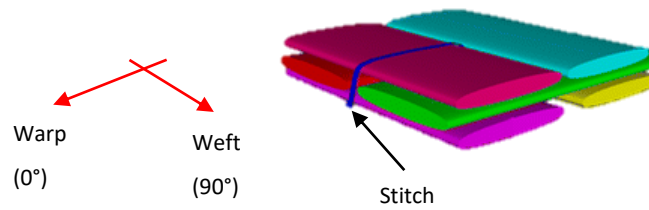
Figure 37 Fibre architecture of TG15N, SG33N, and TG33N (reproduced with permission from R. Younes [58])

According to the literature, fabric in-plane shear and out-of-plane bending properties are the most dominant properties affecting the preform geometry. Thus, those two properties were measured for the three NCF reinforcements. As no blank holder was used for the preforming process, fabric tensile property was not measured. Friction coefficient was assumed based on values from the literatures [13, 22, 56]. Thus, tensile and friction properties were not characterised. Fabric areal density and thickness were also measured experimentally.

## 3.2 Fabric Densities

Material areal weight and volumetric density were measured by cutting samples of fabrics (about $10^{-2}$ m$^2$) and weighted on ©Sartorius CP225D high precision scale. Each sample's measured area and weight are reported in Table 3.

Table 3 Measured fabrics' geometrical parameters for density calculation

| Material | Length (m) | Width (m) | Area (x10$^{-2}$ m$^2$) | Mass (g) |
|----------|-----------|-----------|------------------------|----------|
| TG15N    | 0.95      | 0.87      | 0.827                  | 4.5809   |
|          | 1.20      | 0.85      | 1.020                  | 5.4586   |
|          | 1.45      | 0.85      | 1.233                  | 6.7068   |
| SG33N    | 2.05      | 0.80      | 1.640                  | 17.2835  |
|          | 2.20      | 0.80      | 1.760                  | 18.4855  |
|          | 1.75      | 0.78      | 1.365                  | 14.1767  |
|          | 1.65      | 0.77      | 1.271                  | 13.8205  |
| TG33N    | 1.10      | 1.05      | 1.155                  | 13.2410  |
|          | 1.80      | 1.08      | 1.944                  | 20.7568  |
|          | 1.65      | 1.05      | 1.733                  | 19.8493  |

Thickness of the fabrics was measured with a caliper. As the fabrics were very soft and were easily deformable, it was important not to squeeze too much the fabrics between the caliper to prevent thickness measurement inaccuracy.

The areal weight and volumetric density were calculated using the equations below:

$$\rho_A = \frac{m}{A} \tag{3.1}$$

$$\rho_V = \frac{\rho_A}{T_h} \tag{3.2}$$

where $\rho_A$ and $\rho_V$ are the areal weight and volumetric density respectively, $m$ is the measured mass, $A$ is the measured area of fabric sample, and $T_h$ is the measured thickness of the fabric. The thickness of each fabric material and results for areal and volumetric density calculations are reported in Table 4.

Table 4 Calculated average areal weight and volumetric density of fabrics

| Material | Measured Thickness (x10⁻³ m) | Areal Weight (g/m²) | Volumetric Density (g/m³) |
|---|---|---|---|
| TG15N | 0.45 | 554 | 1.23 |
| | | 535 | 1.20 |
| | | 544 | 1.21 |
| | Average | 545 ± 9.5 | 1.21 ± 0.015 |
| SG33N | 0.95 | 1054 | 1.11 |
| | | 1050 | 1.11 |
| | | 1039 | 1.10 |
| | | 1087 | 1.15 |
| | Average | 1058 ± 7.77 | 1.11 ± 0.006 |
| TG33N | 0.8 | 1146 | 1.43 |
| | | 1168 | 1.33 |
| | | 1145 | 1.43 |
| | Average | 1120 ± 13.0 | 1.40 ± 0.058 |

## 3.3  In-plane Shear

### 3.3.1  Picture-Frame Test Methodology

The picture-frame setup (Figure 38) was used to characterise the shear behaviour of the NCF. Picture-frame tests were performed on an Instron® 5985 testing machine with a 5 kN load cell.
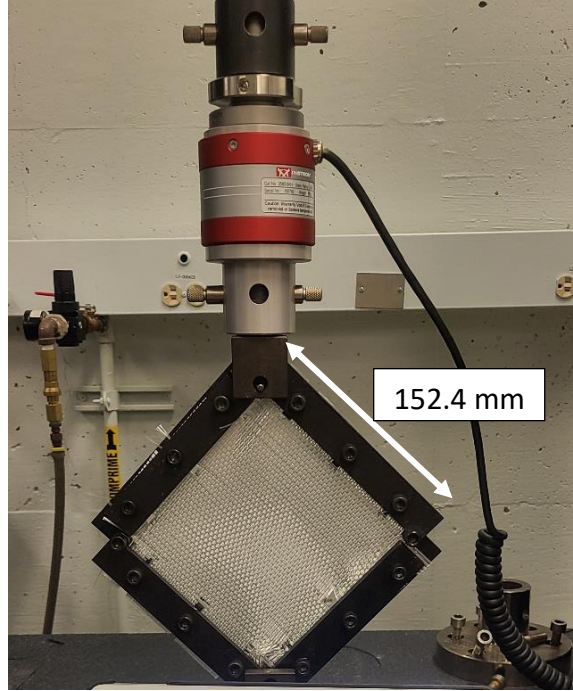
Figure 38 Picture-frame apparatus on Instron tensile test machine with 5kN load cell

Prior to test the samples, zero test or calibration test is first required [41]. From the results of a zero test, as shown in Figure 39, the load required to pull on the fixture was measured and subtracted from the fabric sample test results by using the equation (3.3). The load was then simplified using the equations (3.4) and (3.5). These equations are shown as dashed red line in Figure 39:

$$F_x = F_r - F_{zero} \tag{3.3}$$

$$\begin{cases} F_{zero} = \dfrac{1}{70} \cdot d & |0 \leq d < 70 \tag{3.4} \\ F_{zero} = \dfrac{8}{10} \cdot (d - 70) + 1 & |70 \leq d \leq 80 \tag{3.5} \end{cases}$$

where $F_x$ is the measured load which are used in further calculations, $F_r$ is the raw data load from the Instron tensile machine, $F_{zero}$ is the force required in newtons, and $d$ is the crosshead displacement in mm.
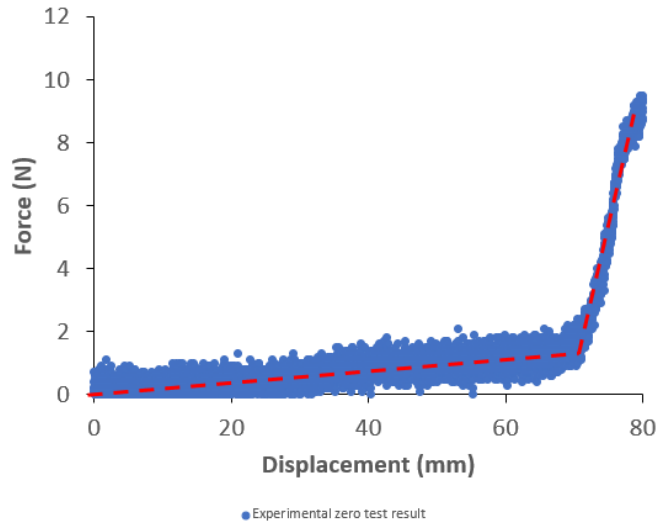
Figure 39 Calibration test results of picture-frame setup

Different crosshead speeds (10, 20 and 30 mm/min) were tested. Figure 40 compares the force and shear angle of the TG15N at those three crosshead displacements. The 30 mm/min tested samples showed some discrepancies compared to the other two speeds. The curves and variabilities of results at 10 and 20 mm/min of crosshead displacements were very similar. Considering the testing efficiency and accuracy, the crosshead speed of 20 mm/min was selected.
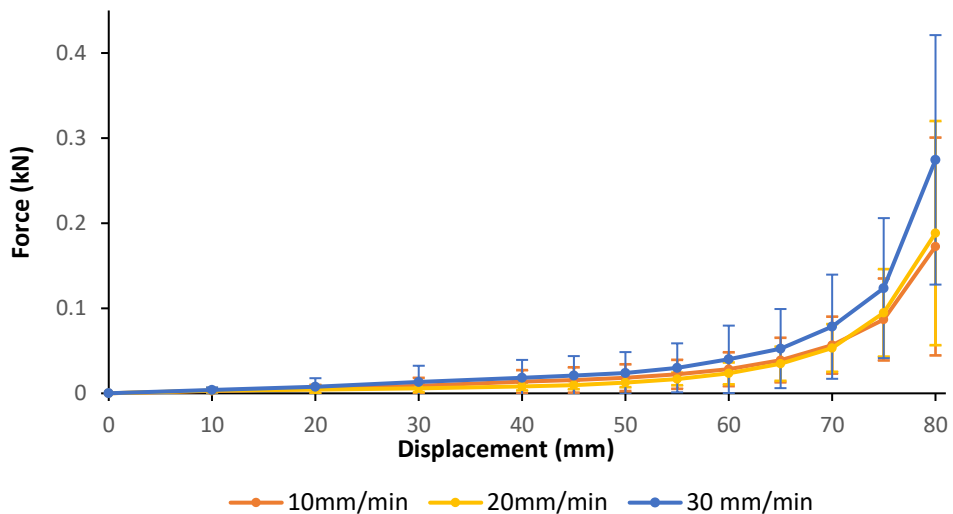


Figure 40 Average values and variability at different crosshead displacement rate of TG15N samples

Samples were tested in both positive (+45°) and negative (-45°) shear angle with respect to the warp orientation, to determine if the fabric architecture had an asymmetric shear behaviour as

mentioned in the literature [16, 19, 44]. Figure 41 shows the sample placed in the picture frame with the two possible orientations.



(a)                                                    (b)
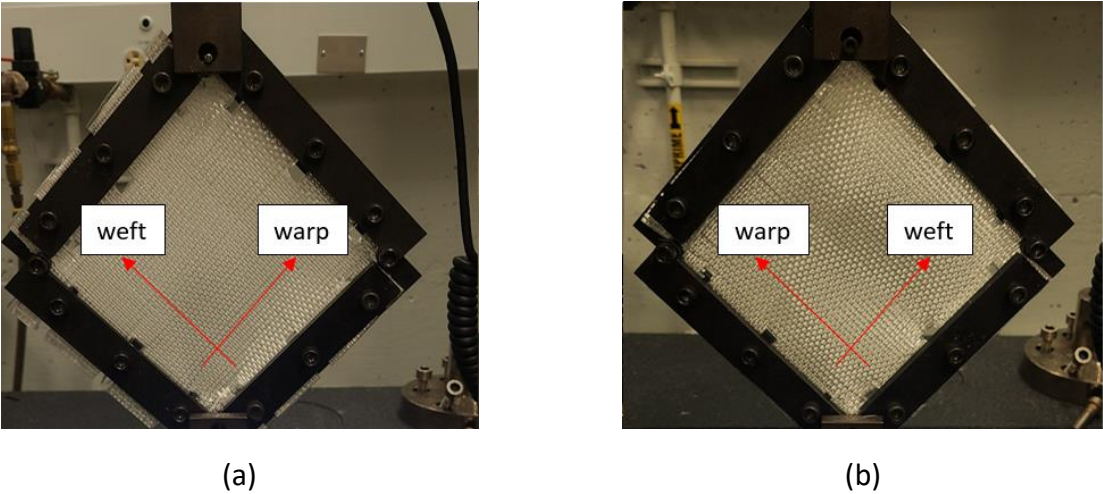
Figure 41 Sample orientations: warp direction or positive shear angle (a) and weft direction or negative shear angle (b)

Figure 42 shows the variation of the applied force as function of crosshead displacement for TG15N samples tested in the warp and weft directions. It can be observed that the shear behaviour of the NCF fabric is the same in both directions. Therefore, NCF samples were only tested in the positive shear angle direction for the following tests.
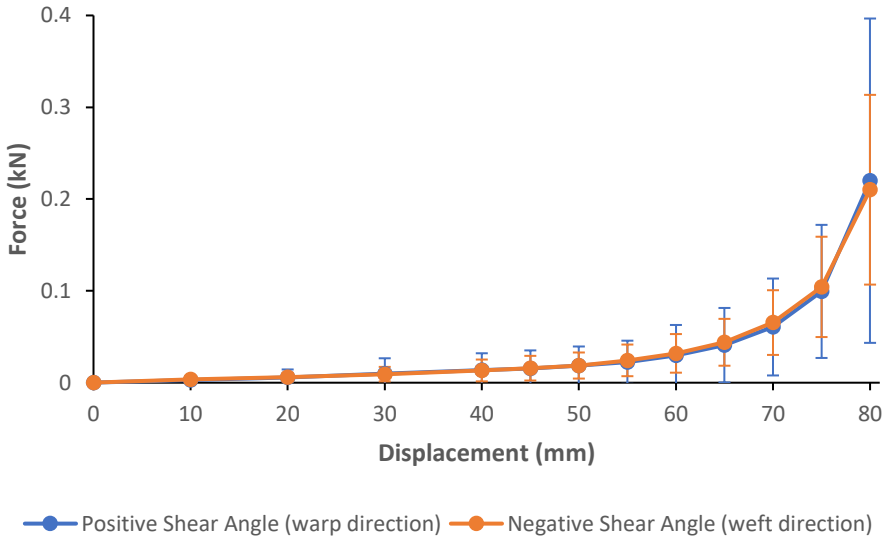


Figure 42 Shear behaviour for TG15N samples tested in positive and negative warp orientation

The shear stress ($\tau$) and strain ($\gamma$) were calculated using the following equations [26, 40]:

$$\tau = \frac{2 \cdot F_x \cdot \cos(^{\alpha}/_2)}{T_h \cdot L} \tag{3.6}$$

$$\gamma = \frac{\pi}{2} - \alpha \tag{3.7}$$

where $F_x$ is the measured load, $T_h$ is the thickness of the fabric, $L$ is the arm length of the picture-frame and the $\alpha$ is the angle between two adjacent arms at the top corner. The equations can be transformed using these trigonometric relationships:

$$\cos(^{\alpha}/_2) = \frac{H + \frac{d}{2}}{L} \tag{3.8}$$

$$\alpha = 2 \cdot \cos^{-1}(\cos(^{\alpha}/_2)) \tag{3.9}$$

where $H$ is the length of the side adjacent to the angle and $d$ is the crosshead displacement as shown in Figure 43. The transformed equations are:

$$\tau = \frac{2 \cdot F_x \cdot \left(\frac{H + ^{d}/_2}{L}\right)}{Th \cdot L} \tag{3.10}$$

$$\gamma = \frac{\pi}{2} - 2 \cdot \cos^{-1}\left(\frac{H + ^{d}/_2}{L}\right). \tag{3.11}$$

These equations allow to have only raw data ($F_x$ and $d$) as variables and the rest ($T_h$, $L$, and $H$) as constants to calculate the shear stress and strain.
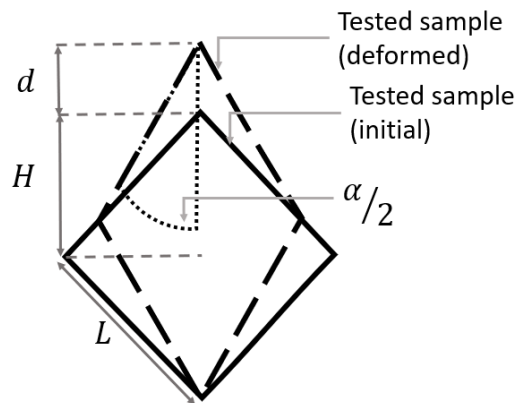


Figure 43 Geometrical parameters of the picture frame setup

Finally, the shear angle ($\theta$) can be calculated from the shear strain ($\gamma$):

37

$$\theta = \gamma \cdot \frac{180}{\pi}.$$

(3.12)

### 3.3.2   Material Preparation

Masking tape was applied at the clamping region of the sample to prevent fibre fraying and misorientation (Figure 44). The masking tape did not affect the tested region. Applying the tape facilitated the sample preparation time as well as improved the test reproducibility.
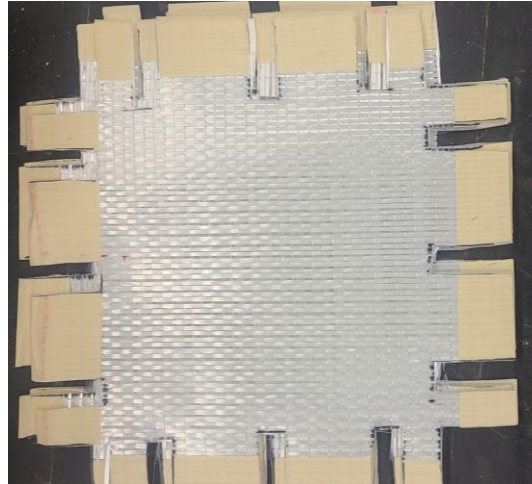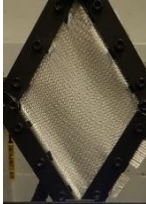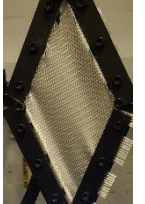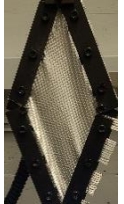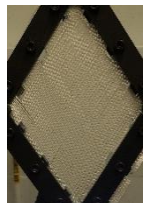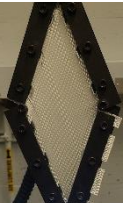


Figure 44 Picture-frame sample geometry with masking tape applied on clamping area

During the first sessions of picture-frame tests, the manipulation of the samples was not delicately done. Due to this effect, when tested under same condition, half of the tested samples showed wrinkles (Table 5). The resulting load and displacement were also significantly different as shown in Figure 45. As described in the literature, picture-frame test setup is prone to wrinkles [15, 20-22]. Those wrinkles were causing relaxation on the samples which does not illustrate the pure shear behaviour. Thus, once the wrinkles were apparent, the results were discarded.

Table 5 Example of progression of the picture-frame test at specific displacements with and without wrinkles

| Θ (°) /Disp (mm) | 23.9/40 | 39.4/60 | 49.0/70 | 61.7/80 |
|---|---|---|---|---|
| **With wrinkles** | | | | |
| **Without wrinkles** | | | | |
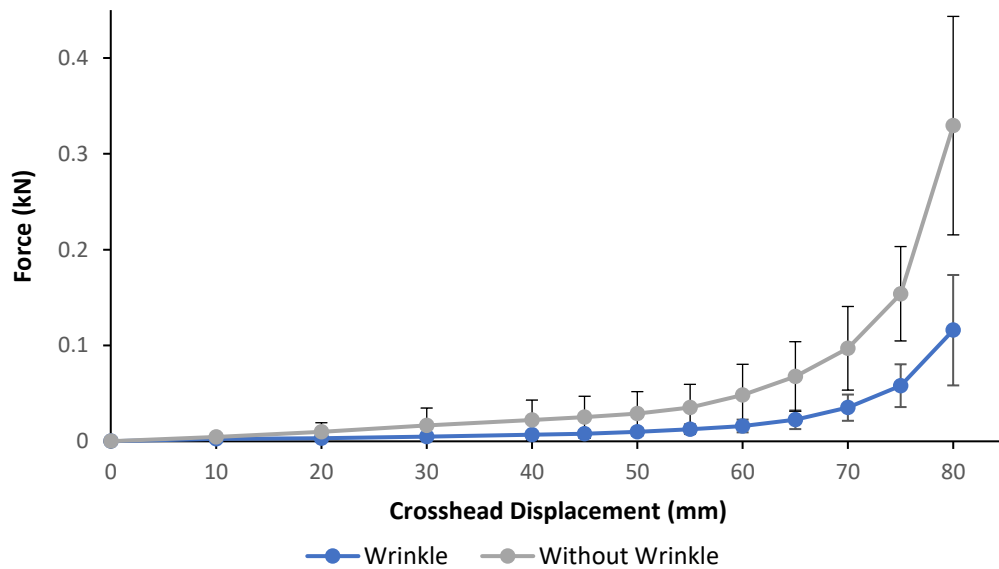


Figure 45 Picture-frame test result of TG15N with and without wrinkles

By analyzing the samples, it was observed that inconsistent spacing at the sample corners as well as initial wrinkling caused by sample deflection during handling were the main causes of the wrinkle initiation during the test.

Following these observations, sample preparation was then done with very high care resulting in less variability during the picture frame test. No wrinkle was initiated during the following sets of tests.

### 3.3.3   Picture-Frame Test Results

At least three samples for each material were tested. The average values of the picture-frame test are plotted in Figure 46. The load required to pull on the fixture determined from the calibration test was subtracted from the raw data.
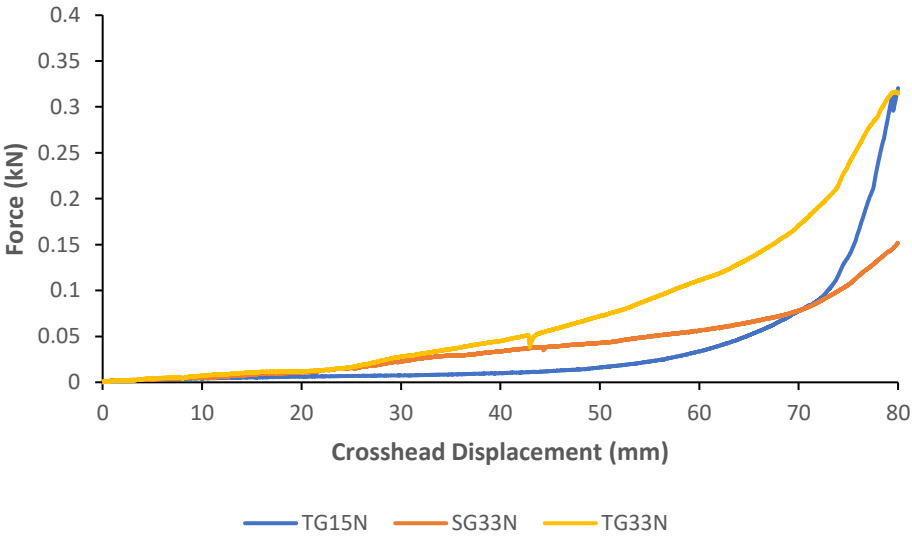


Figure 46 Average of Picture-Frame Test Results for TG15N, SG33N, and TG33N

Using Equations (3.10) and (3.11), the shear stress and strain calculated from the picture-frame results (Figure 46) are illustrated in Figure 47.
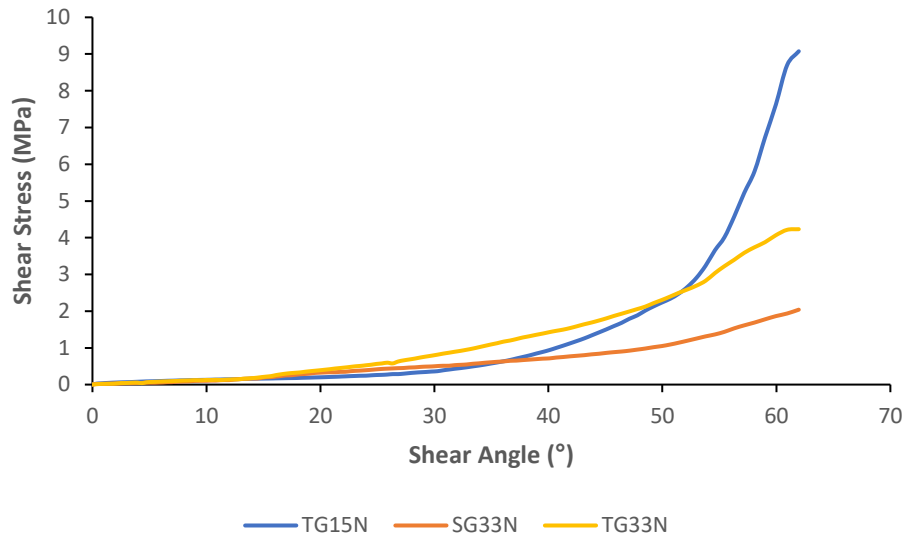
Figure 47 Comparison of the shear behaviour measured for TG15N, SG33N, and TG33N

From the shear stress – strain curves (shown in the Figure 47), the NCF locking angle can be determined at the intersection of the two tangents of the curve inflection [15, 43]. Figure 48 presents an excel tool that was developed to easily visualise the locking angle as well as the two shear moduli (pre and post locking angle). Several inputs were required: the measured shear strain, the measured shear stress and the range of the two tangents. The detailed explanation of each item of the excel tool is described below:

- Item 1: It corresponds to the range of the two tangents. These four cells are determined visually by the user. L1 represents the first linear region and L2 represents the second linear range. The boundaries min and max in radian for each range were used as inputs. These boundaries allow to split the input shear stress and angle cloud of points into two different arrays.

- Item 2: Slope and Y-intercept are determined by using built in functions "Slope" and "Intercept" respectively in GPa. The inputs of the functions are the two different arrays determined using the ranges from item 1. Various ranges were tested until the highest linearity using the R Square formula (built in "RSQ" function) was obtained. The RSQ cells were color scaled so that a linearity close to 1 was shown in green while a linearity close to 0 is in red. Slope values (Slope 1 and Slope 2) are equal to the shear moduli of the two linear regions. Slope 1 is the shear modulus before the locking angle and Slope 2 is the

41

shear modulus after the locking angle. The locking angle (Locking A) corresponds to the intercept of the two tangents.

- Item 3: The three points required to illustrate the two moduli and the locking angle values are shown in item 3 and in orange in the graphic. The Strain 1 is set to be 0. The Strain 2 is the locking angle value from item 2. The Strain 3 is the maximum strain from the experimental data. The Stress 1 is set to be 0. The Stress 2 is the Slope 1 multiplied by the locking angle. Lastly, the Stress 3 is found by linear function using Slope 2 and at Strain 3.
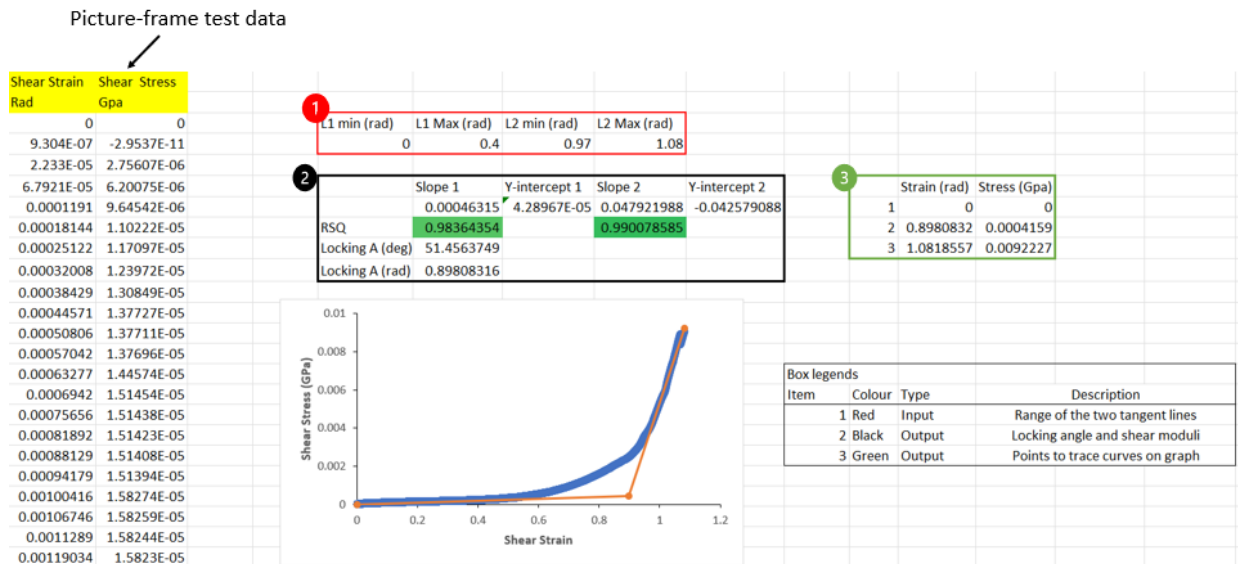


Figure 48 Shear moduli and locking angle calculation tool

With the shear moduli and locking angle, the shear properties of different materials can be numerically compared. The stress-strain curves of the 3 NCFs with their respective locking angles are shown in Figure 49 and the locking angles and shear moduli (pre and post locking angle) are reported in Table 6. From the picture frame test and the calculation of the locking angle, TG15N seems to have the best drapability behaviour in shear with the highest locking angle.
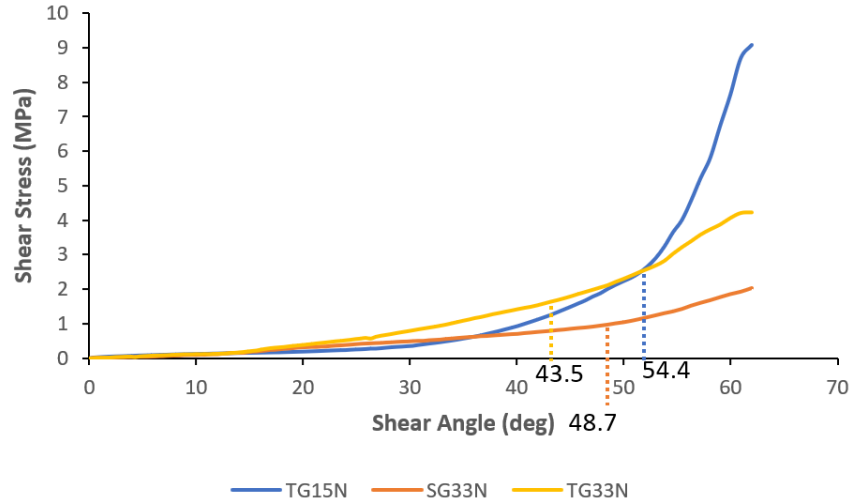
Figure 49 Comparison of the shear behaviour measure for TG15N, SG33N, and TG33N with locking angles

Table 6 Shear moduli and locking angles determined using the developed excel tool of each tested NCF

| Material | G1 (GPa) | Locking angle (°) | G2 (GPa) |
|----------|----------|-------------------|----------|
| TG15N | 5.274E-04 | 54.4 | 4.792E-02 |
| SG33N | 1.004E-03 | 48.7 | 5.077E-03 |
| TG33N | 1.414E-03 | 43.5 | 9.676E-03 |

The difference in locking angles between the three tested materials is mainly due to the difference in mesoscopic architecture. As SG33N and TG33N materials have thicker fibre tows compared to TG15N, there is less space between the fibres for them to freely rotate which result in lower locking angle.

### 3.3.4   Shear Property Implementation in PAM-FORM and Validation

There are three different methods to implement the shear behaviour in PAM-FORM.

1. Methodology 1: implement stress vs strain cloud of points obtained from the picture frame experimental test from Figure 47 (Figure 50)

2. Methodology 2: implement force vs displacement raw data obtained from the picture-frame experimental test from Figure 46 (Figure 51)

3. Methodology 3: implement shear moduli and locking angle calculated with the developed Excel tool and reported in Table 6 (Figure 52)
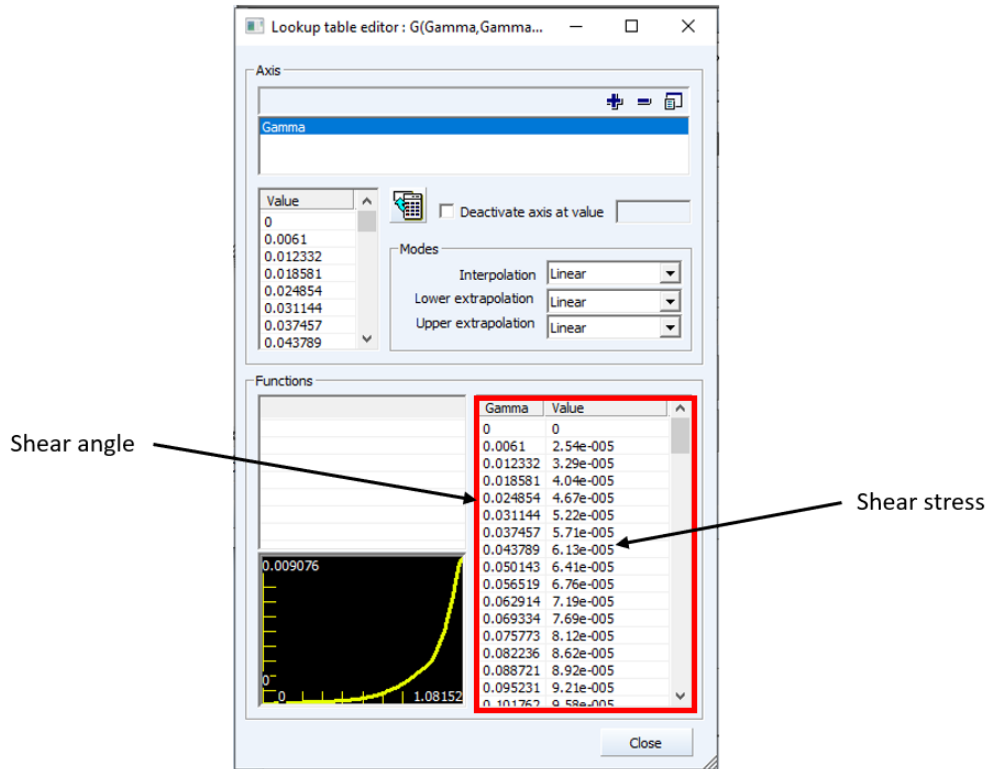
Figure 50 Methodology 1: Shear properties implementation by using calculated shear stress and strain values from the picture-frame test results
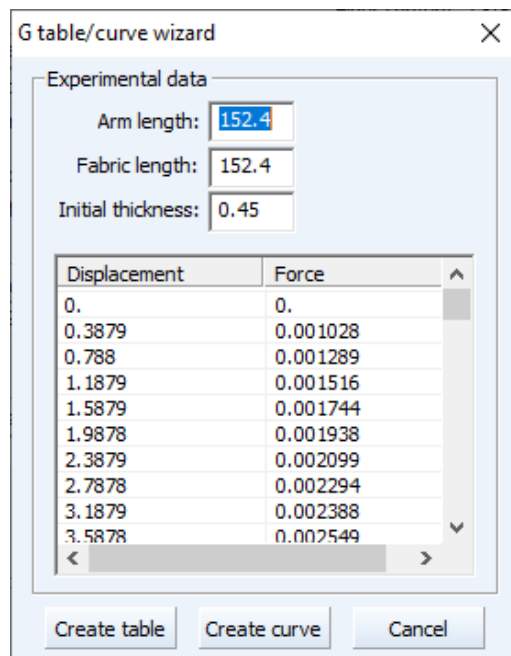


Figure 51 Methodology 2: Shear properties implementation by using force and displacement from picture-frame test
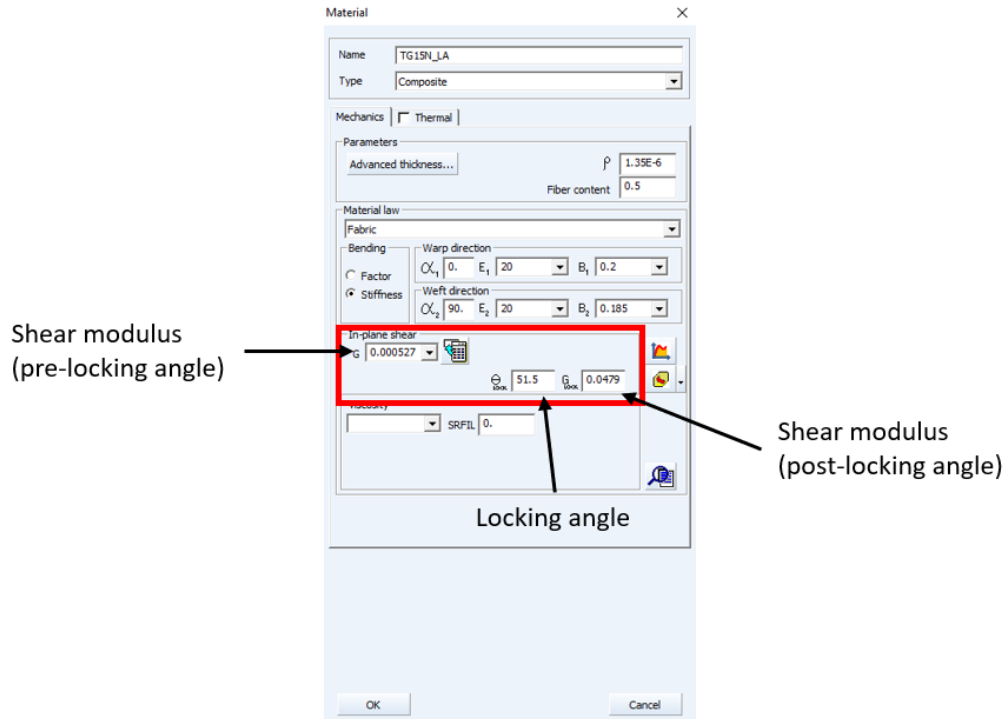
Figure 52 Methodology 3: Shear properties implementation by using shear moduli and locking angle

The validation of shear behaviour for each material with the three implementation methodologies was performed with a single element simulation with the boundary conditions shown in the Figure 53: three imposed displaced nodes (arrows) and one fixed node. The imposed displacement of the top node ($U_y$) in the vertical direction corresponds to the crosshead displacement of the load cell. The two imposed displacements ($u_x, u_y$) of the side nodes in diagonal directions were kinematically coupled with the vertical displacement. The single element simulation allowed to keep the four edges straight while getting the representative reaction force and displacement of the top node. The reaction force and the displacement of the top node were compared with the picture-frame experimental force-displacement curves obtained for each material as suggested by Lebrun et al. [46]. The relationships between the imposed displacements are defined with the following equations:

$$u_y = {U_y}/{2} \tag{3.13}$$

$$u_x = L \cdot \left( \frac{\sqrt{2}}{2} - \sin\frac{\alpha}{2} \right) \tag{3.14}$$

where $U_y$ is the imposed displacement at top corner, $u_x$ and $u_y$ are the imposed displacements in x and y directions respectively, $L$ is the armlength of the picture-frame, and $\alpha$ is the angle between two adjacent arms at the top corner.
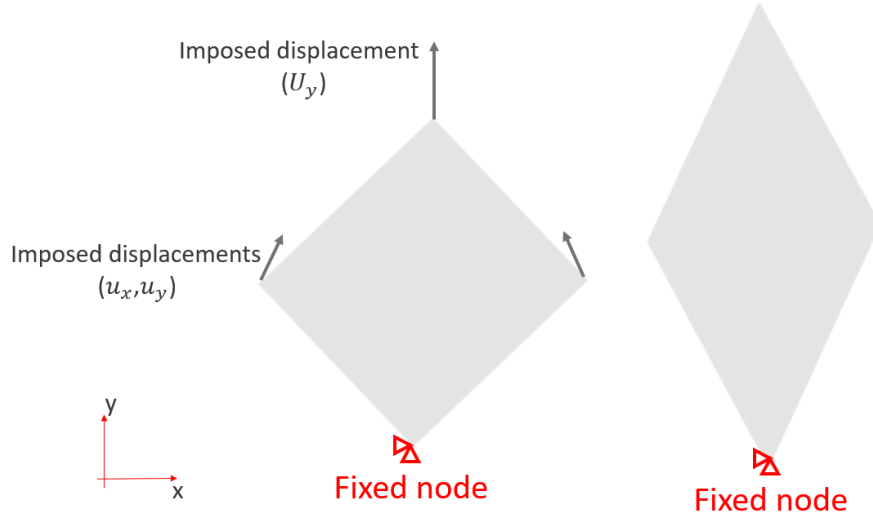


Figure 53 Picture-frame validation method with boundary condition (left) and deformed shape (right)

Comparison from simulation by using implementation methodology 1 (calculated shear-strain) is shown in Figure 54. The simulation results of methodology 2 (force-displacement from picture-frame) resulted in the same numerical values for the force-displacement curves as the simulation results shown in Figure 54. PAM-FORM uses the same equations (3.6) and (3.7) for shear stress strain calculation. Good correlations with very high confidence level can be observed for all three materials with $R^2$ value above 0.96.
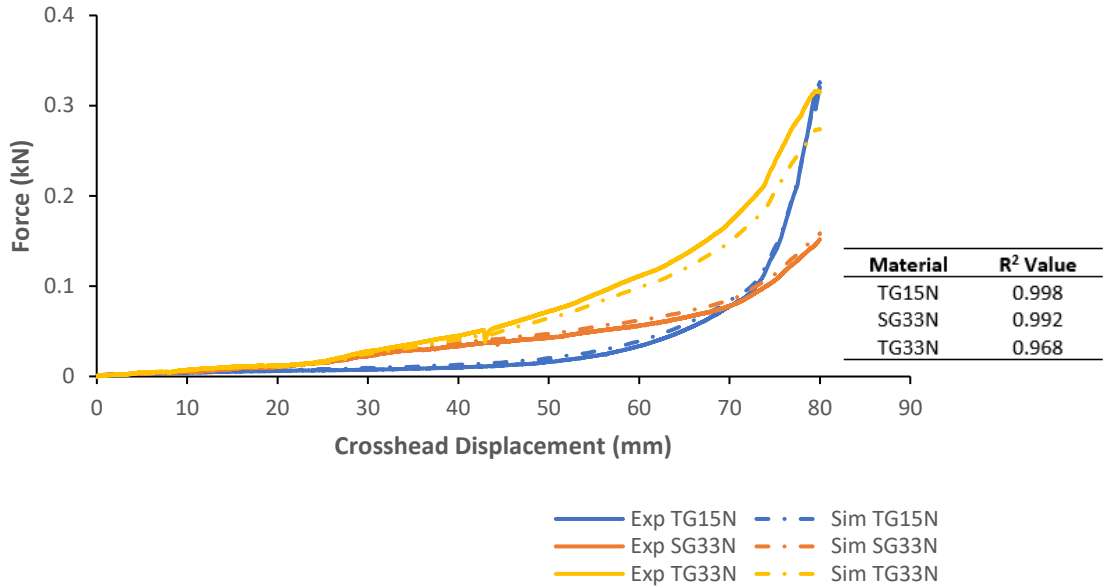
Figure 54 Comparison of force and crosshead displacement between simulation and experimental results for the picture frame test of methodologies 1 with $R^2$ values

Similar comparison was performed with implementation methodology 3 (two moduli and locking angle). The comparison is plotted in Figure 55. Methodology 3 simplifies the material shear behaviour to 2 linear regions and 1 intercept. The correlations were not as great as the other two implementation methodologies. All three materials have $R^2$ value below 0.90. For more accurate results, the author highly suggests to directly implement the experimental curves obtained with the picture frame test in PAM-FORM, as show in methodologies 1 and 2.
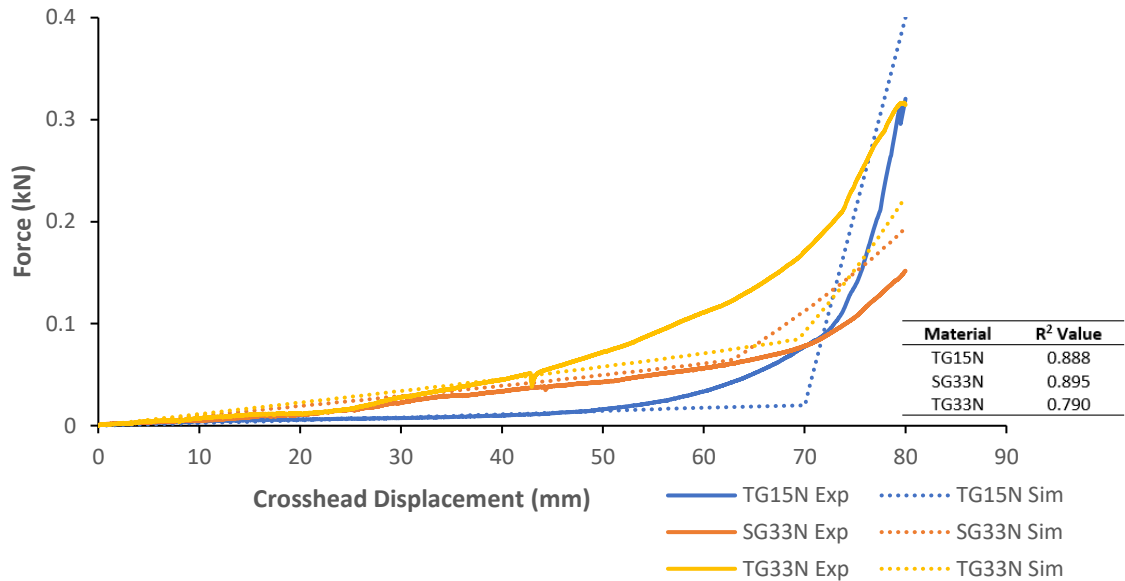
Figure 55 Comparison between simulation and experimental force and displacement results for implementation methodology 3 with $R^2$ values

## 3.4 Out-of-plane Bending

### 3.4.1 Bending Cantilever Test Methodology

The Fabric Stiffness Tester Model 112 from Taber® Industries (Figure 56) was used to measure the out-of-plane bending stiffness. In theory, the width of the sample should not affect the out-of-plane bending results. Maximum sample width corresponds to the width of the surface of the tester. Minimum width depends on the type of tested material. For NCF, if the width of the sample is too narrow, then fibre fraying at the edge of the sample becomes significant and can affect the test results. By trial-and-error, the optimal width was set to 25.4 mm.

Three overhang lengths (80 mm, 110 mm and 130 mm) were tested based on the minimum and maximum lengths that could be tested with the apparatus. Both bending properties along warp and weft directions were measured. For each sample, side view picture of the specimen was taken. An example is shown in Figure 56. The sample deflection and the curvature profile were then analysed using "GetData Graph Digitizer" [59] image analysis software. Coordinates (X, Z) of the curvature profile were extracted to accurately determine deflection. The graphical user interphase (GUI) of the image analysis software is shown in Figure 57. The software first required a reference for the X and Z axes. The horizontal board and the vertical ruler were used to

reference the X and Z axes respectively. The red dots were manually placed on the curvature profile, and their coordinates were calculated from the reference X and Z axes and listed in the red box. These coordinates were then exported to excel as data points.
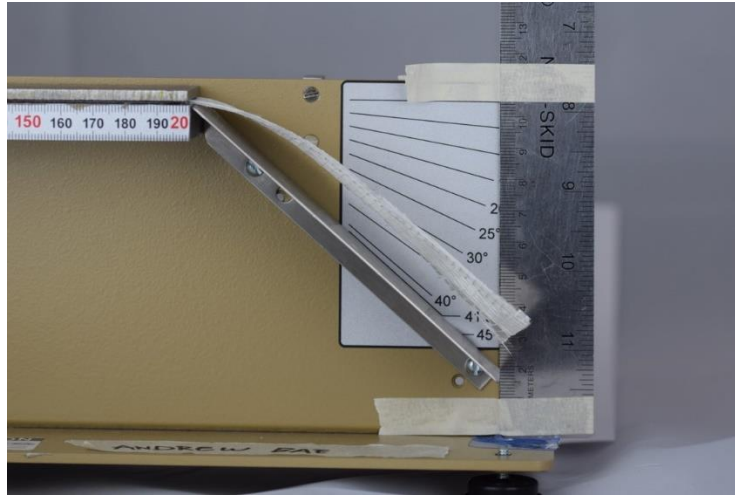


Figure 56 Bending cantilever setup (Taber® fabric stiffness tester)

1. Set X and Z axes
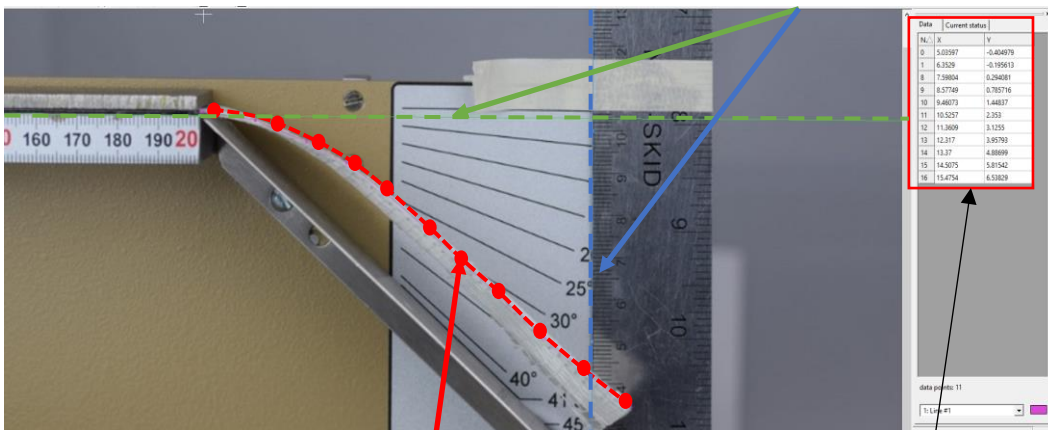


2. Manually collect data points of curvature          3. Export data points of curvature

Figure 57 Get Data Graph Digitizer GUI with steps to obtain coordinate points

The flexural rigidity (*G*) and bending modulus (*B*) were calculated using the following equations [38, 50, 51]:

$$G = g \cdot \rho_A \cdot c^3 \tag{3.15}$$

$$B = 12 \cdot \frac{G}{T_h{}^3} \tag{3.16}$$

$$\rho_A = \rho_V \cdot T_h \tag{3.17}$$

$$c = OL \cdot \left( \frac{\cos(\theta/2)}{8 \cdot \tan \theta} \right)^{1/3} \tag{3.18}$$

$$\theta = \sin^{-1} \left( \frac{\delta}{OL} \right) \tag{3.19}$$

where $g$ is the gravitational acceleration, $\rho_A$ is the fabric areal weight, $T_h$ is the fabric thickness, $\rho_V$ is the fabric volumetric density, $\theta$ is the angle created between the deflection ($\delta$) and ($OL$), and finally $c$ is the bending length. The different variables are illustrated in Figure 58. Peirce first introduced the concept of the bending length as the length of fabric that will bend under its own weight during the cantilever test [50]. It mathematically relates the overhang length to the fabric's flexural stiffness. The relationship between the bending length and the overhang length was developed based on elastic theory and corrected with empirical data. About twenty measurements for each sample at each $OL$ were tested and the average value of bending moduli was taken.
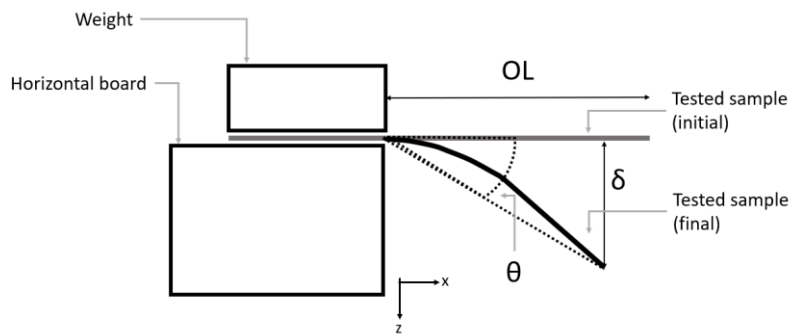


Figure 58 Bending behaviour characterisation test setup

### 3.4.2 Material Preparation

Due to the nature of the fabric, strips of fibres were easily fraying while cutting the fabric. This phenomenon happened more critically when the fabric was cut along the weft direction (Figure 59), leading to non-homogeneous samples and large discrepancy from one sample to another.

Sample non-homogeneity affected the results by creating a twisting effect of the sample (Figure 60) and uneven deflection points. Results were discarded when this happened.
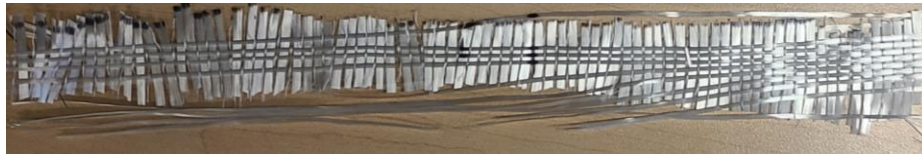


Figure 59 Instability of fibres along the weft direction
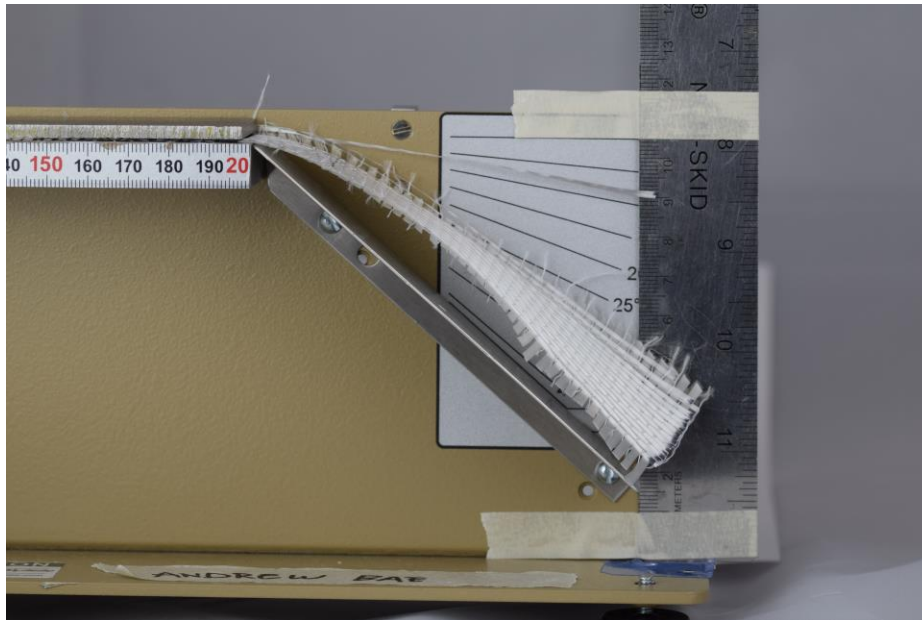


Figure 60 Twisting effect during cantilever test due to uneven distribution of fibres

Several attempts to improve sample consistency were tested by applying different types of tapes (Teflon, masking, dry-wall) at the edge of the fabric or the entire coupon itself to prevent fibre fraying. Example of a sample with dry-wall tape applied at the edge of bending sample is shown in Figure 61. During the studies, addition of these tapes reduced sample variability, but significantly changed the sample stiffness, resulting in a 20 to 30% increase in the bending modulus.



Figure 61 Dry-wall tape applied at the edge of fabric to reduce fraying

Thus, to improve the test results, fabric cutting and sample manipulation were performed very delicately, without the addition of tape.

### 3.4.3    Bending Cantilever Test Results

Figure 62 compares the bending behaviour of the three tested NCFs at different overhang lengths. No significant variation of the bending modulus with the overhang lengths was observed. The modulus values and the average values for each material in both directions are reported in Table 7.
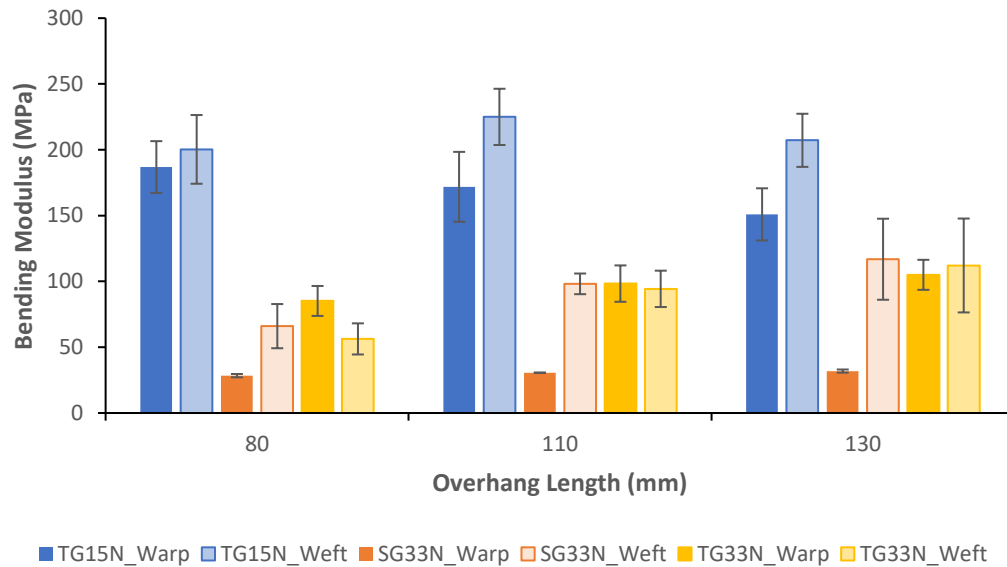


Figure 62 Bending modulus results as a function of the overhang length and fabric orientation for the tested NCFs

Table 7 Bending modulus of each material at different orientations and overhang lengths

| Material | Orientation (°) | Bending Modulus (GPa) | | | |
|---|---|---|---|---|---|
| | | 80 mm | 110 mm | 130 mm | Average |
| TG15N | Warp 0 | 0.1869 | 0.1719 | 0.1509 | 0.1699 |
| | Weft 90 | 0.2003 | 0.2250 | 0.2072 | 0.2108 |
| SG33N | Warp 0 | 0.0284 | 0.0306 | 0.0319 | 0.0303 |
| | Weft 90 | 0.0660 | 0.0981 | 0.1168 | 0.1000 |
| TG33N | Warp 0 | 0.0852 | 0.0983 | 0.1050 | 0.0977 |
| | Weft 90 | 0.0563 | 0.0943 | 0.1121 | 0.0958 |

Figure 63 shows the flexural rigidity results at different overhang lengths for both warp and weft directions. Higher flexural rigidity can be observed for SG33N, followed by TG33N mainly due to the difference in thickness of the materials. Also, contrary to TG15N and TG33N, the bending behaviour of SG33N in the warp and weft direction is significantly different. Lower bending modulus was measured in the warp direction due to thermoplastic binder stitch.

Flexural rigidity of the fabric is used to calculate the bending modulus of the material but is also link to the material wrinkle formation. From the literature [22, 23], high flexural rigidity material has shown to create larger wrinkle size but lower flexural rigidity material is more prone to wrinkles. From these results, it can be assumed that SG33N would create the largest wrinkles due to highest flexural rigidity (in the weft direction) and TG15N would be more prone for wrinkles due to low flexural rigidity. Also, SG33N would result in largest bridging due to its high flexural rigidity.
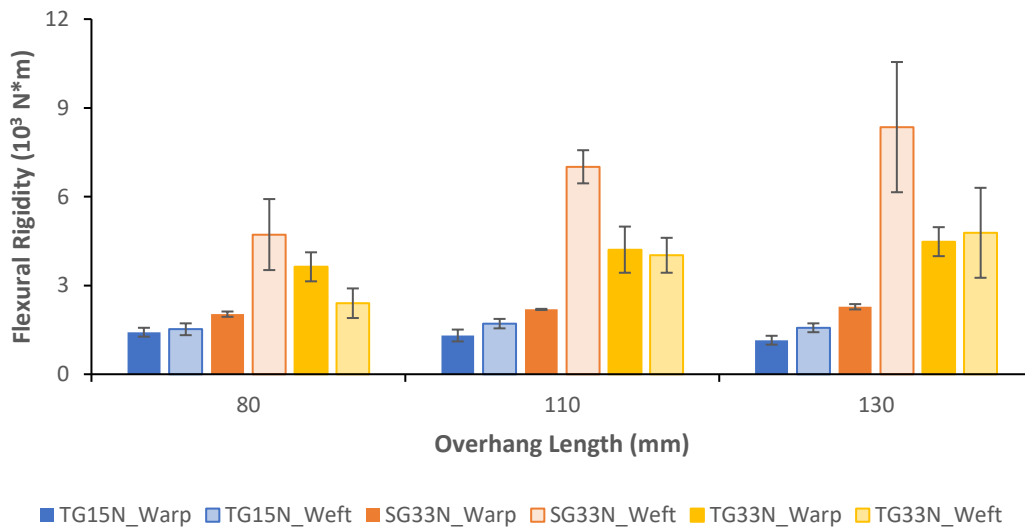


Figure 63 Flexural rigidity results as a function of the overhang length and fabric orientation for the tested NCFs

### 3.4.4   Bending Property Implementation in PAM-FORM and Validation

In PAM-FORM, there are two possible methods to implement bending modulus:

1.  Constant bending modulus (Figure 64)
2.  Variable bending modulus in function of radius of curvature (Figure 65)

53
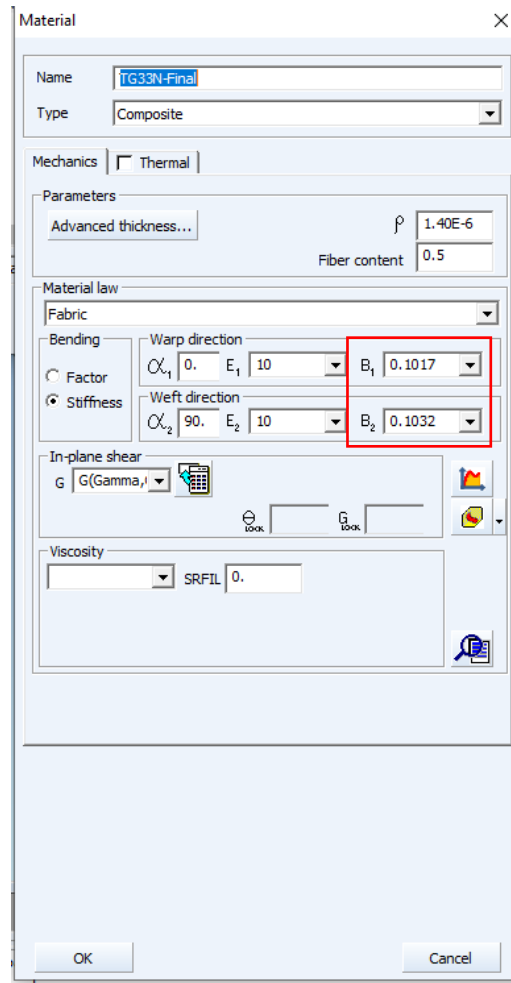
Figure 64 Implementation of bending properties as constant bending modulus
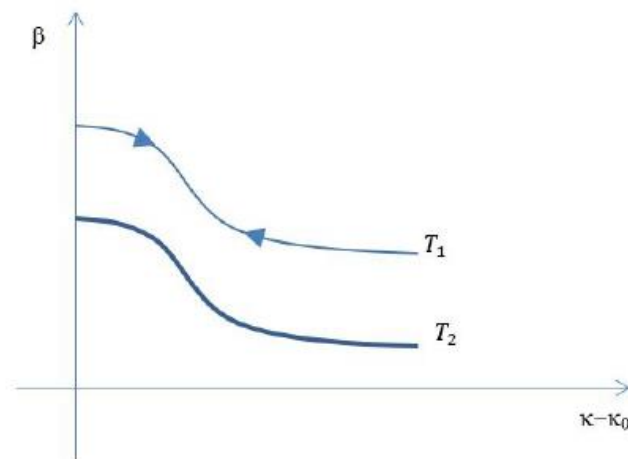


Figure 65 Implementation of bending properties (β in figure) in function of bending curvature (κ in figure) [17]

The bending properties were validated by modelling the bending cantilever test in PAM-FORM as shown in Figure 66. A rectangular model was created with a fixed edge on one side. Gravitational force was applied to the rest of the elements. From the simulation, the curvature profile was extracted and compared to the experimental curvature profile obtained with the cantilever test.

The bending moduli from Table 7 were implemented in the model in as a constant modulus value in both warp and weft directions. Comparisons between experimental (extracted using "GetData Graph Digitizer") and numerical (extracted from PAM-FORM) bending curvature profiles are shown Figure 67 to Figure 69 and their respective $R^2$ values are reported in Table 8 to Table 10. Good correlations for all three materials can be observed with an average $R^2$ values of 0.962 for each overhang length.
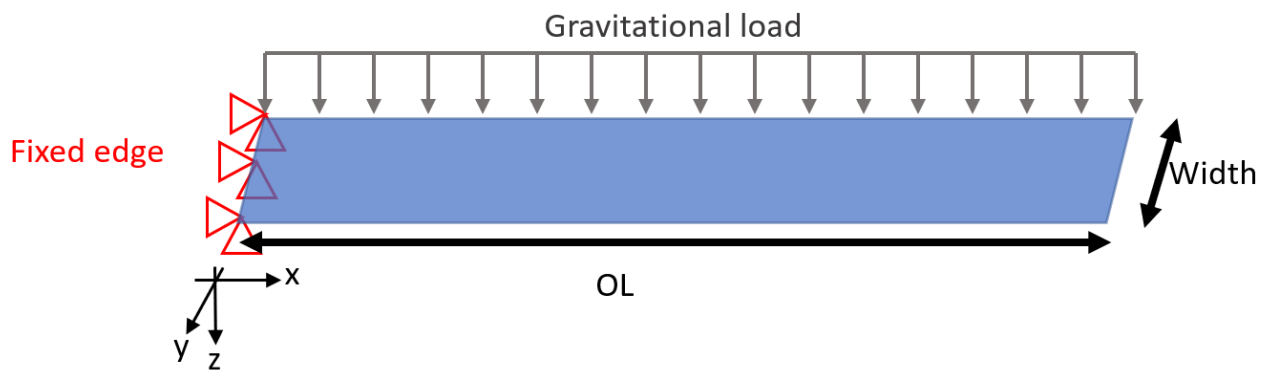


Figure 66 Bending validation simulation boundary condition
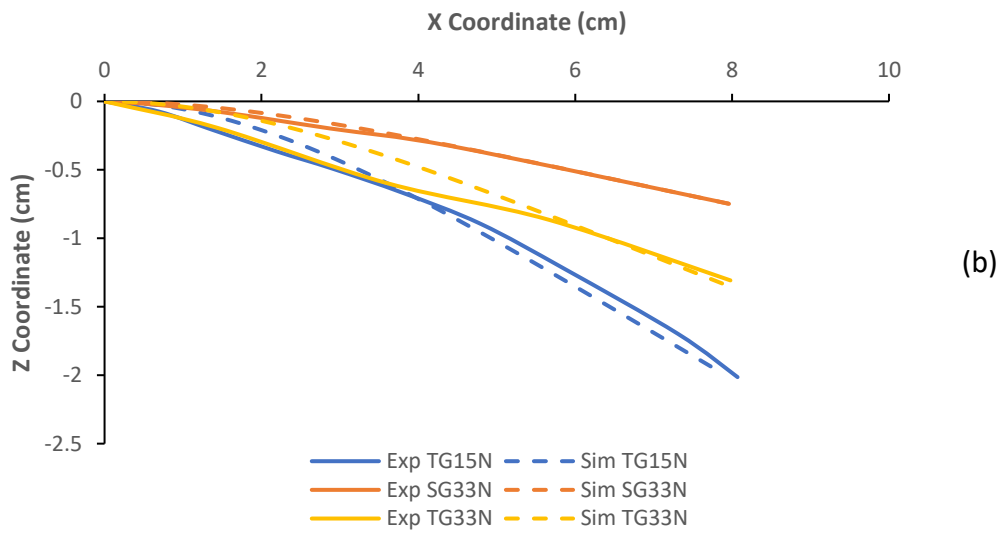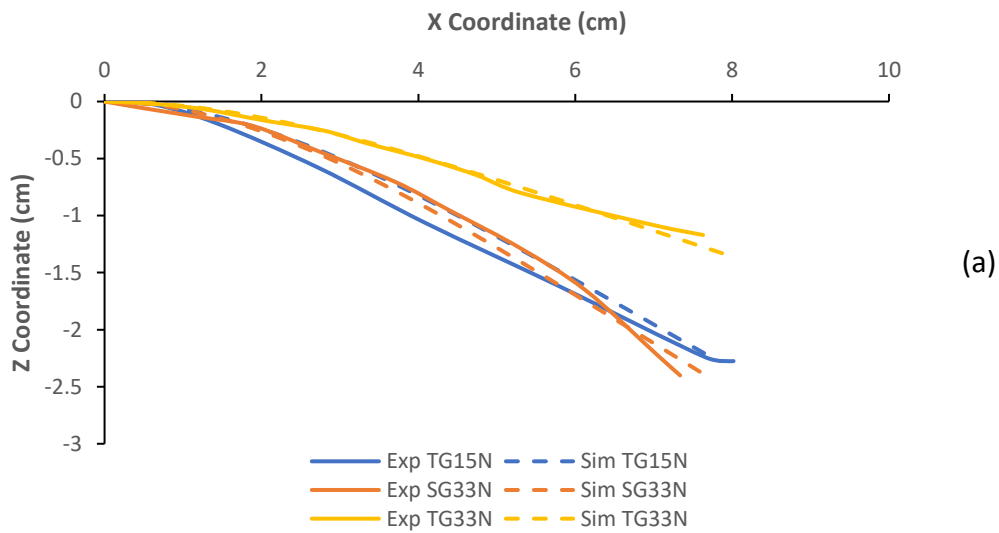
Figure 67 Bending curvature comparison for each material at OL = 80 mm at warp direction (a) and weft direction (b)

Table 8 $R^2$ values of bending curvature comparison for each material at OL= 80 mm

| | R² Value | |
| --- | --- | --- |
| Material | Warp | Weft |
| TG15N | 0.982 | 0.985 |
| SG33N | 0.990 | 0.993 |
| TG33N | 0.989 | 0.917 |

(a)



(b)
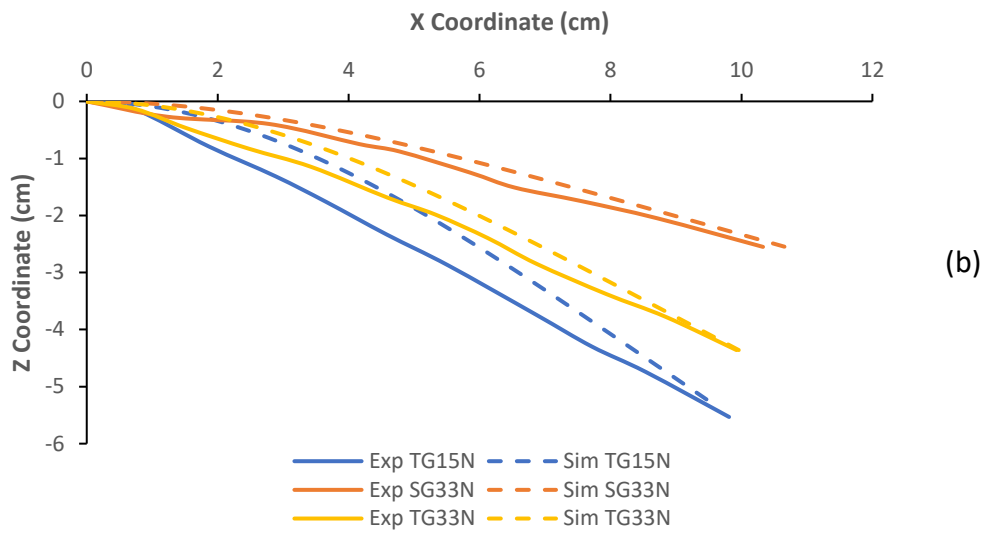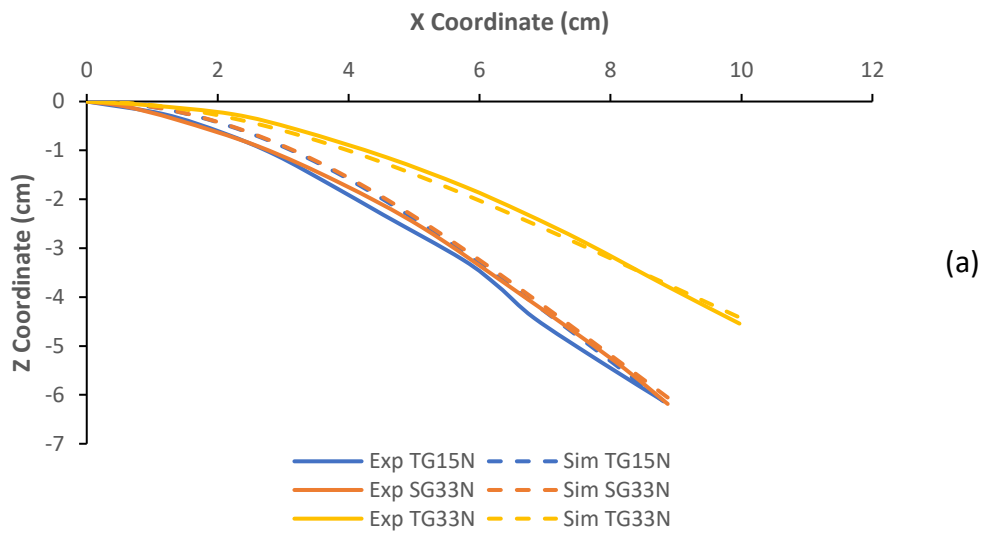
Figure 68 Bending curvature comparison for each material at OL = 110 mm at warp direction (a) and weft direction (b)

Table 9 $R^2$ values of bending curvature comparison for each material at OL = 110 mm

| | R² Value | |
| Material | Warp | Weft |
|---|---|---|
| TG15N | 0.987 | 0.909 |
| SG33N | 0.996 | 0.939 |
| TG33N | 0.995 | 0.948 |

(a)

(b)
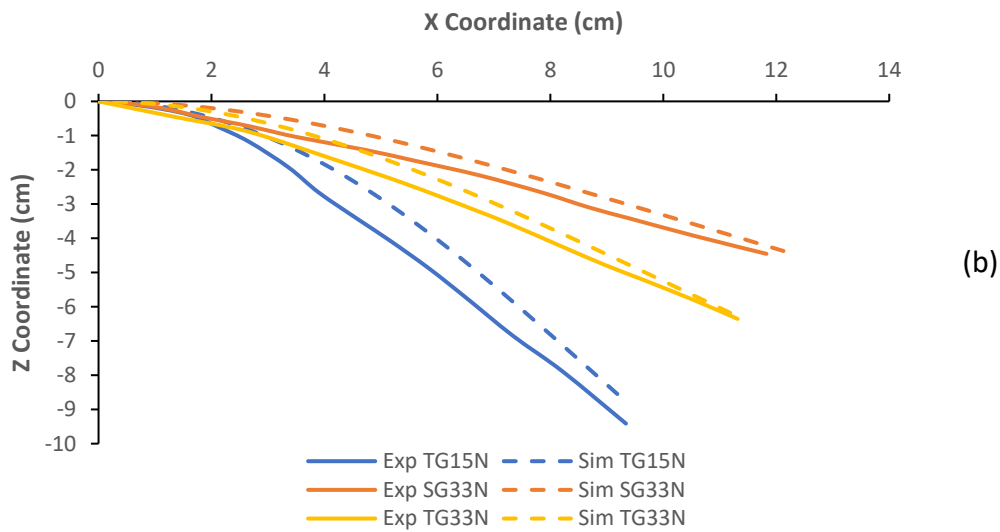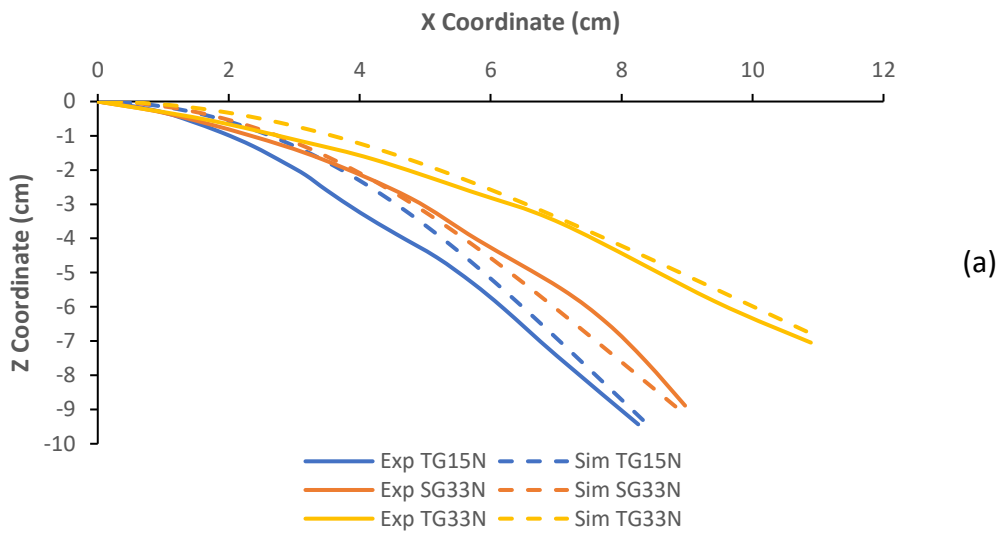
Figure 69 Bending curvature comparison for each material at OL = 130 mm at warp direction (a) and weft direction (b)

Table 10 $R^2$ values of bending curvature comparison for each material at OL = 130 mm

| | R² Value | |
|---|---|---|
| Material | Warp | Weft |
| TG15N | 0.953 | 0.929 |
| SG33N | 0.977 | 0.939 |
| TG33N | 0.981 | 0.964 |

The average $R^2$ values of bending curvature comparisons at both warp and weft directions for the three tested materials are shown in Table 11. There are higher deviations in the comparisons in the weft direction. This is due to instability of fibres along the weft direction as previously discussed in Section 3.4.2.

Table 11 Average $R^2$ values of bending curvature comparison at warp and weft directions

| Material | $R^2$ Value | |
| --- | --- | --- |
| | Warp | Weft |
| TG15N | 0.974 | 0.941 |
| SG33N | 0.988 | 0.957 |
| TG33N | 0.988 | 0.943 |

## 3.5   Discussion

The shear and bending behaviours of NCF (TG15N, SG33N, and TG33N) reinforcements was experimentally characterised and implemented in PAM-FORM preforming software. The NCF material data cards were validated by modelling the shear and bending characterisation tests and comparing experimental and numerical results. Good correlations were obtained for both behaviours with average $R^2$ values of 0.986 for shear and 0.962 for bending.

The comparisons of drapability behaviours of the three NCF fabrics are shown in Figure 70. TG15N seems to have the best drapability properties for shear with highest locking angle (54.4°) followed by SG33N (48.7°) and TG33N (43.5°). However, TG15N has the lowest flexural rigidity which makes it more prone to wrinkles. Due to low flexural rigidity, the material is suitable for parts with large grooves (to reduce bridging) or with large curvature. TG15N is best suitable for a complex design part. SG33N also has a high locking angle and relatively low flexural rigidity in the warp direction. By placing the fabric such that the warp direction is in parallel to curvature's tangential direction, this material could also be a great option for preforming complex geometry. Also, the thermoplastic binder, integrated in its architecture, could be directly used as fabric binder to simplify the preforming process and reduce manufacturing time. The other advantage of SG33N and TG33N is their thickness. The advantage of using thicker material is the deposition rate. The higher the deposition rate is, there is a reduction of manufacturing time by reducing the occurrence of layering up the fabrics and of binder application.
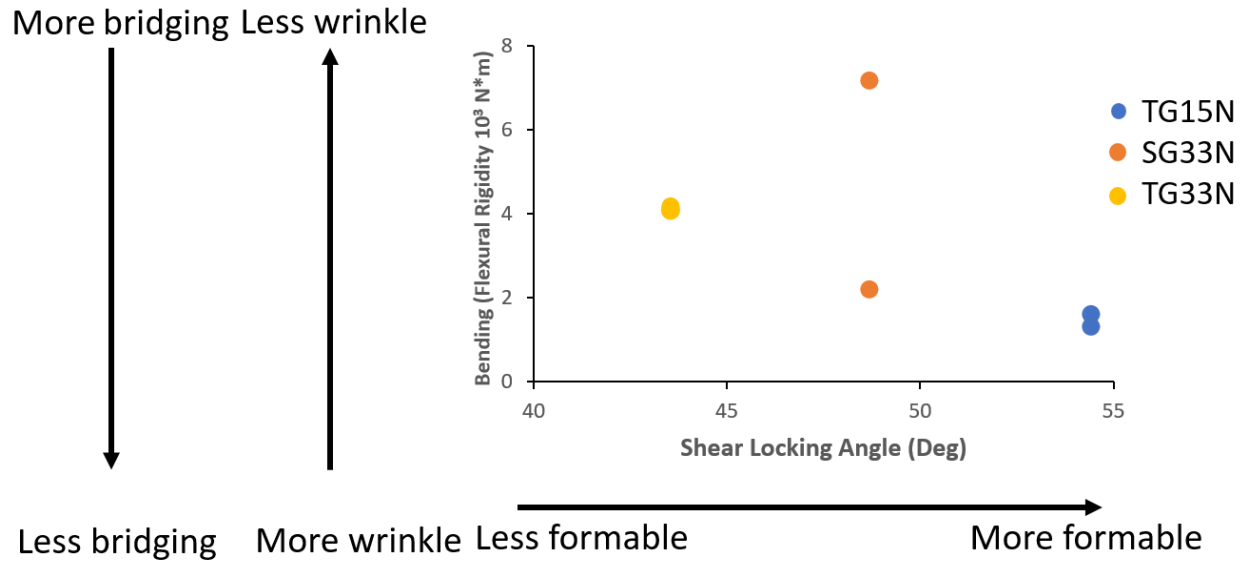
Figure 70 Material behaviours comparison chart of TG15N, SG33N, and TG33N

For the tensile behaviour of the three materials, their properties were directly taken from the literature. As the fabrics all have same E-Glass fibres, the tensile modulus was estimated to be 70 GPa [60]. The coefficients of friction for intra-ply friction and for friction between tool and fabric were both estimated to be 0.2 using the assumption from several other studies [13, 22, 56].

# 4 Preforming Simulation of Complex Geometry

This chapter presents the results of preforming simulation on complex geometry using the implemented material data card from Chapter 3. The membrane preforming simulation was used to validate material properties of the NCF implemented in PAM-FORM for a complex geometry setup. Two different validation methodologies were used to compare the experimental preforming results and the membrane preforming simulation: gridline and 3D scanning validation methodologies. The methodologies and results of the validation are discussed. Next, sensitivity analyses on tensile properties were performed and the effect on shear angle distribution was analysed. Also, flat pattern optimisation was carried out for a complex geometry and compared with another preforming simulation software.

## 4.1 Simulation Setup

Preforming simulation validations using PAM-FORM were carried out on a seatback demonstrator geometry (general dimensions X = 900 mm, Y = 500 mm, Z = 175 mm) designed by the NRC (Figure 71). This geometry has complex features such as deep grooves (15 mm) and double-curvature surfaces. The validation was performed by reproducing the seatback geometry experimental preforming on PAM-FORM simulation software.

(a)



Deep Groove

Section A-A

(b)
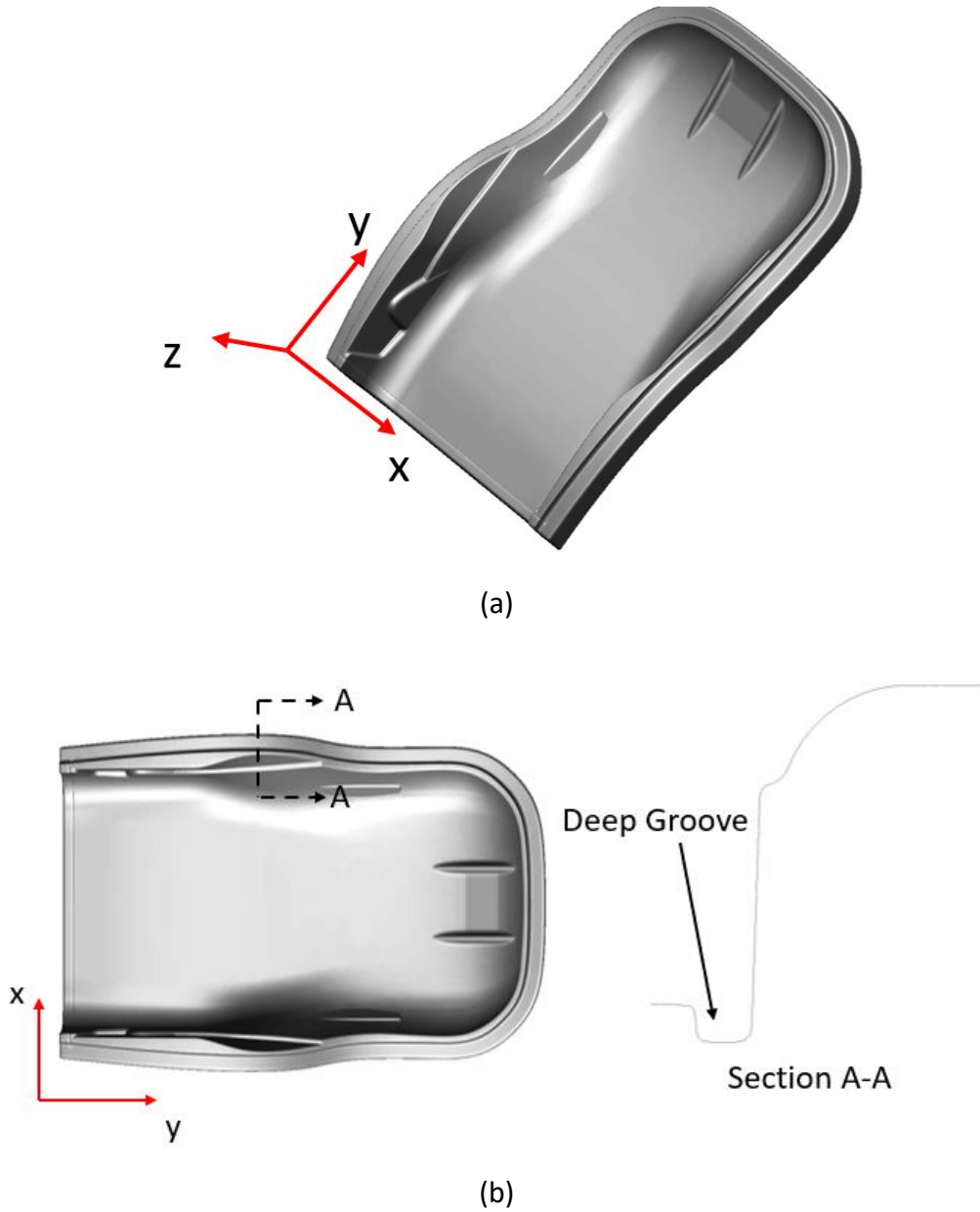
Figure 71 Seatback demonstrator geometry isometric view (a) and top and section view (b)

The shear and bending properties (Figure 47 and Table 7) of the three NCF reinforcements determined in the previous Chapter 3 were implemented in PAM-FORM preforming software as explained in the previous Sections 3.3.4 and 3.4.4. The tensile modulus of the E-glass fabric was estimated to be 70 GPa according to the literature [60]. The intra-ply friction coefficient and the coefficient of friction between tool and fabric were also both estimated to be 0.2 [13, 22, 56].

The seatback geometry simulations were performed using the male tool geometry. Two simulations were created: a membrane preforming simulation and a rigid match-die tool preforming simulation. In both cases, layers were created using the geometry file used to cut the fabrics on an automatic cutting table for the experimental validation (Section 4.2). At the beginning of each simulation, the layers were placed on the top of each other over the rigid tool using PAM-FORM "Positioning" feature. Then the rubber membrane or the female rigid punch-tool was placed on the top of layered fabrics. Figure 72 shows the position of the fabric layers (grey) and the tool (yellow).



(a)                                              (b)
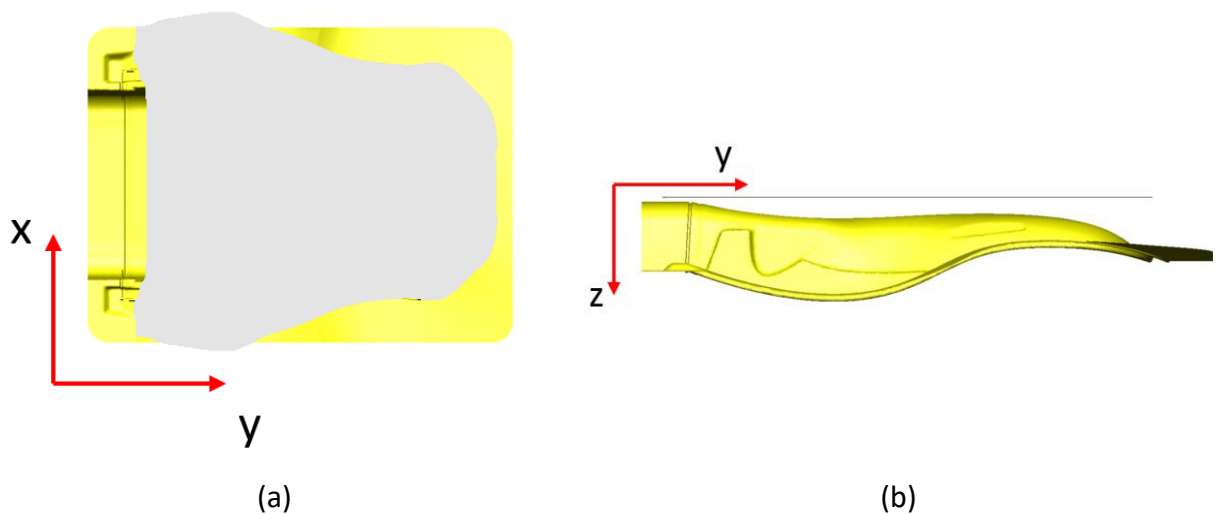
Figure 72 Layers of fabrics (in grey) and tool (in yellow) for membrane simulation: top view (a) and side view (b)

### 4.1.1 Membrane Simulation Setup

To perform the membrane preforming simulation, the membrane was first characterised. In the material database of PAM-FORM, a plastic material was already created which can be used as a membrane material. This material data card required one input property: the tensile modulus. To obtain this property, ASTM D412 tensile test was performed on the rubber membrane material. The material was provided by the CTA and unfortunately, no specific information on the rubber material was available. Eight samples of rubber membrane materials were tested. The tensile behaviour of the membrane material is shown in Figure 73. The average Young's modulus measured from the tensile test was 1.20 MPa. In PAM-FORM software, the rubber material was categorised as a "Trim" material.
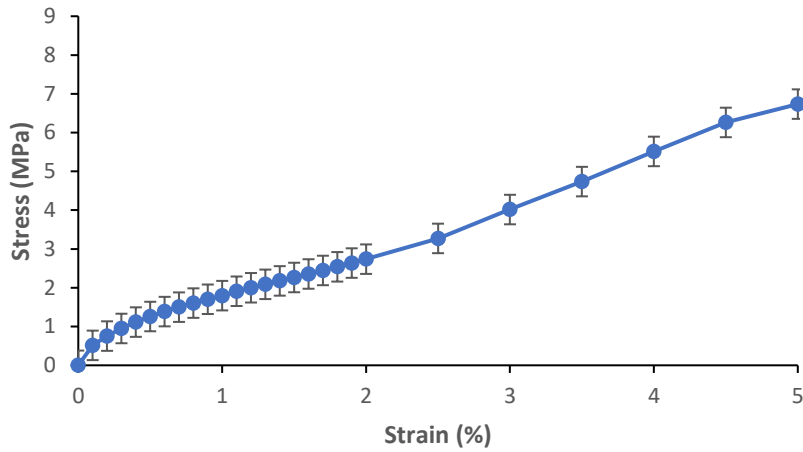
Figure 73 Tensile test result of rubber membrane material

Figure 74 shows the position of the membrane (cyan) relative to the fabric layers (grey) and the tool (yellow). The preforming boundary conditions were applied by setting different combinations of membrane velocity and pressure boundary. The boundary condition is reported in Figure 75. The speed and the pressure were applied on all nodes of the membrane. The progression of TG15N membrane preforming is shown in Table 12.



(a)                                                            (b)
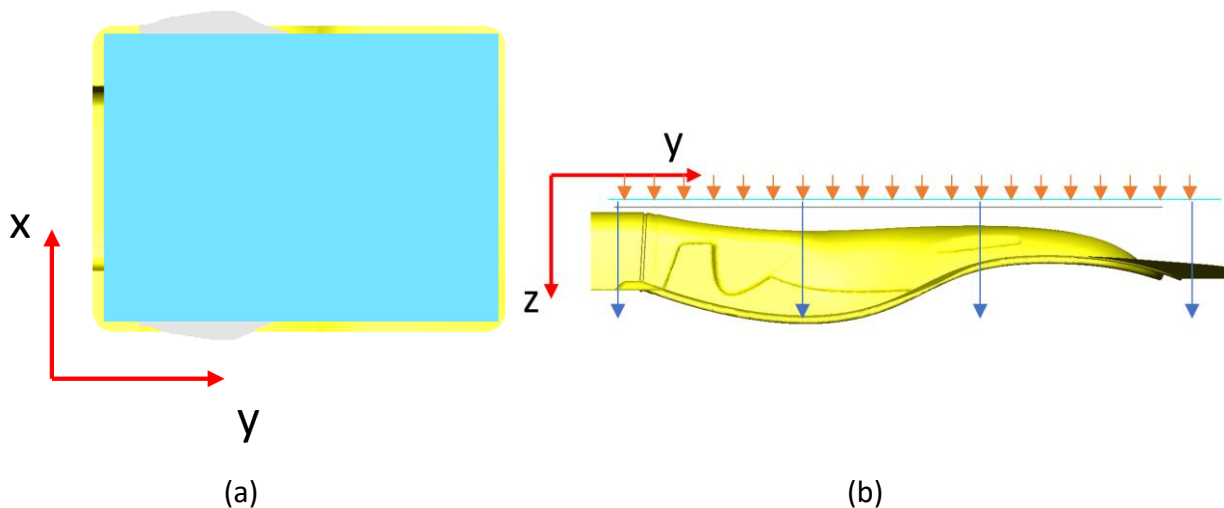
Figure 74 Membrane (in blue) over layers of fabrics (in grey) and male tool for membrane simulation (in yellow): top view (a) and side view (b) with boundary conditions: velocity (in blue arrow) and pressure (in orange arrows)

64
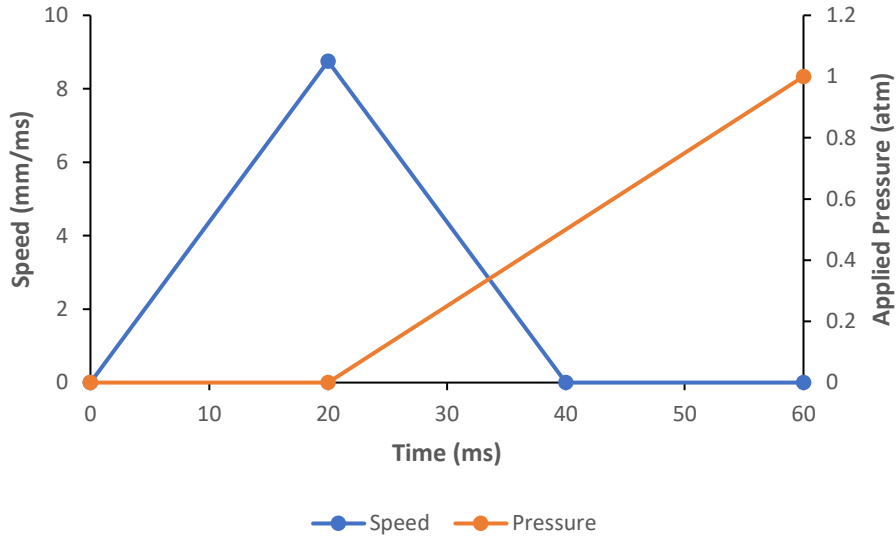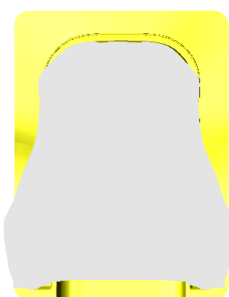
Figure 75 Boundary conditions applied for the membrane preforming simulation

Table 12 Progression of membrane preforming of TG15N

| Time (ms) | 0 | 20 | 40 | 60 |
|---|---|---|---|---|
| Description | Initial condition | Pressure starts to get applied | Membrane fully reaches its final displacement | Fully pressurised to atmospheric pressure |
| |  |  |  |  |

## 4.1.2    Matched-Tool Simulation Setup

The matched-tool simulation was created to evaluate other preforming methods for future usage. Despite its higher tooling cost, matched-tool preforming might be more adequate for industrial manufacturing purpose.

The fabric layers were placed between the rigid female punch-tool and the male tool (Figure 76). For the boundary conditions, the rigid female punch tool was displaced at an imposed velocity as reported Figure 77. The progression of TG15N matched-tool preforming is shown in Table 13.



(a)  (b)
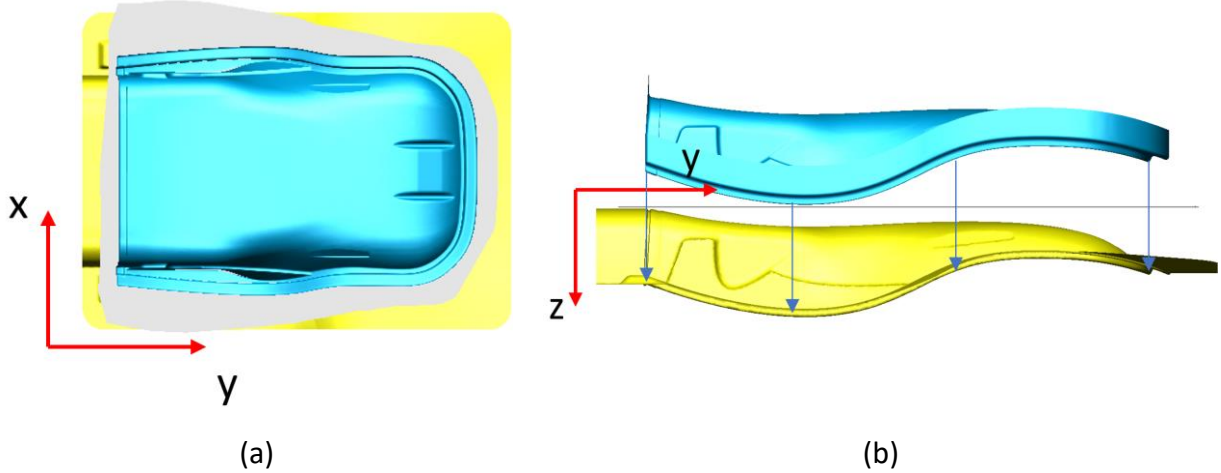
Figure 76 Female punch tool (in blue) over layers of fabrics (in grey) and male tool (in yellow) for matched-tool simulation: top view (a) and side view (b) with boundary condition: velocity (in blue arrow)
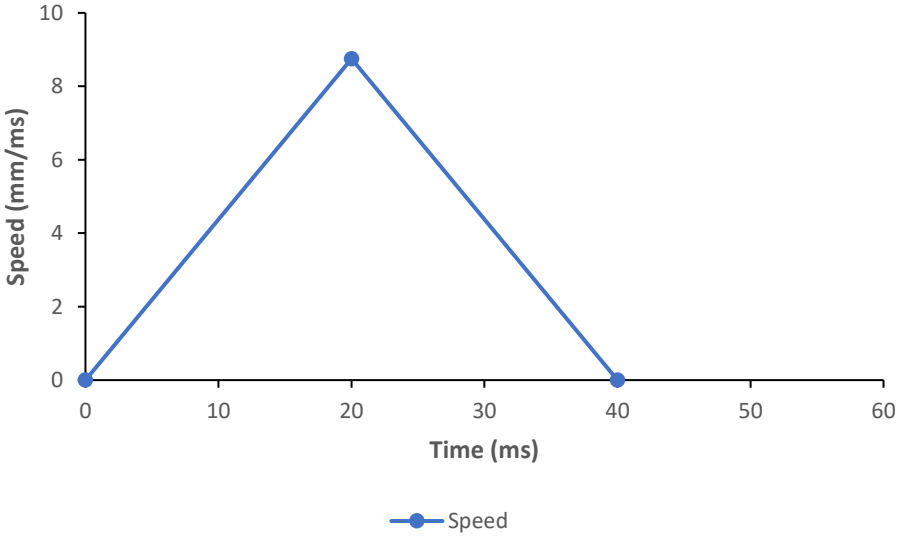


Figure 77 Boundary condition for the matched-tool simulation

Table 13 Progression of matched-tool preforming of TG15N

| Time (ms) | 0 | 20 | 40 |
|---|---|---|---|
| Description | Initial condition | | Final state |



## 4.2 Preforming simulation validation

### 4.2.1 Complex geometry preforming trials

The experimental preforming consisted in stacking 6 layers of TG15N fabrics with a binder applied between each ply to obtain a layup of [90/0/90]$_s$. The layers were cut using a 2D fabric cutting table from GERBERcutter® DCS 2500 (Figure 78). The layers stack was then laid on top of a preforming plug and formed under vacuum using a thick rubber membrane as shown in Figure 79. The system was then heated up at 100°C in an oven for 60 min to activate the binder.

A thermoplastic binder, EPIKOTE Resin TRAC 06720 (*HEXION* *TM)*, was used for the preforming experiments. It is a thermoset powder binder with softening temperature ranging from 90 to 100°C [61]. The binder behaves like a thermoplastic at its softening temperature, while temperatures above 100°C will initiate its cross-linking [61]. It has excellent compatibility with epoxy resin [61]. The final seatback preform is shown in Figure 80.

Figure 78 GERBERcutter® DCS 2500 Fabric cutting table at Centre Technologique en Aérospatiale (St-Hubert, QC)



Figure 79 Vacuum bagging for rubber membrane preforming
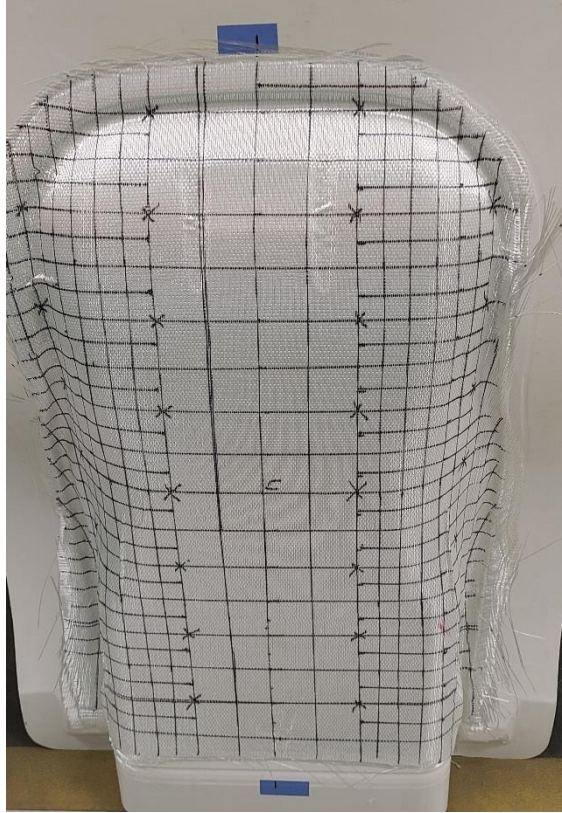
Figure 80 Final preformed seatback

## 4.2.2   Gridline validation methodology

The gridline validation methodology [37] was performed to compare the experimental and numerical shear angle results for the preforming of the seatback geometry.

First, a grid with 25 mm x 25 mm squares was drawn on the top layer (Figure 81-a). Then the experimental preforming process was carried as described in Section 4.2. The local shear angles of the top fabric were obtained by measuring the angles between the vertical and horizontal gridlines (Figure 81-b) using a protractor printed on a transparent plastic paper (Figure 82). Each corner was then coloured coded according to their shear angle (Table 14). This allowed to measure shear angles despite complex geometrical features. A total of 850 measured angles were compared with the computed shear angle results.
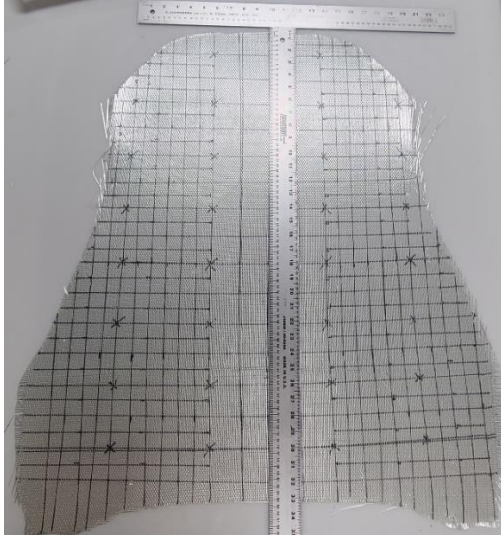
(a)                                                                              (b)

Figure 81 Initial gridlines on the TG15N fabric (a) and gridlines after preforming deformation (b)



(a)                                                                              (b)
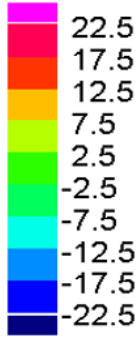


(c)                                                                              (d)

Figure 82 Various examples of the measurement of shear angle using gridline methodology on complex geometry with protractor printed on transparent paper (a to d)

Table 14 Shear angle legends for gridline validation methodology

| Comparison | Experiment and Simulation Shear Angle Distribution Legend (°) |
|---|---|
| Exp < Sim ⬭ (blue)<br>Exp > Sim ⬭ (red) | Shear angle<br>22.5<br>17.5<br>12.5<br>7.5<br>2.5<br>-2.5<br>-7.5<br>-12.5<br>-17.5<br>-22.5 |

Different regions (outside edge, within boundary, and hinge area) of the seatback geometry were analysed for the shear angle comparison as shown in Figure 83 and Figure 84. The withing boundary area corresponds to the actual component geometry, while the material outside the edge corresponds to the extra material required during the preforming step.
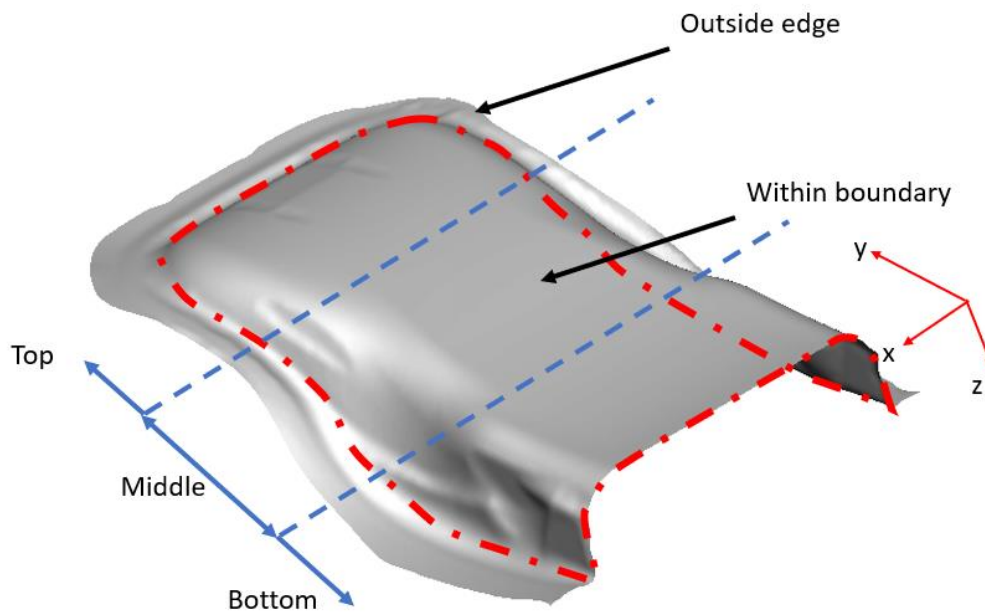


Figure 83 The boundary of the desired geometry (in red dashed line) and different sections used during analysis (in blue dashed line)

71
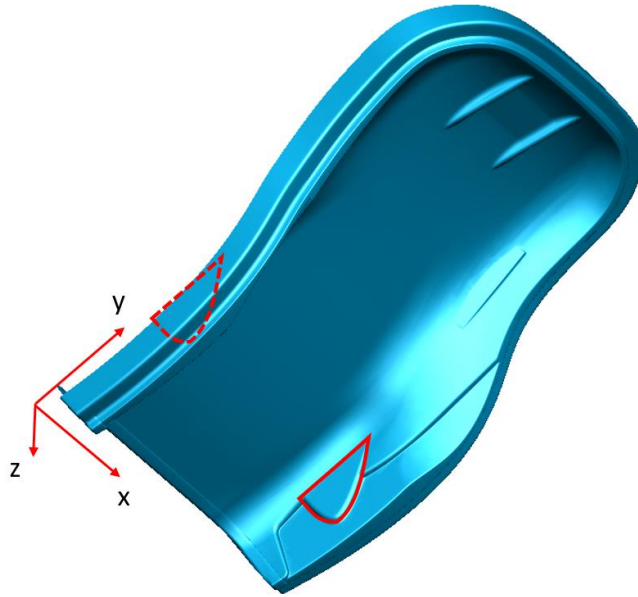
Figure 84 Position of hinge areas in red shown on the seat back mould geometry

Examples of the comparison between the experimental and simulation shear angles are shown in Figure 85 to Figure 89. In these comparisons, a red ellipse corresponds to a section where the simulation underpredicted the preform shear angles, while a blue ellipse corresponds to a section where the simulation overpredicted the preform shear angles.

The edge effects (difference at the outside of desired geometry boundary shown in Figure 83) are shown in several comparisons such as Figure 85, Figure 86, and Figure 87. In these areas, the simulation results are underestimating the shear angles.

On the contrary, at the hinge areas, the simulation is overestimating the shear angles. This is mainly due to a difference in part thickness between PAM-FORM model and the experimental preform. The simulation model was defined with a constant thickness of 2.5 mm. However, during the experimental part has a doubled thickness of 5 mm at the hinge area. This doubled thickness was not modelled in PAM-FORM.

(a)                                          (b)
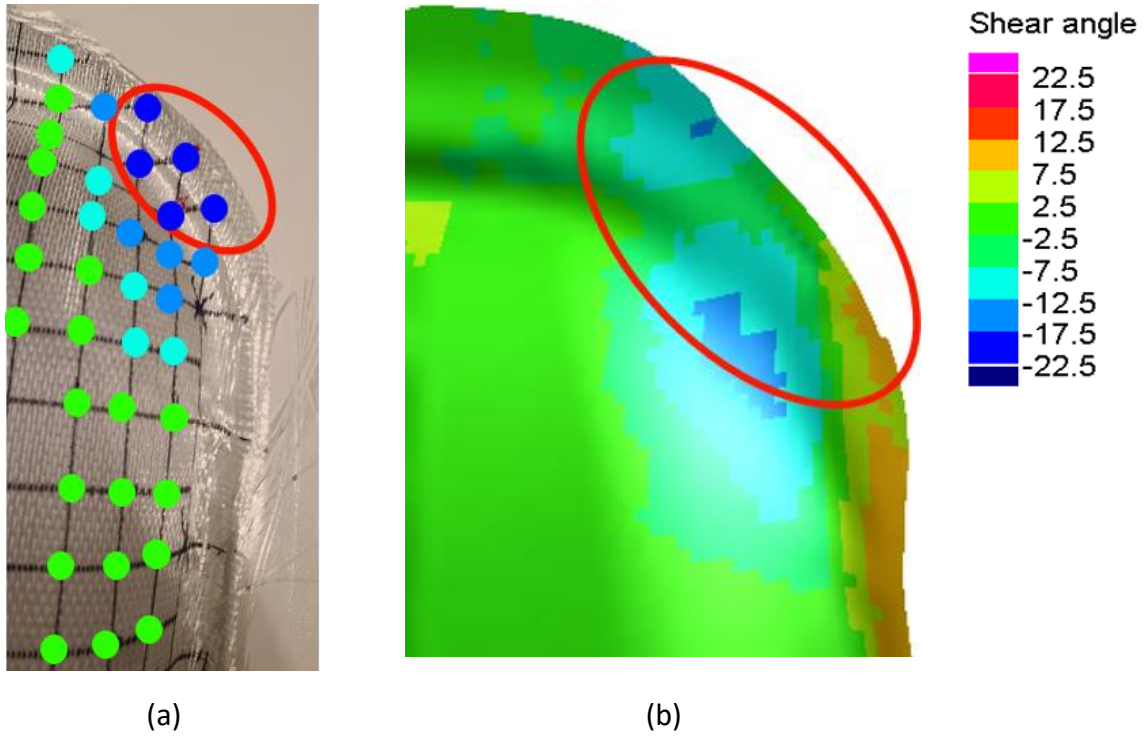
Figure 85 Shear angle comparison at the top right section for experimental (a) and simulation (b)

preforming



(a)                                          (b)
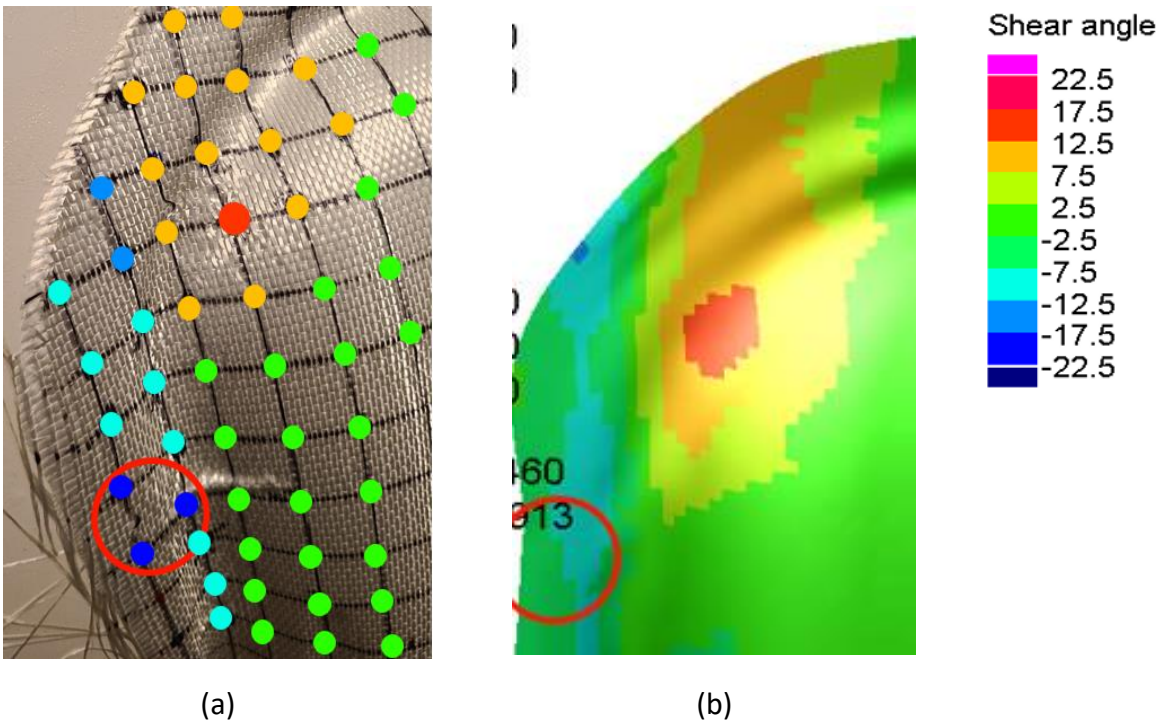
Figure 86 Shear angle comparison at the top left section for experimental (a) and simulation (b)
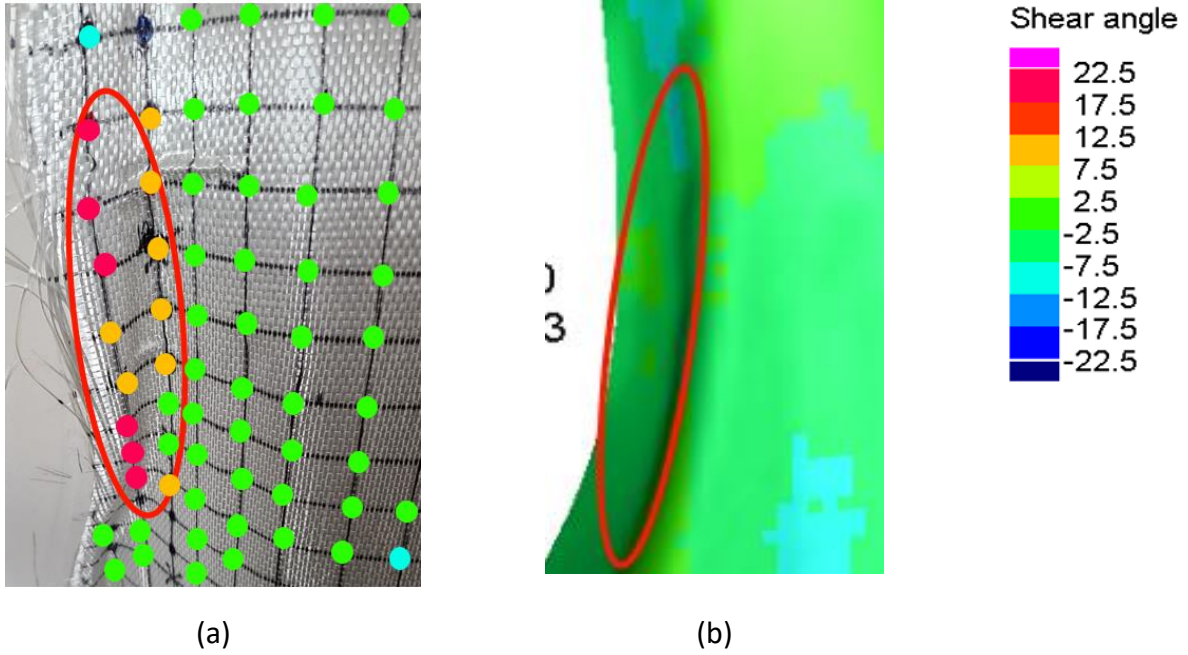
preforming

Figure 87 Shear angle comparison at the middle left section for experimental (a) and simulation (b) preforming
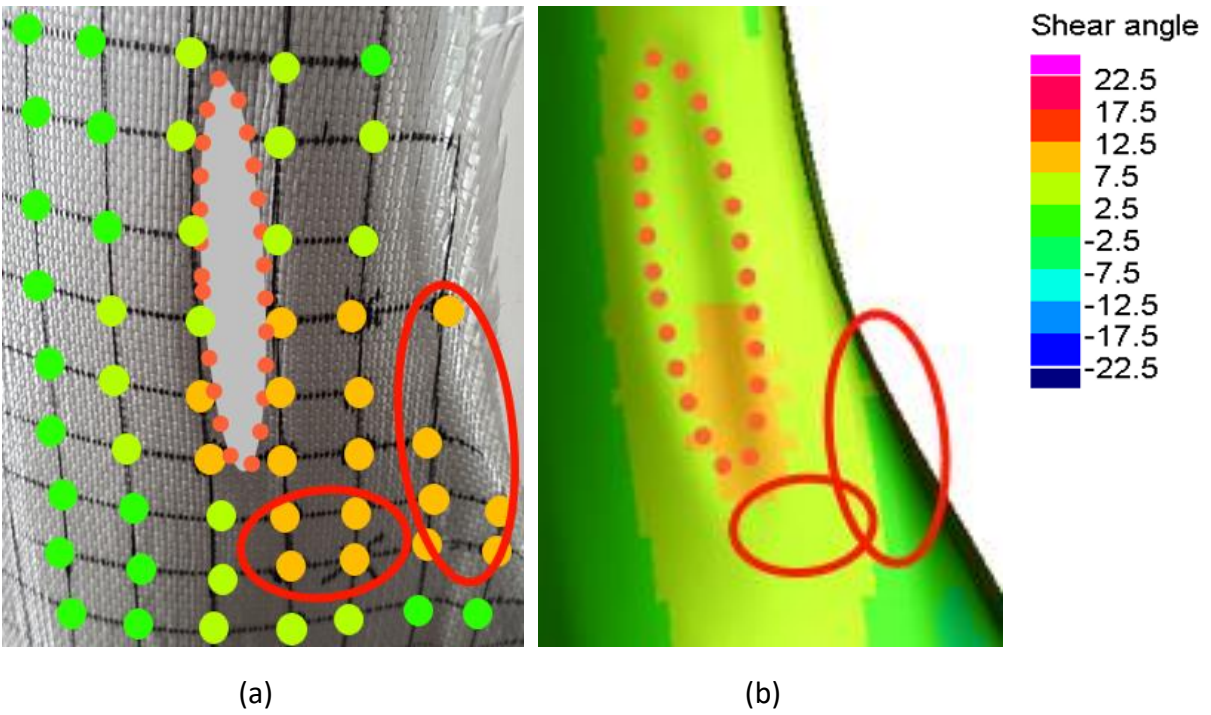


Figure 88 Shear angle comparison at the middle right section for experimental (a) and simulation (b) preforming with side ellipse area shown in orange pointed line
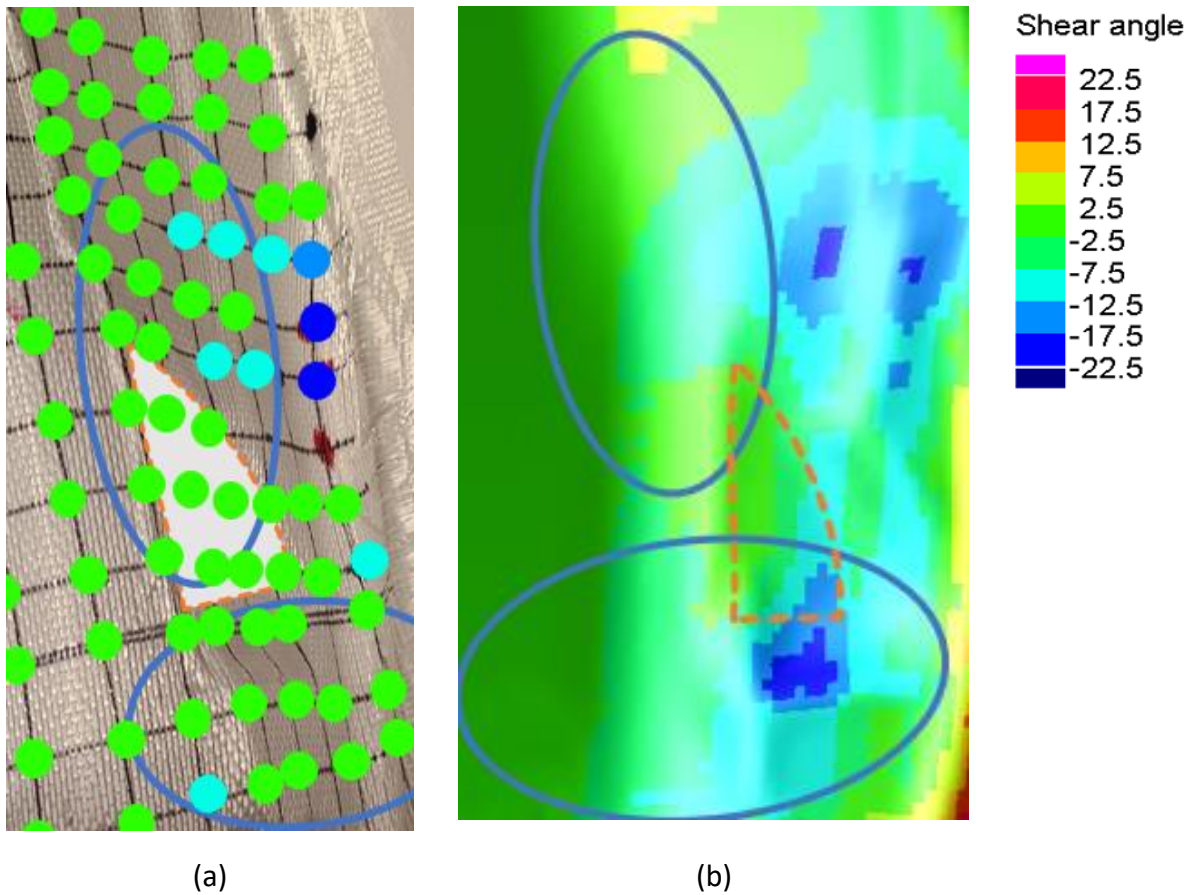
Figure 89 Shear angle comparison at the bottom right section for experimental (a) and simulation (b) preforming with hinge area shown in orange dashed line

The simulation was capable to simulate the shear angles within ±5° for 96% of the analysed corners. Most of the shear angles that had a difference superior to 10° were located at outside of the part boundary or near the hinge area. Within the boundary, only 10 corners were showing difference in shear angles greater than 5°. The simulation underestimated the shear angles at those regions. Some wrinkles were observed during experimental preforming. However, the membrane simulation was not able to predict any wrinkles. Further studies would be required to determine the reason behind the inaccuracy in prediction of wrinkle formation. First, a sensitivity analysis on bending modulus can be performed to determine if PAM-FORM can predict wrinkles for this geometry by reducing the bending modulus of the fabric. Then, the locations can be compared to experimental wrinkles. If the locations are similar to experimental wrinkle locations, bending characterisation test methodology must be improved.

Out of the 850 analysed corners, the count and proportion of errors at different locations are reported in Table 15. The error % reported in Table 15 is simply the proportion of the count of difference to 850 analysed corners.

Table 15 Count of difference in shear angle between experimental and simulation preforming of seat back using [90/0/90]s layup of TG15N

| Difference | ±5-7.5° | ±7.5-10° | >10° | Total | Error % |
|---|---|---|---|---|---|
| Outside edge | 0 | 2 | 8 | 10 | 1.18% |
| Within boundary | 1 | 7 | 2 | 10 | 1.18% |
| Hinge area | 0 | 10 | 5 | 15 | 1.76% |
| Total | 1 | 19 | 15 | 35 | |
| Error % | 0.12% | 2.24% | 1.76% | | 4.12% |

### 4.2.3  3D Scanning Methodology

The objective of the 3D scanning methodology was to compare the bridging level at critical regions (complex double curvature areas) to validate the bending behaviour of the characterised materials.

For this method, partial preforming processes were performed. The fabrics were deformed under vacuum using rubber membrane at room temperature without binders. The Hexion Absolut Arm-7 Axis 8525-7 3D scanning device was used as shown in Figure 90. The accuracy (maximum permissible longitudinal error $E_{UNI}$) of the scanner was 0.047 mm according to ISO 10360-12:2016. Two experimental scanning were performed:

- without any fabrics
- with eight plies in the warp direction (0 deg) of TG15N

The first experimental scanning (without any fabric) allows to validate the deformation of the membrane with its characterised properties from Section 4.1.1.
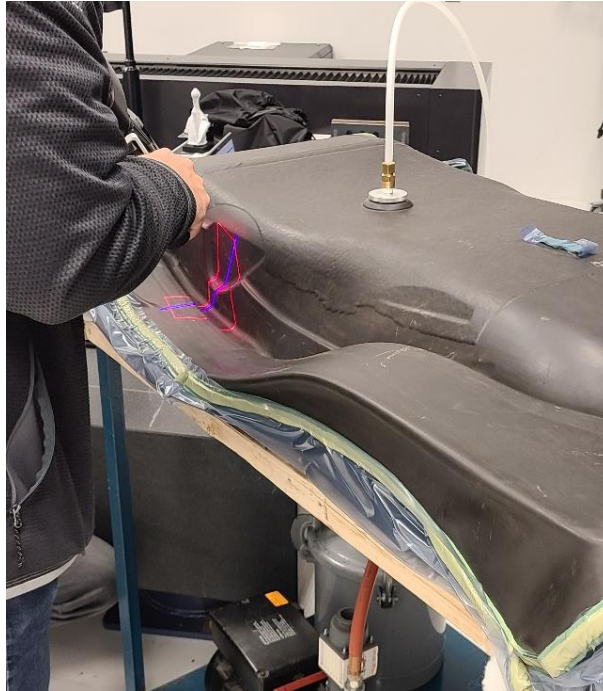
Figure 90 3D scanning process using Hexion 8525-7 performed at the Centre Technologique en Aérospatiale (CTA) (St-Hubert, QC)

The comparison between the simulation and the scan geometry was performed by using the Autodesk Inventor CAD software. The geometry from the simulation was exported from PAM-FORM using IGS format and the scanned file was exported from Polyworks software using STL format. Both geometries were matched by using different flat reference surfaces, the bridging levels were then compared at different cross-sections.

The following figures (Figure 91 and Figure 92) illustrate the comparisons between the experimental 3D scanned preformed and simulated preformed membrane with no fabric and with 8 layers of TG15N, respectively. The black colour with the orange dashed outline represents experimental 3D scanned membrane geometry, and the grey colour with the blue dashed outline represents the simulated membrane geometry.

As shown in Figure 91, the simulation predicted a much stiffer membrane material compared to the experiment with some bridging at the deep groove around the geometry (Figure 72). During the experimental preforming, the membrane was capable to deform fully into the groove, while the simulation is showing some bridging of the membrane. The tensile property of membrane, only required material input in PAM-FORM, may not be sufficient to predict the complete

behaviour of the membrane during experimental preforming. Despite inaccurate prediction of the rubber membrane without fabrics, good correlation of the membrane's shape was observed between the experiment and the simulation for the validation with 8 layers of TG15N NCF (Figure 92). It might be assumed that, as the membrane properties is much lower than the fabrics properties, the simulation was driven by the fabric properties of TG15N.
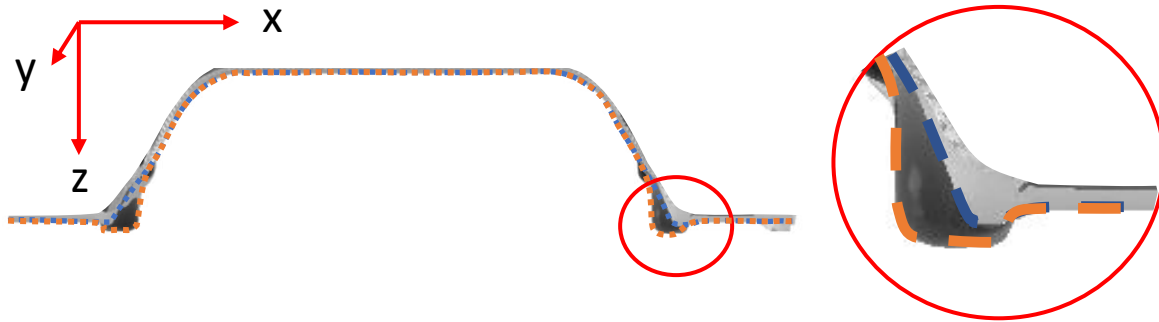


Figure 91 Cross-section comparison between experimental 3D scanned membrane (in orange dashed line) and simulation preforming membrane (in blue dashed line) for no fabric setup
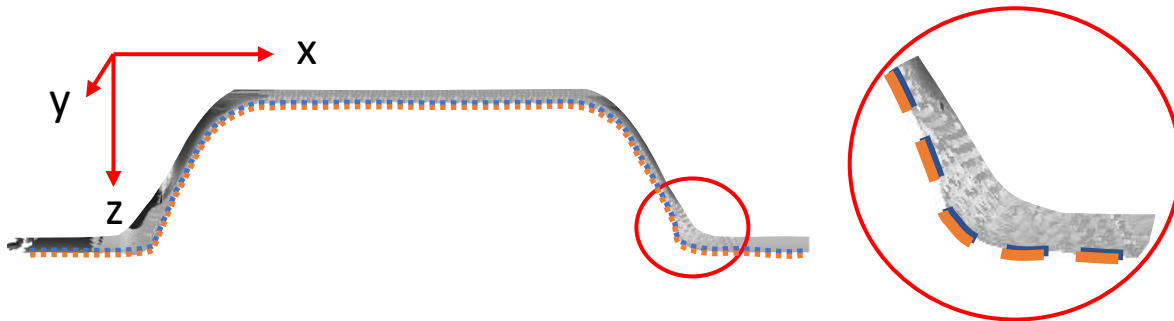


Figure 92 Cross-section comparison between experimental 3D scanned membrane (in orange dashed line) and simulation preforming membrane (in blue dashed line) for TG15N setup

Other characterisation tests of the drapability behaviour of the membrane could improve the accuracy of prediction of the final shape of the rubber membrane under vacuum.

## 4.3    Tensile Properties Sensitivity Analysis

The tensile properties of the NCF were not experimentally characterised. However, to determine the effect of the fabric tensile properties on NCF preforming behaviour, a sensitivity analysis on the tensile properties was performed using the matched-tool and membrane preforming

simulations. Sensitivity analysis was performed with tensile modulus set at 35 GPa, 50 GPa 70 GPa, and 100 GPa. From the literature a typical tensile modulus of E-glass fibre is 70 GPa [60].

For the matched-tool simulation, no significant differences between results with different tensile moduli were found for the shear angle results (Figure 93 and Figure 94) except at the outside of the part boundary. Within the boundary of the seatback, the shear angle contour looked very similar for all tested fabric tensile modulus. Difference in maximum and minimum shear angles were observed in the outside region of the boundary but no specific trend was observed as shown in Figure 95. The matched-tool preforming simulations did not predict any bridging (Figure 96). So overall, the fabric tensile modulus did not affect the matched-tool preforming simulation.
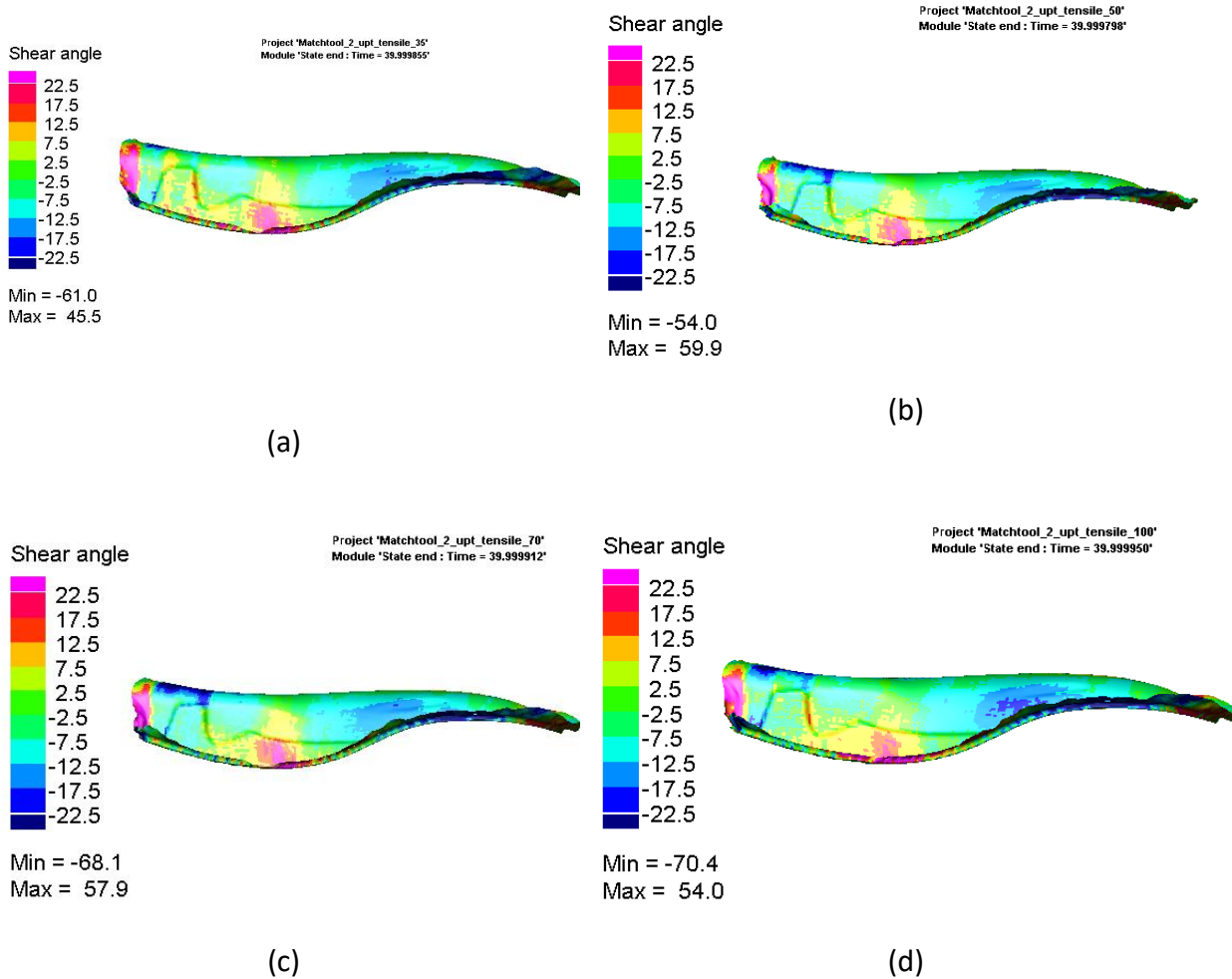


Figure 93 Side view comparison of shear angle for different fabric tensile modulus for the matched-tool simulation: 35 GPa (a), 50 GPa (b), 70 GPa (c), and 100 GPa (d)
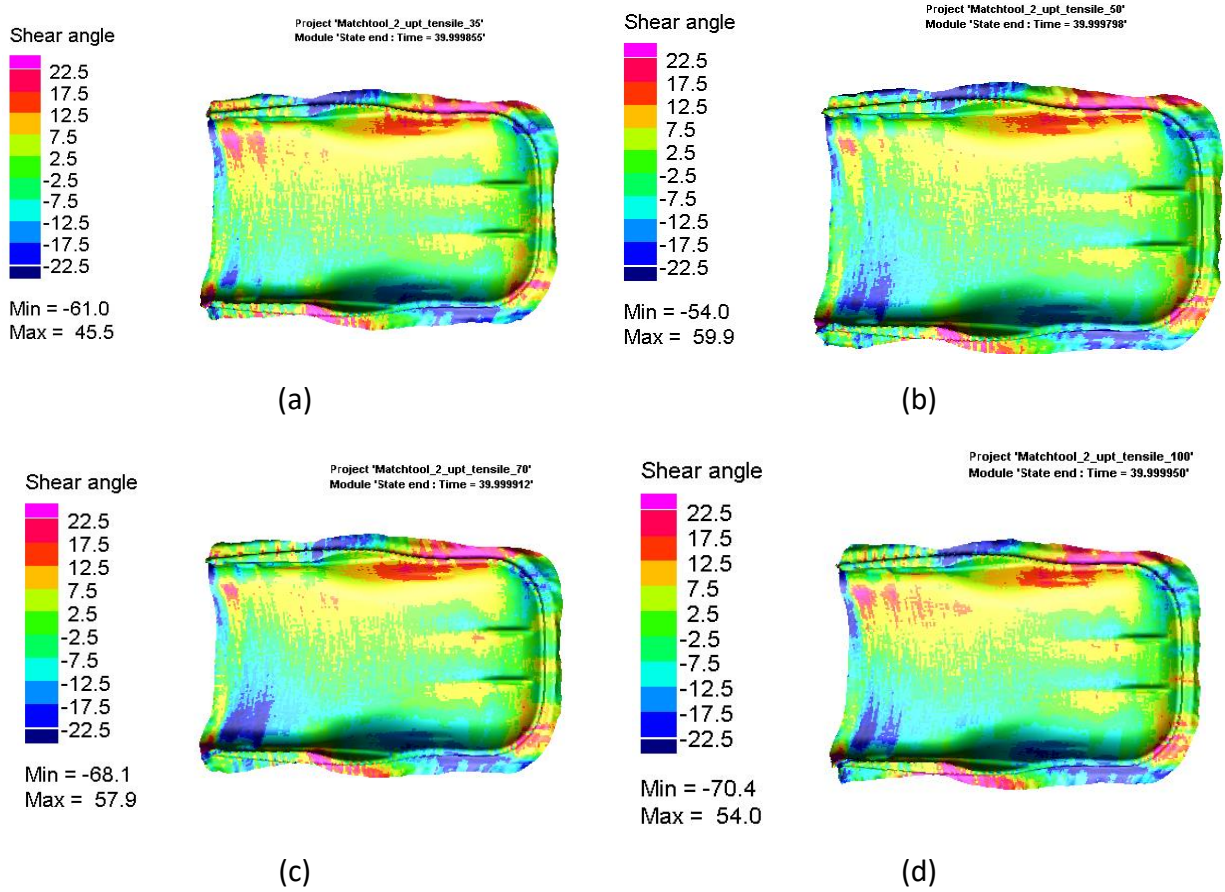
Figure 94 Top view comparison of shear angle for different fabric tensile modulus for the matched-tool simulation: 35 GPa (a), 50 GPa (b), 70 GPa (c), and 100 GPa (d)
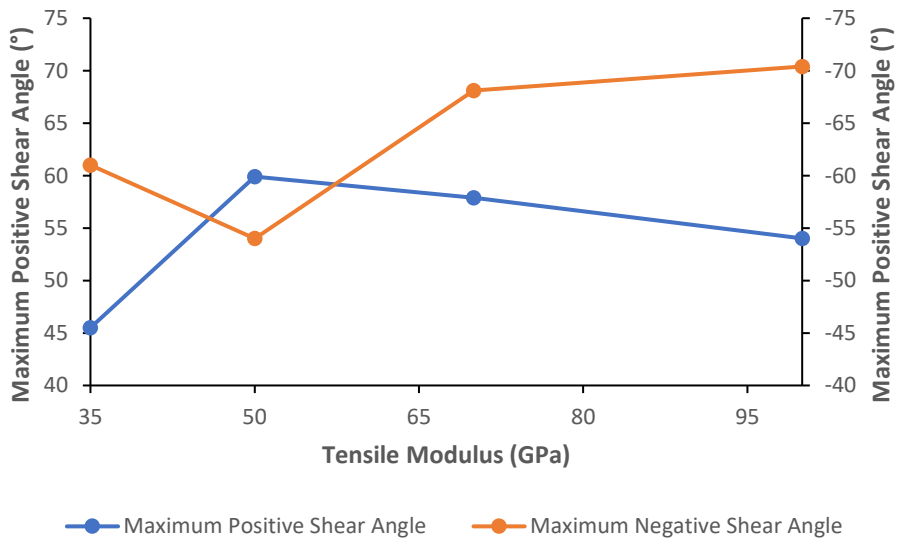


Figure 95 Variation of the maximum positive and negative shear angles as a function of the fabric tensile modulus for the matched-tool simulation
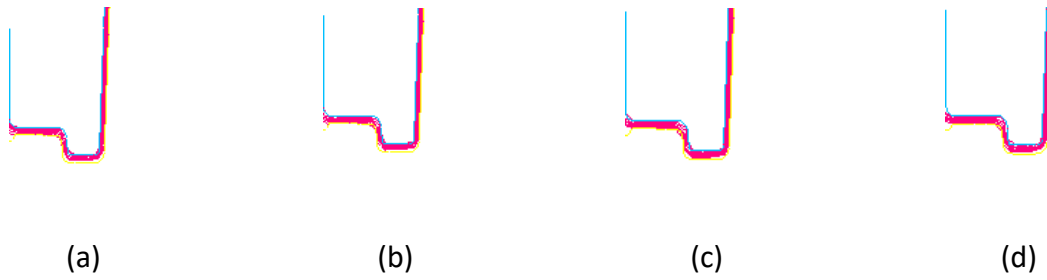
Figure 96 Cross-section view at the deepest groove section comparison of bridging for different fabric tensile modulus for the matched-tool simulation: 35GPa (a), 50 GPa (b), 70 GPa (c), and 100 GPa (d)

Similarly to the matched-tool simulation, the membrane simulation results showed no significant effect of the fabric tensile modulus on preform shear angles, as shown Figure 97, Figure 98 and Figure 99.

However, an effect on bridging was observed as shown in Figure 100 where the distance between the membrane and the tool for each fabric modulus is presented. Bridging increased with the tensile modulus of the fabric. A difference of 1.5 mm in bridging was observed between a tensile modulus of 35 GPa and 100 GPa.
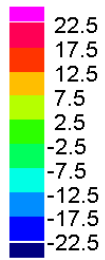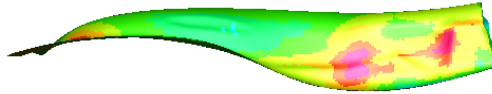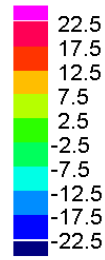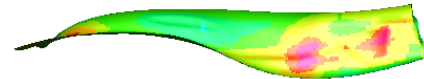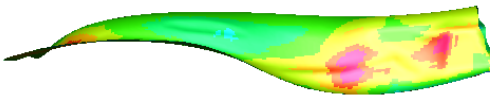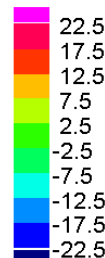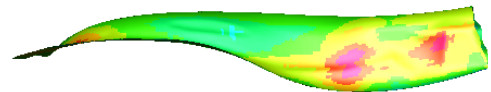
Figure 97 Side view comparison of shear angle for different fabric tensile modulus for the membrane simulation: 35GPa (a), 50 GPa (b), 70 GPa (c), and 100 GPa (d)
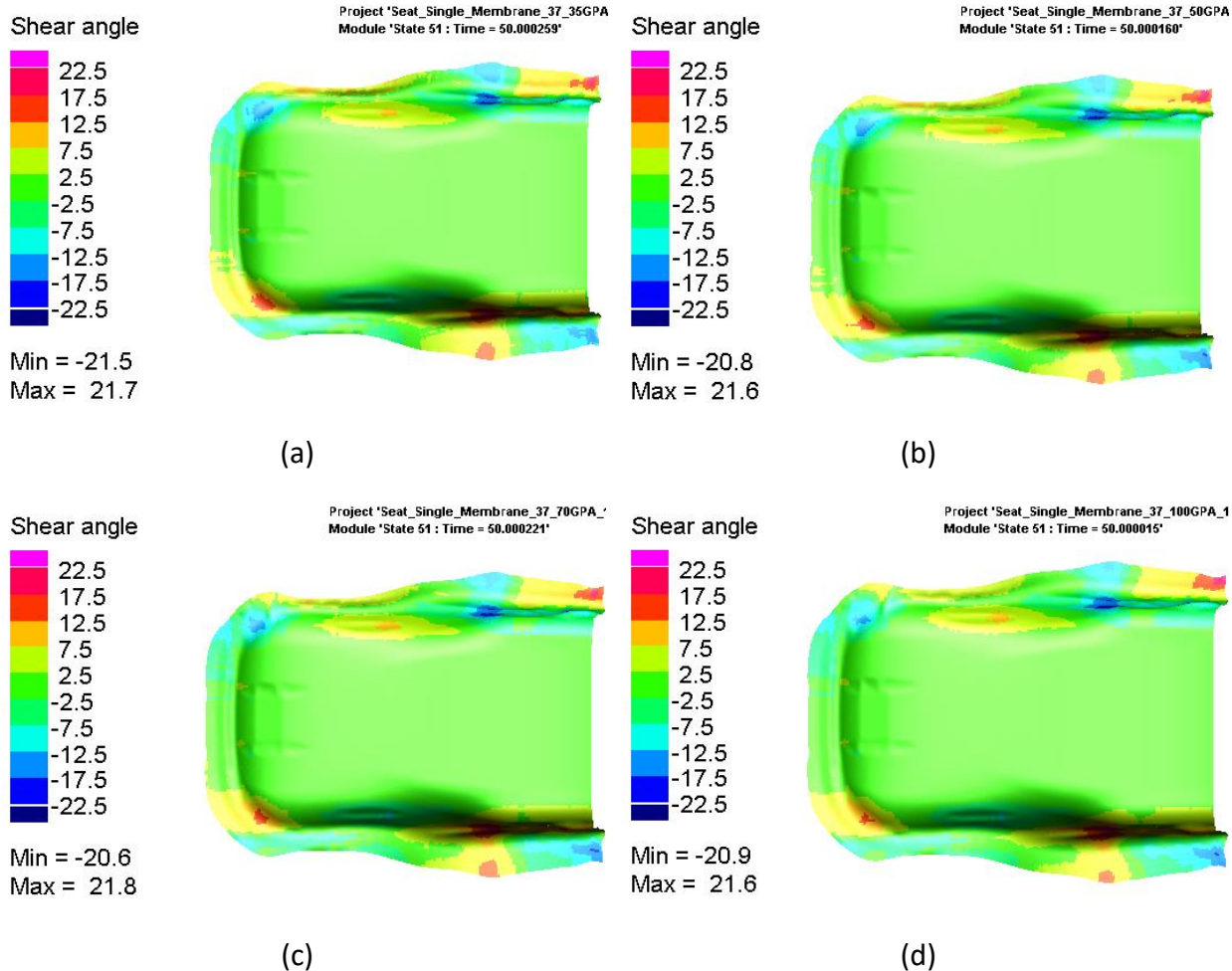
Figure 98 Top view comparison of shear angle for different fabric tensile modulus for the membrane simulation: 35GPa (a), 50 GPa (b), 70 GPa (c), and 100 GPa (d)
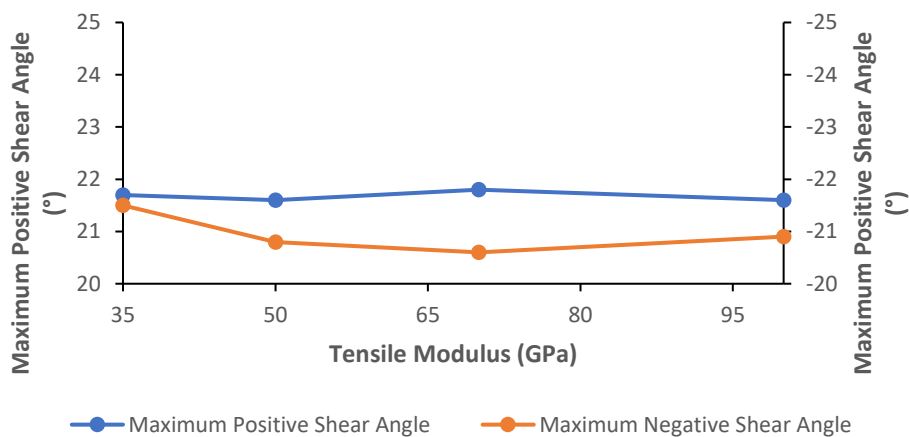


Figure 99 Variation of the maximum positive and negative shear angles as a function of the fabric tensile modulus for the membrane simulation

83
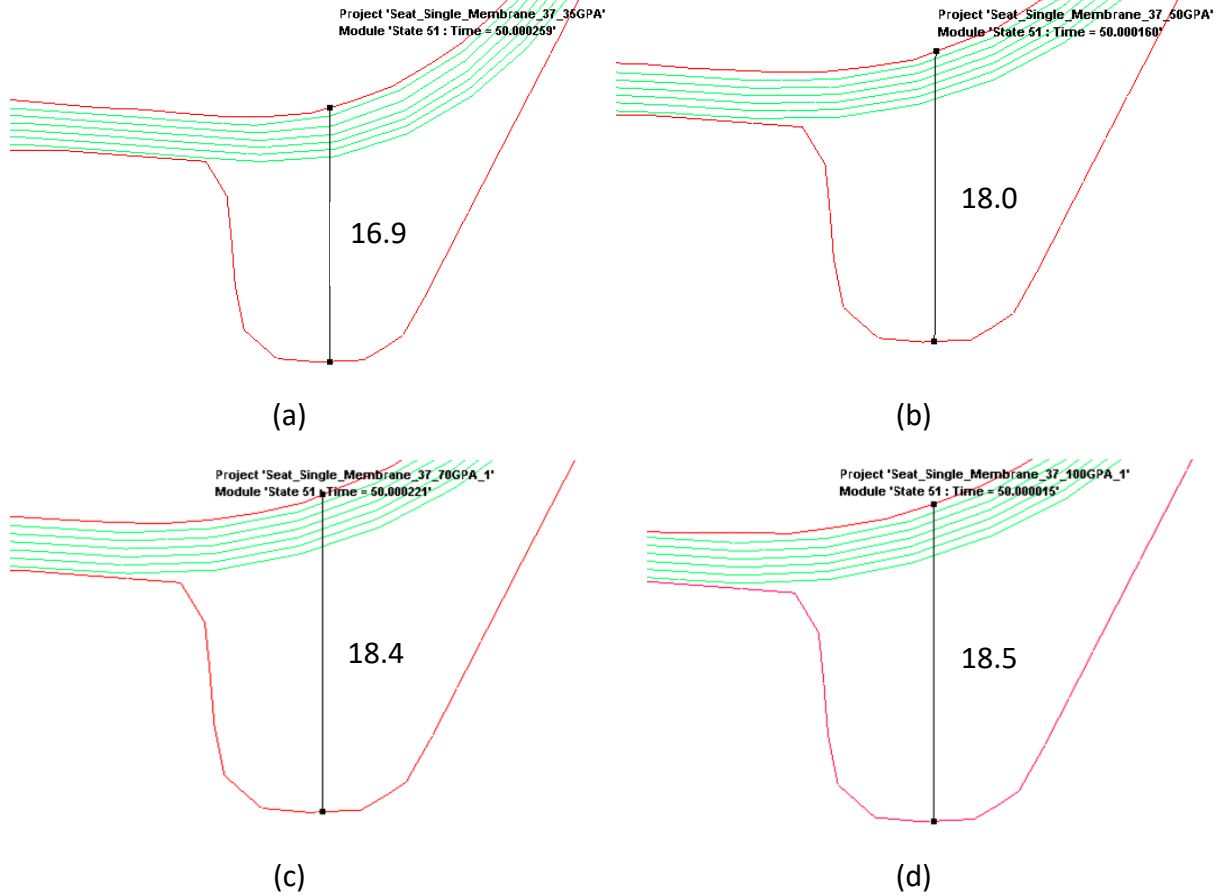
Figure 100 Cross-section view at the deepest groove section comparison of bridging for different fabric tensile modulus for the membrane simulation: 35GPa (a), 50 GPa (b), 70 GPa (c), and 100 GPa (d) with distances between tool and membrane shown in mm

Considering the sensitivity analyses of the tensile properties of fabrics for both matched-tool and membrane simulations, for the seatback geometry, it can be concluded that the tensile properties did not affect the shear angle results. Also, the variation of the tensile properties did not significantly affect the bridging level of the membrane and matched-tool simulations.

## 4.4  Flat Pattern Optimisation

Flat-pattern optimisation is a useful tool to reduce labour by determining the fabric cutting shape to obtain the desired deformed shape after preforming [31]. Optimised flat pattern helps improving the preform quality, especially near the edge of the part.

Flat pattern optimisation was performed by using the flattening curve tool in PAM-FORM. Given the boundary curve of the desired final shape, PAM-FORM is capable to extract that curve to the

fibre meshes orthogonally or into X, Y and Z directions. In this case, the final shape curve was extracted in the Z direction.

For this type of optimisation, several iterations were required (Figure 101). In this picture the flat pattern is shown in grey, while to tool is shown in blue. The first preforming simulation was performed using a rectangular shape (Figure 101-a). Using the results, three other iterations were performed (Figure 101 – b, c, d).



(a)

(b)

(c)

(d)
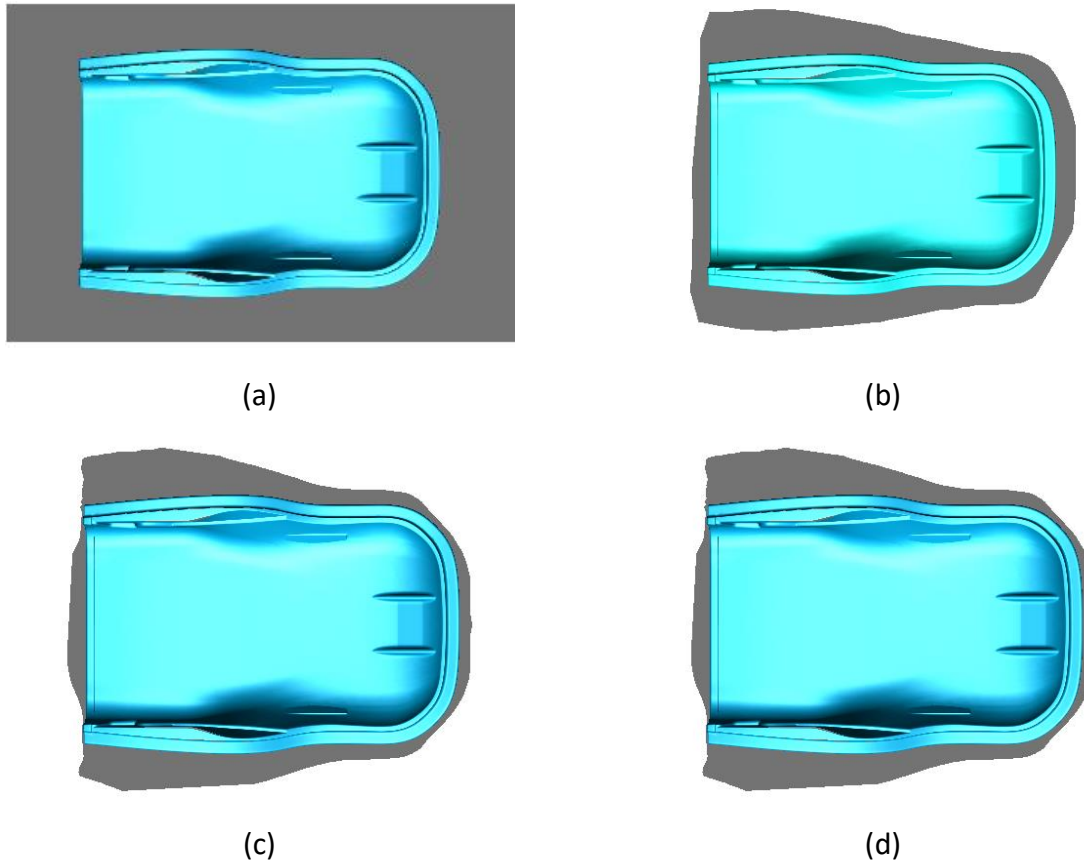
Figure 101 Progression of flat pattern optimisation iterations (in grey) 1 to 4 (a to d) and female punch tool (in blue) as reference

Shear angles were then compared between the four iterations (Figure 102 and Figure 103). Significant reduction in maximum shear angles were observed from the initial rectangular fabric shape as shown in Figure 104. The maximum and minimum shear angles converged at the fourth iteration. Comparing in terms of shear angle distribution, the optimised shape resulted in lower shear angles in the inside boundary.

**Shear angle**

| | |
|---|---|
| 22.5 | |
| 17.5 | |
| 12.5 | |
| 7.5 | |
| 2.5 | |
| -2.5 | |
| -7.5 | |
| -12.5 | |
| -17.5 | |
| -22.5 | |

Project 'Matchtool_2_upt_tensile_70_Rectangle'
Module 'State end : Time = 39.999943'

Min = -52.0
Max = 71.4

(a)

Project 'Matchtool_2_upt_tensile_70'
Module 'State end : Time = 39.999912'

Min = -68.1
Max = 57.9

(b)

Project 'Matchtool_2_upt_tensile_70_OP1_2'
Module 'State end : Time = 39.999863'

Min = -45.8
Max = 42.7

(c)

Project 'Matchtool_2_upt_tensile_70_OP1_22'
Module 'State end : Time = 39.999863'

Min = -45.8
Max = 42.7

(d)

Figure 102 Side view comparison of shear angle for four different flat pattern optimisations 1 to 4 (a to d)
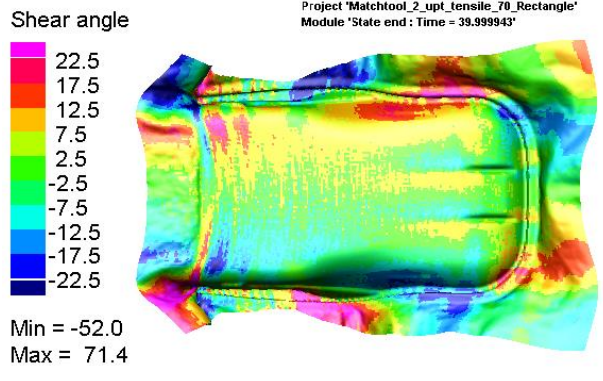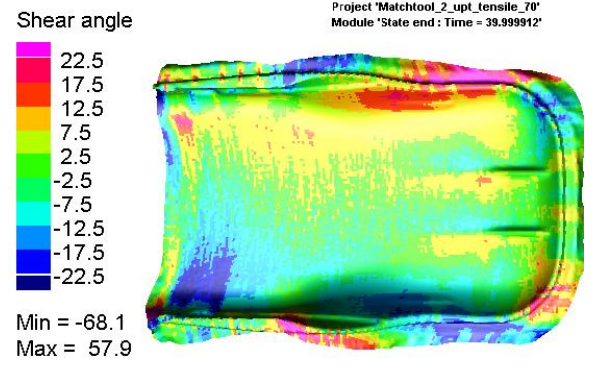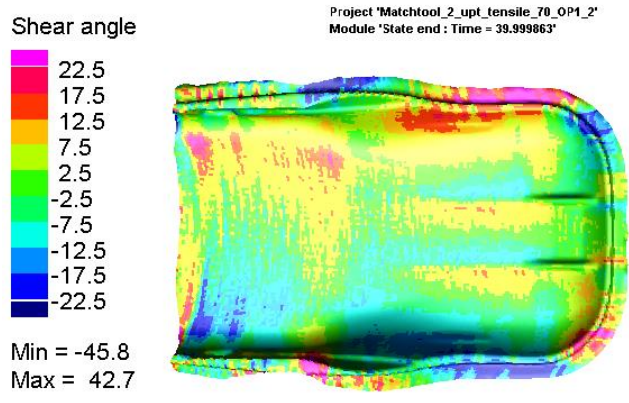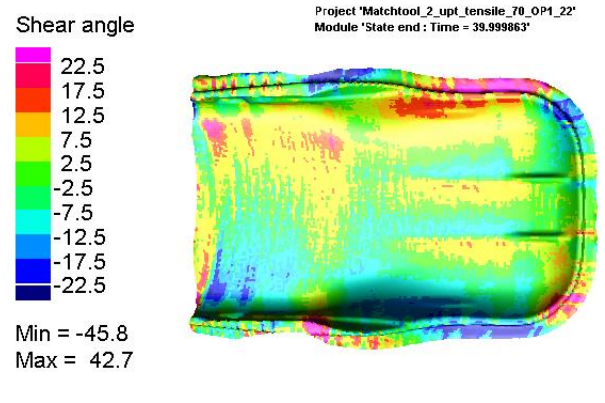
Figure 103 Top view comparison of shear angle for four different flat pattern optimisations 1 to 4 (a to d)
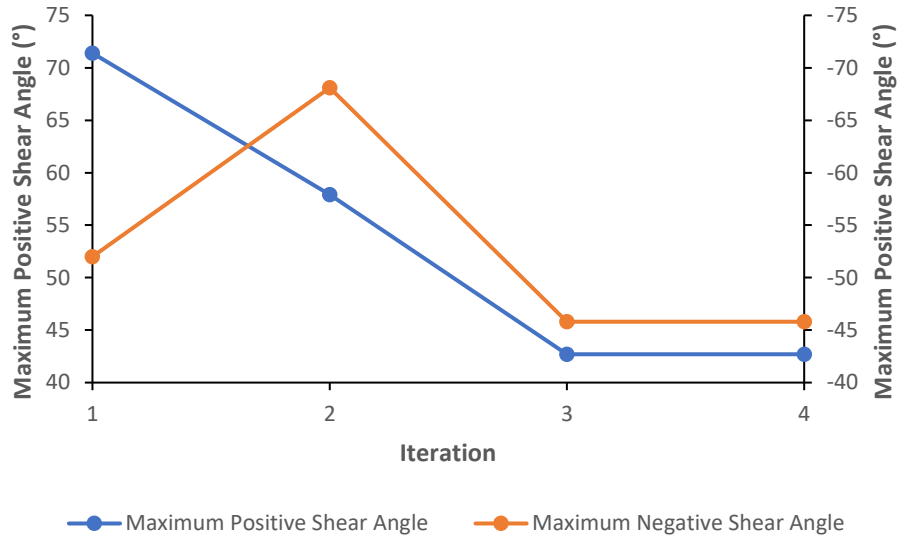
Figure 104 Comparison of maximum positive and negative shear angles for four different iterations of flat pattern optimisation for the simulation

Flat pattern optimisation results were compared with flat pattern obtained using kinematic mapping simulation (FiberSim software) in Figure 105. Kinematic mapping may seem more suitable for this purpose as it can be done in a single iteration. The Composites and Advanced Materials team of CTA performed the flat pattern optimisation on FiberSim. The material behaviour input required for the FiberSim is only the locking angle of the fabric. The locking angle of 54° was used for TG15N material. Visually, the two patterns showed different shapes. The flat pattern of PAM-FORM is longer at the lower edge and wider at the side edges.



(a)                                                        (b)

Figure 105 Comparison between optimised flat patterns from FiberSim (a) and PAM-FORM (b)

The shear angle distributions of the flat patterns obtained with the two softwares were compared in Figure 106 and Figure 107. The maximum shear angles are much higher with the FiberSim simulation output. Also, within the boundary of the seatback, the shear angle distribution shows much higher shear angles with the FiberSim flat pattern. Moreover, FiberSim flat pattern led to incomplete component geometry as shown in red dash-line in Figure 107-a.



(a)                                                        (b)
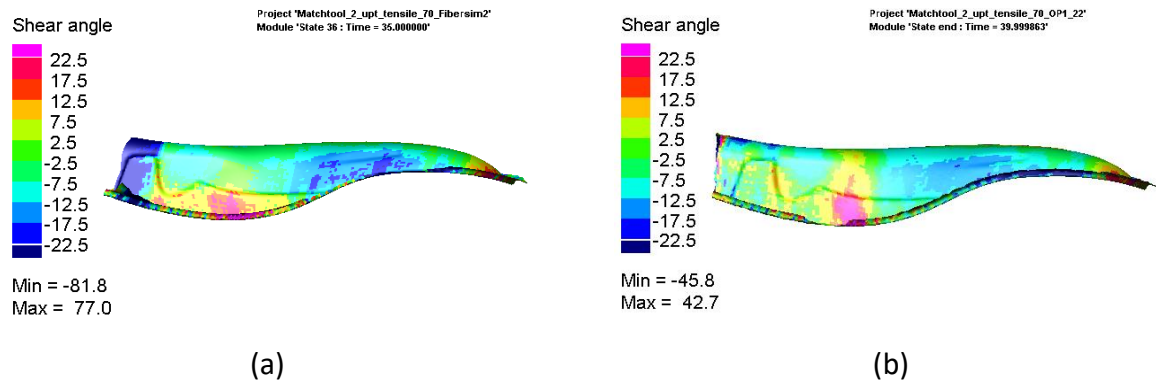
Figure 106 Side view comparison of shear angle for optimised flat pattern from FiberSim (a) and PAM-FORM (b)



(a)                                                        (b)
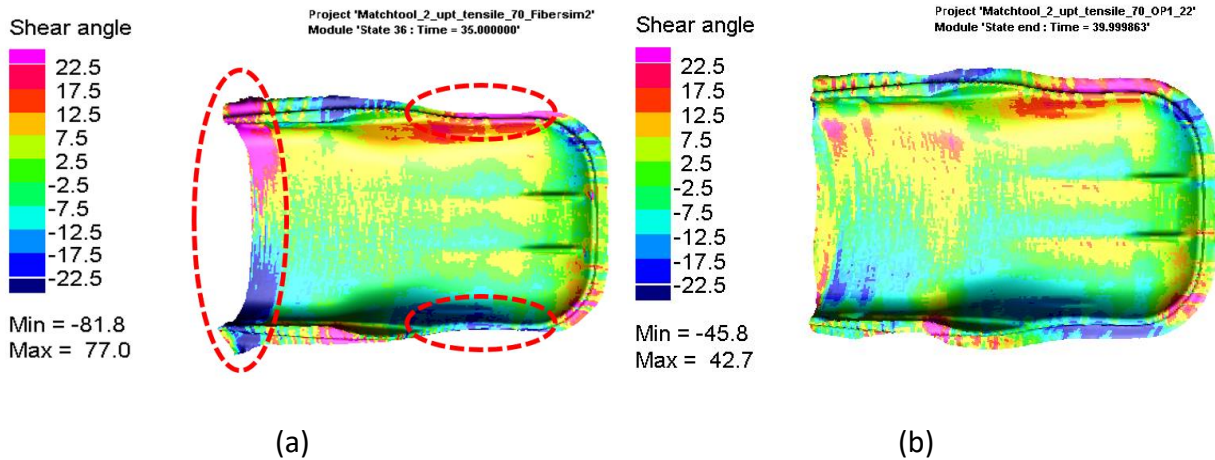
Figure 107 Top view comparison of shear angle for optimised flat pattern from FiberSim (a) and PAM-FORM (b) with inaccurate geometry shown in red dashed line

## 4.5   Discussion

By implementing the characterised shear and bending behaviours of the NCF, PAM-FORM was able to predict the shear angles of experimental preforming within ±5° for 96% of analysed 850 corners. Also, PAM-FORM was able to predict the bridging level of the membrane under vacuum. From the validation results of shear angle and bridging, the matched-tool preforming setup was simulated. The matched-tool (Figure 93-c and Figure 94-c) resulted in much higher shear angles

compared to membrane preforming (Figure 97-c and Figure 98-c). These higher shear angles may result in lower permeability of the preform and lower strength of the final composite part. However, the membrane preforming results in bridging of 18.4mm (see Figure 100-c) which was also shown during 3D scan of the experimental preforming (see Figure 92). The bridging may be then eliminated during the compression step of the CRTM process. Considering the cost of the matched-tool preforming and its high shear angles, membrane preforming would be favored over the matched-tool preforming.

Additional PAM-FORM simulations could be carried out to improve the existent preforming processes by trying different preforming variables (i.e. punch displacement time, vacuum pressure). Also, other preforming techniques can be tried such as the sequential stamping and pressurised membrane shown in Figure 108.
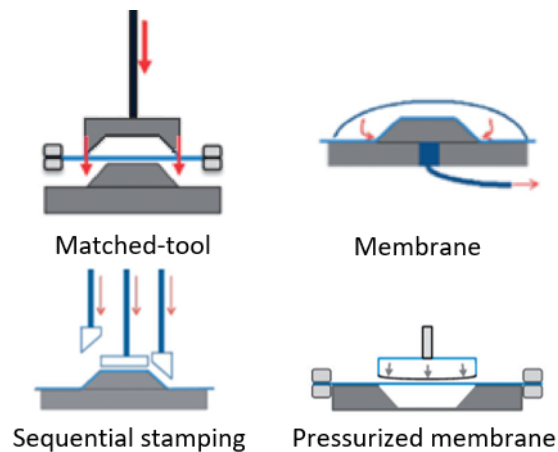


Figure 108 Examples of basic forming processes (reproduced with permission from P. Middendorf [7])

From the sensitivity analysis of tensile properties, no effect in both shear angle distribution and bridging level for the matched-tool simulations were predicted with the seatback geometry. For the membrane simulation, varying the tensile properties did not affect the shear angle distribution. Only a small effect was observed for the bridging level. The fabric tensile properties sensitivity analysis shows that the fabric tensile properties do not have to be characterised in order to obtain accurate preforming simulation. As shown from the literature, the effect of the tensile properties may be more important if there is a blank holder in the preforming setup.

The flat pattern optimisation clearly improves the part quality when comparing the maximum and minimum shear angles. After four iterations, the simulation predicted significant decrease in maximum and minimum shear angles. The results of flat pattern obtained from FiberSim and PAM-FORM were compared. PAM-FORM's flat pattern resulted in better geometry and lower shear angle distribution. The inaccuracy of the FiberSim software may be due to the non-consideration of the entire drapability properties other than the locking angle of the material. However, the FiberSim flat pattern was obtained within few minutes, while PAM-FORM's flat pattern was obtained within several iterations (about three days).

# 5 Conclusion

In this study, the shear and bending properties of NCF (TG15N, TG33N, and SG33N) reinforcements were characterised and implemented in PAM-FORM preforming software. NCF material data cards were validated by modelling the shear and bending characterisation tests and comparing experimental and numerical results. Good correlations were obtained for both shear and bending behaviours with average $R^2$ values of 0.986 for shear and 0.962 for bending. From those characterisation tests, TG15N seems to have the best drapability properties in shear with a high shear locking angle (54.4°). TG15N is also less susceptible to have bridging. However, it might be more prone to wrinkles during preforming compared to the other two materials because of its low flexural rigidity (1.29 $\times 10^{-3}$ N·m in warp and 1.60 $\times 10^{-3}$ N·m in weft). This material would be suitable for preforming of complex geometry which has high curvature and complex features. SG33N also has a high locking angle and relatively low flexural rigidity in the warp direction (2.17 $\times 10^{-3}$ N·m). By placing the fabric such that the warp direction is in parallel to curvature's tangential direction, this material could also be a great option for preforming complex geometry. The thermoplastic binder integrated in its architecture could be directly used as fabric binder to simplify the preforming process. SG33N and TG33N are thicker than TG15N. This characteristic is very important as it leads to decrease the number of plies required for the laminate and therefore reduce the manufacturing time with a reduction of the binder application processes.

The complex geometry preforming simulations were developed to determine the capability of PAM-FORM software to simulate NCF materials for complex 3D geometry preforming. The gridline and 3D scanning methodologies were used to validate the complex geometry simulations by measuring the preform shear angle and bridging. Good correlations were found for both methodologies. However, PAM-FORM simulation software was not able to properly predict wrinkling effects. The tensile properties sensitivity analysis was used to see effect of tensile properties on preforming. Results showed that the value taken from the literature was sufficient to obtain accurate preforming simulations. A flat pattern optimisation was also performed with PAM-FORM and FiberSim and demonstrated that flat pattern optimisation improves the part quality. Taking into consideration the material properties of the fabric is necessary to obtain a

more accurate flat pattern, but the kinematic mapping simulation (FiberSim) could still be a useful tool to have the initial starting shape for the optimisation, as it is much quicker to obtain the results. The results between membrane and matched-tool preforming were also compared and showed that the membrane preforming resulted in lower shear angle distribution but bridging of the preform in the groove feature around the preform perimeter. The effect of bridging was then found to be negligible during the experimental compression-RTM manufacturing process.

## 5.1   Future Work

As future work, the further optimisation for the preforming of the current seatback complex geometry could be performed by using the developed and validated material data cards:

- Simulating different techniques of preforming processes could also be carried out. Some examples of other possible techniques are sequential preforming and pressurised membrane preforming as shown in Figure 108.

- Experimental validation of match-tool preforming could be performed as several studies were performed on this preforming methodology.

- Experimental validation of the difference between optimised flat patterns from both PAM-FORM and Fibersim could be performed.

- Other dry fabrics with different weave architecture could be characterised and implemented by following the characterisation and implementation methodologies described in this study.

- Prepreg materials could also be characterised using similar characterisation methodologies. For prepreg materials, temperature must be considered as prepreg exhibits a shear rate-dependent behaviour due to resin viscosity.

- Other complex geometries could be simulated using the complex geometry simulation modelling processes using the characterised material data cards (TG15N, SG33N, and TG33N).

- Further characterisation of the rubber membrane materials (i.e., bending) could be performed to improve the accuracy of the effect of the membrane on the preforming.

- Other dry fabric drapability behaviour characterisation methodologies could be performed and be compared with the results of this study. Few examples of different characterisation methodologies are:
  - In-plane shear: bias-extension test [35, 41, 46] and frameless picture-frame test [15, 62, 63]
  - Out-of-plane bending: loop test [57, 64]
- Experimental validation of the assumptions of tensile and friction behaviours could be performed as several studies indicate that these drapability behaviours of reinforcement can affect the outcome of the preforming. Also, sensitivity analysis (like tensile from this thesis) can be performed on the frictional behaviour. Characterising tensile and friction behaviours could be performed to improve accuracy of wrinkle prediction in complex geometry preforming.

# References

[1]     L. Khoun and P. Trudeau, "SNAP RTM: A cost-effective compression-RTM variant to manufacture composite component for transportation applications," presented at the ACCE 2018, USA, 2018.

[2]     F. Lionetto, A. Moscatello, and A. Maffezzoli, "Effect of binder powders added to carbon fiber reinforcements on the chemoreology of an epoxy resin for composites," *Composites Part B: Engineering,* vol. 112, pp. 243-250, 2017.

[3]     L. Grou, "Preforming Process for Out-of-Autoclave Composite Manufacturing," Master of Engineering, Mechanical Engineering, McGill University, Canada, 2019.

[4]     S. Chen *et al.*, "Double diaphragm forming simulation for complex composite structures," *Composites Part A: Applied Science and Manufacturing,* vol. 95, pp. 346-358, 2017.

[5]     Y. Dong, R. Lin, and D. Bhattacharyya, "Finite element simulation on thermoforming acrylic sheets using dynamic explicit method," *Polymers and Polymer Composites,* vol. 14, no. 3, pp. 307-328, 2006.

[6]     G. Creech, "Mesoscopic finite element modelling of non-crimp fabrics for drape and failure analyses," PhD, Cranfield University, United Kingdom, 2006.

[7]     A. Mallach, F. Härtel, F. Heieck, J.-P. Fuhr, P. Middendorf, and M. Gude, "Experimental comparison of a macroscopic draping simulation for dry non-crimp fabric preforming on a complex geometry by means of optical measurement," *Journal of Composite Materials,* vol. 51, no. 16, pp. 2363-2375, 2017.

[8]     D. Mattsson, "Mechanical performance of NCF composites," PhD, Applied Physics and Mechanical Engineering, Luleå tekniska universitet, Luleå, 2005.

[9]     M. A. Lepore, L. Ferrante, L. Sanguigno, and A. R. Maligno, "A non-crimp fabric mechanical characterization for the production of aerospace components," *Material Design & Processing Communications,* vol. 3, no. 5, p. e222, 2021.

[10]    B. Sköck-Hartmann and T. Gries, "Automotive applications of non-crimp fabric composites," in *Non-Crimp Fabric Composites*: Elsevier, 2011, pp. 461-480.

[11]    S. G. Advani and E. M. Sozer, *Process modeling in composites manufacturing*. CRC press, 2002.

[12]    L. E. Asp, F. Edgren, and A. Sjögren, "Effects of stitch pattern on the mechanical properties of non-crimp fabric composites," *Proceeding of the 11 ECCM,* pp. 31.05-03.06, 2004.

[13]    S. Allaoui *et al.*, "Experimental and numerical analyses of textile reinforcement forming of a tetrahedral shape," *Composites Part A: Applied Science and Manufacturing,* vol. 42, no. 6, pp. 612-622, 2011.

[14]    M. Sherburn, "Geometric and mechanical modelling of textiles," PhD, University of Nottingham, United Kingdom, 2007.

[15]    L. Krishnappa, J.-H. Ohlendorf, M. Brink, and K.-D. Thoben, "Investigating the factors influencing the shear behaviour of 0/90∘ non-crimp fabrics to form a reference shear test," *Journal of Composite Materials,* vol. 55, no. 20, pp. 2739-2750, 2021.

[16]    J. Viisainen and M. Sutcliffe, "Characterising the variability in wrinkling during the preforming of non-crimp fabrics," *Composites Part A: Applied Science and Manufacturing,* vol. 149, p. 106536, 2021.

[17]    P. Middendorf and C. Metzner, "Aerospace applications of non-crimp fabric composites," *Non-Crimp Fabric Composites,* pp. 441-449e, 2011.

[18]    F. Heinecke and C. Willberg, "Manufacturing-induced imperfections in composite parts manufactured via automated fiber placement," *Journal of Composites Science,* vol. 3, no. 2, p. 56, 2019.

[19]    S. Chen, O. McGregor, L. Harper, A. Endruweit, and N. Warrior, "Defect formation during preforming of a bi-axial non-crimp fabric with a pillar stitch pattern," *Composites Part A: Applied Science and Manufacturing,* vol. 91, pp. 156-167, 2016.

[20]    J. Launay, G. Hivet, A. V. Duong, and P. Boisse, "Experimental analysis of the influence of tensions on in plane shear behaviour of woven composite reinforcements," *Composites science and technology,* vol. 68, no. 2, pp. 506-515, 2008.

[21]    A. A. Skordos, C. M. Aceves, and M. P. Sutcliffe, "A simplified rate dependent model of forming and wrinkling of pre-impregnated woven composites," *Composites Part A: Applied science and manufacturing,* vol. 38, no. 5, pp. 1318-1330, 2007.

[22]    P. Boisse, N. Hamila, E. Vidal-Sallé, and F. Dumont, "Simulation of wrinkling during textile composite reinforcement forming. Influence of tensile, in-plane shear and bending stiffnesses," *Composites Science and Technology,* vol. 71, no. 5, pp. 683-692, 2011.

[23]    B. Liang, N. Hamila, M. Peillon, and P. Boisse, "Analysis of thermoplastic prepreg bending stiffness during manufacturing and of its influence on wrinkling simulations," *Composites Part A: Applied Science and Manufacturing,* vol. 67, pp. 111-122, 2014.

[24]    M. Nishi, T. Hirashima, and T. Kurashiki, "Textile composite reinforcement forming analysis considering out-of-plane bending stiffness and tension dependent in-plane shear behavior," in *Proceedings of the 16th European Conference On Composite Materials, Seville, Spain*, 2014.

[25]    K. Potter, *Lecture 4. Basic Processes - Variability and defects.* Bristol: University of Bristol, 2011.

[26]    U. Mohammed, C. Lekakou, L. Dong, and M. Bader, "Shear deformation and micromechanics of woven fabrics," *Composites Part A: Applied Science and Manufacturing,* vol. 31, no. 4, pp. 299-308, 2000.

[27]    J. Pazmino, V. Carvelli, and S. V. Lomov, "Formability of a non-crimp 3D orthogonal weave E-glass composite reinforcement," *Composites Part A: Applied Science and Manufacturing,* vol. 61, pp. 76-83, 2014/06/01/ 2014, doi: https://doi.org/10.1016/j.compositesa.2014.02.004.

[28]    A. Endruweit, A. C. Long, F. Robitaille, and C. D. Rudd, "Influence of stochastic fibre angle variations on the permeability of bi-directional textile fabrics," *Composites Part A: Applied science and manufacturing,* vol. 37, no. 1, pp. 122-132, 2006.

[29]    Z. Chen, S. Pan, Z. Zhou, T. Lei, B. Dong, and P. Xu, "The effect of shear deformation on permeability of 2.5 d woven preform," *Materials,* vol. 12, no. 21, p. 3594, 2019.

[30]    N. Jeppesen, V. Dahl, A. Christensen, A. Dahl, and L. Mikkelsen, "Characterization of the fiber orientations in non-crimp glass fiber reinforced composites using structure tensor," in *IOP Conference Series: Materials Science and Engineering*, 2020, vol. 942, no. 1: IOP Publishing, p. 012037.

[31]    J. Krebs, D. Bhattacharyya, and K. Friedrich, "Production and evaluation of secondary composite aircraft components—a comprehensive case study," *Composites Part A: applied science and manufacturing,* vol. 28, no. 5, pp. 481-489, 1997.

[32]    E. Group. "PAM-FORM." https://www.esi.com.au/software/pamform/ (accessed.

[33]    K. Vanclooster, S. V. Lomov, and I. Verpoest, "Experimental validation of forming simulations of fabric reinforced polymers using an unsymmetrical mould configuration," *Composites Part A: Applied Science and Manufacturing,* vol. 40, no. 4, pp. 530-539, 2009.

[34]    "Fibersim 101: (4 of 14) Plies." SIEMENS. https://community.sw.siemens.com/s/article/fibersim-101-4-of-14-plies (accessed.

[35]    V. N. Khiêm, H. Krieger, M. Itskov, T. Gries, and S. E. Stapleton, "An averaging based hyperelastic modeling and experimental analysis of non-crimp fabrics," *International Journal of Solids and Structures,* vol. 154, pp. 43-54, 2018/12/01/ 2018, doi: https://doi.org/10.1016/j.ijsolstr.2016.12.018.

[36]    D. J. Steigmann, "Mechanical response of fabric sheets to three-dimensional bending, twisting, and stretching," *Acta Mechanica Sinica,* vol. 31, no. 3, pp. 373-382, 2015.

[37]    A. Long, B. Souter, F. Robitaille, and C. Rudd, "Effects of fibre architecture on reinforcement fabric deformation," *Plastics, rubber and composites,* vol. 31, no. 2, pp. 87-97, 2002.

[38]    E. Syerko, S. Comas-Cardona, and C. Binetruy, "Models of mechanical properties/behavior of dry fibrous materials at various scales in bending and tension: A review," *Composites Part A: Applied Science and Manufacturing,* vol. 43, no. 8, pp. 1365-1388, 2012.

[39]    D. Lussier and J. Chen, "Material characterization of woven fabrics for thermoforming of composites," *Journal of Thermoplastic Composite Materials,* vol. 15, no. 6, pp. 497-509, 2002.

[40]    *PAM-FORM User's Guide*. ESI Group, 2020.

[41]    J. Cao *et al.*, "Characterization of mechanical behavior of woven fabrics: experimental methods and benchmark results," *Composites Part A: Applied Science and Manufacturing,* vol. 39, no. 6, pp. 1037-1053, 2008.

[42]    P. Boisse, N. Hamila, E. Guzman-Maldonado, A. Madeo, and G. Hivet, "The bias-extension test for the analysis of in-plane shear properties of textile composite reinforcements and prepregs: a review," *International Journal of Material Forming,* vol. 10, no. 4, pp. 473-492, 2017.

[43]    D. Bae, S. Kim, W. Lee, J. W. Yi, M. K. Um, and D. G. Seong, "Experimental and Numerical Studies on Fiber Deformation and Formability in Thermoforming Process Using a Fast-Cure Carbon Prepreg: Effect of Stacking Sequence and Mold Geometry," *Materials,* vol. 11, no. 5, p. 857, 2018. [Online]. Available: https://www.mdpi.com/1996-1944/11/5/857.

[44]    S. Chen, "Fabric forming simulation and process optimisation for composites," PhD, University of Nottingham, United Kingdom, 2016.

[45]    S. Bel, P. Boisse, and F. Dumont, "Analyses of the deformation mechanisms of non-crimp fabric composite reinforcements during preforming," *Applied Composite Materials,* vol. 19, no. 3, pp. 513-528, 2012.

[46]    G. Lebrun, M. N. Bureau, and J. Denault, "Evaluation of bias-extension and picture-frame test methods for the measurement of intraply shear properties of PP/glass commingled fabrics," *Composite structures,* vol. 61, no. 4, pp. 341-352, 2003.

[47]    F. Schirmaier, K. A. Weidenmann, L. Kärger, and F. Henning, "Characterisation of the draping behaviour of unidirectional non-crimp fabrics (UD-NCF)," *Composites Part A: Applied Science and Manufacturing,* vol. 80, pp. 28-38, 2016.

[48]    S. Haanappel, R. Ten Thije, U. Sachs, B. Rietman, and R. Akkerman, "Formability analyses of uni-directional and textile reinforced thermoplastics," *Composites Part A: Applied science and manufacturing,* vol. 56, pp. 80-92, 2014.

[49]    *ASTM D1388: Standard test method for stiffness of fabrics*. ASTM International, 2008.

[50]    F. T. Peirce, "26—The "handle" of cloth as a measurable quantity," *Journal of the Textile Institute Transactions,* vol. 21, no. 9, pp. T377-T416, 1930.

[51]    E. de Bilbao, D. Soulat, G. Hivet, and A. Gasser, "Experimental study of bending behaviour of reinforcements," *Experimental Mechanics,* vol. 50, no. 3, pp. 333-351, 2010.

[52]    N. Lammens, M. Kersemans, G. Luyckx, W. Van Paepegem, and J. Degrieck, "Improved accuracy in the determination of flexural rigidity of textile fabrics by the Peirce cantilever test (ASTM D1388)," *Textile Research Journal,* vol. 84, no. 12, pp. 1307-1314, 2014.

[53]    K. A. Fetfatsidis, D. Jauffrès, J. A. Sherwood, and J. Chen, "Characterization of the tool/fabric and fabric/fabric friction for woven-fabric composites during the thermostamping process," *International journal of material forming,* vol. 6, no. 2, pp. 209-221, 2013.

[54]    P. Boisse, A. Gasser, and G. Hivet, "Analyses of fabric tensile behaviour: determination of the biaxial tension–strain surfaces and their use in forming simulations," *Composites Part A: Applied Science and Manufacturing,* vol. 32, no. 10, pp. 1395-1414, 2001.

[55]    S. V. Lomov *et al.*, "Carbon composites based on multiaxial multiply stitched preforms. Part 3: Biaxial tension, picture frame and compression tests of the preforms," *Composites Part A: Applied Science and Manufacturing,* vol. 36, no. 9, pp. 1188-1206, 2005.

[56]    J. Sargent *et al.*, "Benchmark study of finite element models for simulating the thermostamping of woven-fabric reinforced composites," *International Journal of Material Forming,* vol. 3, no. 1, pp. 683-686, 2010.

[57]    M.-G. Han and S.-H. Chang, "Draping simulations of carbon/epoxy fabric prepregs using a non-orthogonal constitutive model considering bending behavior," *Composites Part A: Applied Science and Manufacturing,* vol. 148, p. 106483, 2021.

[58]    M. Karaki, R. Younes, F. Trochu, and P. Lafon, "Progress in experimental and theoretical evaluation methods for textile permeability," *Journal of Composites Science,* vol. 3, no. 3, p. 73, 2019.

[59]    *GetData Graph Digitizer*. [Online]. Available: http://getdata-graph-digitizer.com/index.php

[60]    M. Derradji, J. Wang, and W. Liu, "5 - Fiber-Reinforced Phthalonitrile Composites," in *Phthalonitrile Resins and Composites*, M. Derradji, J. Wang, and W. Liu Eds.: William Andrew Publishing, 2018, pp. 241-294.

[61]    *EPIKOTE resin preform binder systems for mass production of composite parts*. HEXION, 2016.

[62]    H. Montazerian, A. Rashidi, M. Hoorfar, and A. Milani, "A frameless picture frame test with embedded sensor: Mitigation of imperfections in shear characterization of woven fabrics," *Composite Structures,* vol. 211, pp. 112-124, 2019.

[63]    C. Krogh, K. D. White, A. Sabato, and J. A. Sherwood, "Picture-frame testing of woven prepreg fabric: an investigation of sample geometry and shear angle acquisition," *International Journal of Material Forming,* vol. 13, no. 3, pp. 341-353, 2020.

[64]    T. K. Ghosh and N. Zhou, "Characterization of fabric bending behavior: A review of measurement principles," 2003.